Summer 7-13-2018

Selected Applications of Silicon Nanopillar Arrays.

Behnam Kheyraddini Mousavi
University of New Mexico

Behnam Kheyraddini Mousavi

Candidate

Electrical and Computer Engineering

Department

This dissertation is approved, and it is acceptable in quality and form for publication:

Approved by the Dissertation Committee:

Dr. Mani Hossein-Zadeh , Chairperson

Dr. Terefe Habteyes

Dr. Tito Busani

Dr. Payman Zarkesh ha

Dr. Seteven R.J. Brueck

Selected Applications of Silicon Nanopillar Arrays.

by

Behnam Kheyraddini Mousavi

B.S., Electrical Engineering, Tehran University, 2008

M.S., Electrical Engineering, Tehran University, 2011

DISSERTATION

Submitted in Partial Fulfillment of the
Requirements for the Degree of

Doctor of Philosophy
Engineering

The University of New Mexico

Albuquerque, New Mexico

July, 2018

Dedication

To my parents, Mahin and Behrouz and to my brother Arash...

Selected Applications of Silicon Nanopillar Arrays.

by

Behnam Kheyraddini Mousavi

B.S., Electrical Engineering, Tehran University, 2008
M.S., Electrical Engineering, Tehran University, 2011

PhD., Engineering, University of New Mexico, 2018

Abstract

Interaction of optical waves with nanostructures made of various material systems has been the subject of intensive research for many years. These researches have been mainly driven by the need to make smaller optical devices and exploiting the functionalities offered by light-matter interaction in nanoscale. Majority of the nanostructures are fabricated using electron beam (e-beam) lithography that is slow and expensive. As such alternative methods have been developed to enable nanoscale fabrication faster and less expensive. Among these interferometric lithography (IL) is a relatively simple method for quick fabrication of nanostructures. As IL method generates periodic patterns, exploring the potential applications of the nanostructures that can be fabricated using it, is of primary importance. This dissertation is focused on two applications of silicon nanostructures fabricated by IL method:

nanostructured anti-reflection layers (NALs) and plasmonic nanostructures based on arrays of silicon nanopillars (SiNPs) for surface enhanced Raman spectroscopy (SERS). Silicon has been chosen as the structural material due to its extensive usage as the substrate for monolithic electronic circuits and many optical devices.

NALs offer several advantages over traditional antireflection coatings made by multilayer deposition. NALs are created by fabricating a nanostructured surface on the substrate material without the need for deposition of different materials and therefore can tolerate large thermal gradients in high power laser applications. We have developed a mathematical model and calculated the optimal profile for the unit cell for a silicon NAL and examined its performance using rigorous coupled-wave analysis (RCWA). The impact of different geometrical parameters on the performance of NALs have been carefully studied. In particular we have evaluated the impact of these geometrical parameters on the transmitted optical power and suppression of higher spatial modes generation. Next using the theoretical outcomes as a guide, we have fabricated several silicon NALs using IL patterning followed by dry etching and measured and computed their performance in mid-IR spectral region.

The second category of silicon nanostructures studied here consist of flat top silicon nanopillar (SiNP) arrays with one or a stack of metallic nanodisks on top (with silica nanodisk as spacer) used for Raman enhancement applications. These structures, fabricated using IL, are designed to enhance Raman emission from the adsorbed molecules using surface plasmons. This is achieved by high electric field enhancement, through localization of plasmons at the edges. In order to understand the enhancement mechanism, resonance of these nanostructures along with the E-field enhancements are carefully studied using numerical simulations. Regarding possible role of nanopillars in field enhancement, simulation results have revealed hybridization between SiNP and plasmonic nanodisk stacks. This indicates possibility of transfer of energy of incident laser into plasmonic structure through nanopillar,

further amplifying the E-field enhancement. We have also studied the role of geometrical and structural parameters on the field enhancement of these nanostructures. This provides a guide for designing nanostructures with optimal field enhancement for SERS. Next, we have fabricated several samples of SiNPs caped with gold nanodisks and gold-silica-gold nanodisk (stacks) and tested their performance as SERS substrates by measuring the spectrum of the Raman signal (using Thionine and Methylene Blue as target molecules). Our experimental studies have revealed the impact of geometrical parameters of the SiNP and gold nanodisks on the Raman signal. We have also fabricated and tested gold nanodisk performance using SiO_2 nanopillar. Finally we have fabricated and tested SiNPs caped with selected non-metallic nanodisks obtained by post processing of nanodisks made of Ge, and TiN. This preliminary study paves the road for a new category of SiNP based SERS substrates that may have advantages over those that use metallic caps in certain applications.

Contents

Contents

Contents

Contents

Contents

List of Tables

Chapter 1

Introduction

Nanostructures and their application in optical interactions is the main focus of this dissertation. More specifically we have studied the interaction of optical waves with certain sub-wavelength structures. Two main applications are investigated: 1) Nanostructured antireflection layers (NALs) and 2) surface enhanced Raman spectroscopy (SERS) using metal or metal/insulator/metal plasmonic structures (MIM) over silicon nano-pillars (SiNPs).

When light passes through the interface between two mediums with different refractive indexes, it will get partially reflected. This happens due to sudden change in the refractive index between the two medium according to Fresnel equations. As in many applications reflection is undesired. Antireflection coatings (ARC) are commonly used to reduce reflection of light at the interface. These anti-reflection coatings can be in the form of thin film layers or nanotextured layers. Thin film ARC are based on destructive interference of light [70, 110, 19]. That is, the light reflected back from bulk material substrate, interferes destructively with the light reflected from surface of ARC layer [110]. Nanotextured ARC layers on the other hand, work by gradual change of effective refractive index from incidence medium (like air) into

the bulk material (like quartz or silicon). These nanostructured materials, work based on fill factor concept [110].

These nanostructures can replace the conventional multi-layer antireflection coatings [35]. If designed and fabricated correctly, nanostructured anti-reflection coatings (NALs), can almost completely eliminate reflection at the interface while the conventional method may be challenging due to difficulty of fabricating too many layers and finding the the materials with the desired refractive index. Another important advantage of NALs over traditional antireflection coating is the similarity of their thermal properties with the substrate. This eliminates the possibility of delamination due to temperature gradient in the presence of heating.

Structured anti-reflection layers started as micro-structured antireflection layers around 1980 [44]. Soon after fabrication techniques of nanostructured layers were developed [10, 110]. Later on these nanostructures were used as antireflection and anti-glare coatings. The most common anti-glare coatings were used to eliminated reflection from surface of materials like quartz and glass [117, 81]. These nanostructures also found their way in solar cell technology [77, 18, 122] and infrared detectors [134]. By texturing surface of substrates used for solar cell applications, scientists could effectively enhance the transmission of light into the high refractive index bulk materials such as silicon (which is transparent at IR)[85, 141]. NALs were used for enhancing transmission of LED light from high refractive index sources to low refractive index transmission mediums such as air [75, 79]. By advances in technology and emergence of new devices, the applications of nanostructured surfaces (also referred to as Moth-eye antireflection coatings in some references) also grew. Using materials transparent to infrared (IR) transmission to fabricate the antireflection nanotextures, the detection capabilities of infrared cameras considerably improved [54, 76]. Recently Weng et.al. used nanotextured CaF_2, which is also IR transparent, to enhance the efficiency of PbS_2 IR-detectors by 200%. [134].

As NAL is carved out of the substrate, it eliminates the residual stress issue that is a major limitation for fabrication of multilayer ARCs. This significantly increases their durability when exposed to repeated cooling and heating cycles. Therefore, one of the main applications of these NALs is enhancing transmission of light through optical elements used in high-power-laser applications [45, 124, 53, 55]. In such applications, it is also crucial to avoid scattering. This can be achieved by replacing the randomly distributed nanostructures by orderly arranged ones as shown by Hobbs et al [54] (See Fig. 1.1). The arrangement and profile of nanostructures is controlled by the fabrication method used.
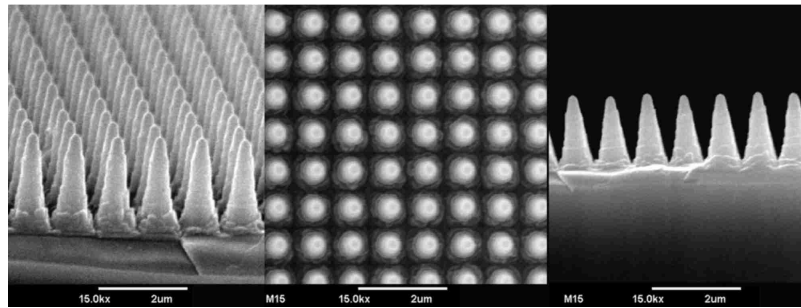
Figure 1.1: Nanostructured anti-reflection coating carved out of bulk silicon [54]. The tapered profile provide a smooth transition from air into silicon medium.

The choice of fabrication method depends on the application of the specific nanostructures, material and the cost. Most common applications of nanostuctured antireflection coatings (and their fabrication methods) include but are not limited to: optical lenses (using injection molding) [78], solar cells (using sol-gel methods [32] or soft imprint lithography [81]), anti-glare glasses (using self mask etching [117]) and Light-extraction enhancement as in GaN LEDs (using nanostructure growth [79]). Other fabrication methods which are used to fabricate nanostructures for different applications include hot embossing [52], colloidal mask [121], glanced angle deposited mask [83], self masking [117], laser ablation [111] nano-imprint lithography [15], and interference lithography [23]. The latter one, is relatively more expensive and best

suited for laser applications [127].

Interference lithography (IL) has recently been point of interest due to advances in laser technology and the demand for optical elements used for transmitting laser. IL generates periodic patterns with adjustable pitches and pattern sizes, which is well suited for fabrication of arrays of nanostructures designed to refrain introducing scattering in the transmitted laser beam while increasing transmission. IL is also compatible with silicon technology. Silicon is one of the most commonly used substrates in optoelectronic industry and is transparent to infrared light, therefore developing practical and cost effective methods for eliminating reflection in air-silicon interfaces is very important. Nanostructured antireflection layers carved out of silicon substrate provide high transmission (IR) with considerable advantages over conventional antireflection coatings. Silicon is transparent in infrared and texturing it, is an effective way of increasing transmission through this high refractive index material [54].

Table 1.1, briefly list the few substrate materials and fabrication methods used to fabricated nanostructured antireflection surfaces.

Table 1.1: **Brief summary of materials, methods and progress on NALs**

Substrate	Texturing Technique	Best Transmission	Date
Si,CZT,Ge,Sapphire, CZT, ZNS, ZnSe	Interference lithography	Over 94% [54]	2005
Glass	Hybrid nano-patterning lithography	98% [65]	2010
AZO	Holographic lithography	97% [84]	2010
Silicon	Colloidal silica mask	Over 99% [76]	2016

So far, considerable research has been done on fabrication of NALs for enhancing transmission of IR [76, 65, 77, 82, 65, 138, 86, 9, 134, 150, 55]. However, to best of our knowledge, no work has been done on studying the optimum profile of the nanostructures for light transmission with minimum scattering, which becomes

more critical if the refractive index of substrate is high. Also, the effect of pitch size in these periodic nanostructured antireflection layers have not been investigated in detail. We have investigated a possible optimum profile for maximizing the transmission of light, while keeping the height of the nanostructures as low as possible. Shorter silicon nanopillars (SiNPs) have considerable advantages over taller ones. Shorter SiNPs are more robust to mechanical damage and have proven to minimize introduction of higher spatial modes to the transmitted beam. As the height of SiNPs decreases, the effect of pitch becomes more significant. The optimum pitch resulting in maximum transmission at every wavelength is determined by post-processing the transmission simulation results obtained using Rigorous Coupled Wave Analysis (RCWA) method. We used IL patterning and plasma etching to fabricate periodic silicon nanopillars (SiNPs) with a tapered profile on bulk silicon substrates and measured IR transmission from air into the corresponding Si substrate.

The second topic investigated in this dissertation, is the Surface Enhanced Raman Spectroscopy (SERS) based on silicon nanopillars (SiNPs). Raman spectroscopy is a well-known technique for identifying the chemical composition of different molecules [5]. Since every Raman-active-molecule generates a unique Raman spectrum, the obtained spectrum includes the Raman signature of the molecular bonds of the specimen. Typically, Raman signals are very weak and therefore difficult to detect. As such, in addition to high intensity sources, highly sensitive detectors and high quality filters (for eliminating the excitation laser) [109, 21] are essential for Raman spectroscopy. Several techniques have been developed to further enhance Raman signals. Examples include surface enhanced Raman, Resonant Raman, stimulated Raman, and hyper Raman [102, 91, 31, 46, 42]. Among these, Surface-enhanced Raman spectroscopy (SERS) is a relatively cheap and easy technique. SERS is based on electromagnetic field enhancement and/or chemical enhancement [131]. Electromagnetic field enhancement (EM) is achieved through localization of surface plasmons (mainly on metallic nanostructures). To expose the specimen molecules to this en-

hanced electric field, they are allowed to get adsorbed on these structures, which are generally made of Au, Ag, Cu or Ni, before conducting the measurement. A considerably large electric field, results in a enhancement of Raman emission from the molecules.

Considerable research has been done on design and fabrication of nanostructures for SERS applications, motivated by better performance, lower cost, and compatibility with certain systems [58, 11, 17, 59]. The basic principle used in all these designs is the confinement of the plasmons (usually) at the edges of the plasmonic nanostructures and generation of high electric field peaking at resonance frequency (due to higher quality factor of the plasmonic resonator at resonance frequency). The resulting large electric field causes strong polarization of the adjacent molecules and therefore enhanced Raman emission.

Nanodisks made of plasmonic materials have gained considerable interest due to ease of fabrication and compatibility with silicon technology. Research groups like Zahng et.al. have investigated the resonance of $Ag/SiO_2/Ag$ nanodisks using analytical analysis and Bessel equations for the oscillating plasmonic waves [143]. The resonances frequencies are important since they are directly related to scattering cross section peaks. If a plasmonic structure is excited with a laser whose frequency is close to the structures scattering cross section peak, the laser can efficiently enhance the field at the edges of the plasmonic disk due to localization of a portion of resonating plasmons [120, 30, 119]. Chang et.al has studied the scattering cross section of MIM and hybridization of two plasmonic disks separated by a thin insulator layer. He has studied the effect of the SiO_2 insulator layer thickness on the resonance frequency of even and odd modes generated by the hybridization of the two disks [30, 47]. Hybridization can further enhances the field at the edges of the plasmonic disks. Raman enhancement, field enhancement and scattering cross section of $Au/SiO_2/Au$ nanodisks are studied experimentally by Su et.al. [120, 119]

(he has not compared the difference between Raman enhancement by single disk and disk-dielectric stack). Zhang et.al.[144] conducted a theoretical study on the formation of symmetric and asymmetric modes when more than two metal layers are used. Although these modes play role in resonance (and therefore field enhancement) of multi layer metal disks, there hasn't been a substantial study on the effect of these modes on Raman enhancement. Metallic or MIM plasmonic structures are generally fabricated directly over a substrate such as quartz [119]. However, little has been done on studying the effect of substrate material and its geometry, on Raman enhancement generated by plasmonic disk.

Bare silicon nanopillars have been investigated for possibility of enhancing Raman[72, 146, 27]. However these studies have mainly focused on Raman of silicon itself (without using an analyte). Recently, two groups (Wells et.al. and caldarola et.al.) have fabricated deep sub-micron SiNPs which are capable of detecting analytes [133, 24]. Silicon nanopillars do have the potential of assisting field enhancement but they have rarely been investigated as a platforms for plasmonic disks [25, 26]. We have studied the effects of using flat-top silicon nanopillars as the substrate for plasmonic single nanodisks and nanodisk stacks.

There are a variety of approaches for fabrication of nanostructures for SERS, such as nanosphere lithography [51], self assembly [11] and electrochemical roughening [3]. However for integrating Raman enhancement surfaces with a microelectronic, photonic or microfluidic circuits (or lab on a chip [94, 130, 125]), one would need to use approaches that are compatible with IC technology [128, 129, 112]. Optical lithography provides a feasible way for integrating nanostructures and plasmonic nanostructures on a circuit [57]. This is highly needed since although for example colloidal nanoparticles can enhance Raman signal [123], they can not controllably be integrated over sub-micron regions in an IC . Among different approaches, e-beam lithography [61, 4], and interference lithography [136, 92, 6] are two candidates for

integrating SERS structures on a chip, in deep sub-micron dimensions [104]. For periodic structures, IL is a cost effective, relatively simple and fast alternative to e-beam lithography. We have used IL to create periodic arrays of flat top SiNPs which are carved out of silicon substrate. We have then used these SiNPs as a substrate for plasmonic nanodisks and stacks.

A brief history of advances on SERS relevant to lithography techniques, has been shown in table 1.2. The table includes works on plasmonic disks and SiNPs fabricated by IL and e-beam lithography and also covers some simulations related to metallic disks or metal/dielectric stacks analysis, using Finite Difference Time Domain (FDTD) approach.

Table 1.2: **Brief summary of materials, methods and progress of SERS based on plasmonic disks and SiNPs**

Nanostructure	Substrate	Method	Study Focus	Date
$Ag/SiO_2/Ag$ Disks	Quartz	IL	Scattering, Raman of analyte [120]	2006
Au/SiNP	Si	E-beam lithography	Raman of analyte [25]	2011
SiNP	Si	E-beam lithography	Raman of SiNP [87]	2010
SiNP	Si	E-beam lithography	Raman of analyte [133]	2012
Ag and $Ag/SiO_2/Ag$ Disks	-	Simulation	Resonance modes [30]	2012
Multilayer Ag/SiO_2 Disks	-	Simulation	Resonance modes [47]	2013
$Au/Al_2O_3/Au$ Disks	-	Simulation	Resonance modes [144]	2015
SiNP	Si	E-beam lithography	Raman of analyte [24]	2015

While the impact of the silicon nanodisk diameter (down to $80nm$ [25]) on field and Raman enhancement has been investigated, to best of our knowledge, the effect of dimensions (including height of nanopillar) and materials of nanopillars (NPs), on field and Raman enhancement has not been studied, neither theoretically nor experimentally. Also, Raman generation based on stacks of several plasmonic layers

fabricated on top of SiNP has not been studied experimentally (but studied theoretically [120]). This is partially due to challenges associated with fabrication of multilayer stacks on silicon surface using lift off process. SiNPs provide a practical way of fabricating multi-layer plasmonic structures with no specific limitation on the number of layers. In addition (as we will show) when the plasmonic layer is on top of SiNP, the efficiency of energy transfer from the excitation laser beam to the localized plasmon resonance is increased. We have theoretically investigated the formation of hybrid resonance mode between SiNP and $Au/SiO_2/Au$ structure, and compared it with scattering cross section results. This hybridization can also considerably affect the resonance frequency. SiNP-based plasmonic structures offer the possibility of maximizing Raman signal in integrated configurations. We have also fabricated and tested non-metallic layers over SiNPs and showed that after some post processing they are capable of enhancing the Raman signal. The generated Raman signal from non-metals may become a major point of interest, because of the need for eliminating metals in certain applications.

Here is a summary of the materials covered in the following chapters:

Chapter 2 is dedicated to fabrication methods. Specific processes used to fabricate the nanostructures (both NAL and SERS) are explained. We use IL to generate the required photoresist patterns for all of our fabrications. As mentioned before IL is a relatively low cost, simple and scalable lithographic technique; however controlling the feature size and pitch of the patterns made by IL can be very challenging. We have developed recipes for controlling different geometric parameters that along with the our recipes for photo-resist development and silicon etching, allowed us to fabricate efficient NALs. Different recipes are provided for controlling various structural parameters. The nanostructures are crudely divided into two groups: 1) moth-eyed structures and nanopillars. In the second part of chapter 2, SiNPs will get fine-tuned for Raman applications. Different plasmonic structures will be fabricated on top the

nanopillars. These structures will be mainly in the form of metallic layers separated with dielectric layers.

Chapter 3 is mainly focused on measurement techniques used for characterizing NALs and characterizing the scattering and Raman emissions from Nanostructures (SiNPs). The design and operation mechanisms of the corresponding equipments and setups are presented and explained.

Chapter 4 is devoted to an the in depth study of NALs based on periodic arrays of SiNPs. This includes both theoretical and experimental analysis of the interaction of optical waves with these structures. Optimum profiles are designed to yield maximum transmission of infra-red light from air into silicon substrate. This includes discussions on the fill-factor and optimal height of NALs. These theoretical analysis provide very useful guidelines for designing optimal profile of NALs. Several samples have been fabricated and characterized using the methods explained in chapter 3. Very high efficiency ARC layers (for IR) have been fabricated using IL patterning and ICP etching of silicon.

Chapter 5 is devoted to study of surface enhanced Raman emission based on nanostructures consisting of SiNPs caped with one or more metallic nanodisks (serving as plasmonic resonators). In order to understand the enhancement, localized plasmon oscillations, electromagnetic modes, E-field enhancement and absorption/scattering cross-sections of these nanostructures are carefully studied using numerical simulations. To simplify the complex behavior of the SiNPs caped with metallic nanodisks, first we study metallic nanodisks and SiNPs separately and later we look at the optical response of the whole nanostructure. This allowed for better understanding of the interaction between SiNPs and the metallic nanodisks fabricated on top of them. The hybridization of plasmonic and cavity resonances are studied numerically. To support the calculated scattering cross-sections, we present the measured scattering cross-sections for bare SiNPs and those caped with metallic nanodisk. The two

main phenomena happening for the plasmonic metals are the coupling of the two metal nanodisks, which generate odd and even modes [30, 47] and in the case of multilayer stacks symmetric and asymmetric modes [144]. When considering the effect of hybridization of SiNP and the metal stacks, the problem gets a little bit complex. Other than numerical evaluation, the practical option we have for characterizing our designs, is measuring the Raman enhancement of test molecules by our plasmonic nanostructures. Therefore, we measured Raman spectra from various samples of SiNPs caped with metallic nanodisks. For these measurements we used Thionine, Rhodamine B and Methylene Blue as the target molecules. Thionine and Rhodamine B are primarily used for comparing Raman signal enhancement on different structures (and therefore the associated field enhancement) and Methylene Blue is used to study the plasmonically induced chemical transitions [123]. using different nanostructures. These measurements along with the scattering measurements are used to describe the overall optical response of the metallic nanodisk-SiNP coupled system. The Raman measurements include Au nanodisks, $Au/SiO_2/Au$ and $Au/SiO_2/Au/SiO_2/Au/SiO_2/Au$ stacks on top of SiNPs. We have also observed and measured both temporal (using Thionine) and spectral (using Methylene Blue) evolution of the Raman spectrum. Our study also covers SiNPs caped with selected non-metallic nano-disks obtained by post processing (NH_3 and oxygen plasma-treatment) of nanodisks made of Ge, and TiN nanodisks. Germanium permittivity is positive in visible wavelengths [48]. Previously other groups have been able to generate Raman enhancement from germanium by surface processes over Germanium nanowires. According to Wang et. al. Germanium can not have plasmons contribution at visible wavelength[131]. Therefore any Raman enhancement is related to Charge Transfer (CT) between the surface of Ge and the specimen molecule. We have processed germanium by plasma and have achieved considerable Raman enhancement from Methylene Blue molecule. In the course of our study we have observed that the permittivity of Germanium becomes negative at visible after the plasma process. This

indicates possible contribution of plasmon at visible wavelength. We don't expect that this phenomena is happening due to impurities [100], and believe that a new composite material has been formed although we don't yet know the structure of this new material. The other nonmetal exhibiting plasmonic characteristics is Titanium Nitride. TiN is known for having a negative permittivity at $630nm$ [108]. Therefore, there is a possibility for the role of plasmons in Raman enhancement. Other groups have fabricated TiN nanorods above 800^{oC}, which are capable of Raman enhancement [146]. We have chosen to deposit TiN films over SiNPs for integration purposes. Our results show that pure TiN thin films couldn't generate Raman enhancement. By further processing TiN over SiNP under NH_3 plasma, we have been able to enhance Raman of MB. Last of all we have investigated removing the background noise, which is observed for the cases of Raman enhancement from Rhodamine B molecules over Au stack on SiNP. The Raman signal quality has been highly enhanced.

Chapter 2

Fabrication

In this chapter the details of the fabrication processes used in this dissertation will be discussed. Since many samples were fabricated and characterized during the course of this project, this chapter is focused on introducing the basic principles of each fabrication processes covering the main factors that affect the outcome of each process. The sequence of the steps and details such as temperature, time and thicknesses are discussed in the following chapters and will be explained case-by-case as each sample is different.

The fabrication processes used in this dissertation can be divided into two main categories those that rely on interferometric-lithography (IL) and those that do not.

2.1   Lithography

Lithography is Greek word meaning producing by stone and has been used as a printing method in ancient civilizations. In modern era, lithography is mainly used to refer to the methods that rely on optical exposure of selected areas of a photoresist (PR) material in order to create the desired protective pattern on a substrate. Using lithography, micro/nano-structures can be fabricated over a substrate. The substrates used in this dissertation are (100) silicon or SiO_2 over silicon. Nano-sized features over the substrate will range from non-metals to metals. In this work we have used a specific type of lithography called "Interferometric Lithography" or IL. The main steps of IL are explained below.

2.2   Interferometric Lithography (IL)

Interferometric-Lithography (IL) is a mask-less lithography. In this method two beams of light interfere and due to constructive and destructive interference, the two beams cancel each other in some regions while amplifying each other in some other regions depending on their relative phase. This will result in dark and bright regions in the image plane. Figure 2.1 illustrates the interferometric lithography setup used in this dissertation. The light source is a pulsed laser with a wavelength of $355nm$ and adjustable output power tunable from $1mW$ to $10W$. The power of each $3ns$ long laser pulse can be adjusted from 1 to $100mJ$ with repletion rate of 1 to 100 pulse per second. The $355nm$ UV laser is generated by frequency doubling a $1060nm$ source laser and adding the resulting green wavelength (530 nm) to original IR wavelength (1060 nm) to generate the 355nm laser ($\frac{1}{\lambda_3} = \frac{1}{\lambda_1} + \frac{1}{\lambda_2}$).The residual green light is filtered out and the UV wavelength is uniformly distributed over a concave lens using a lens.
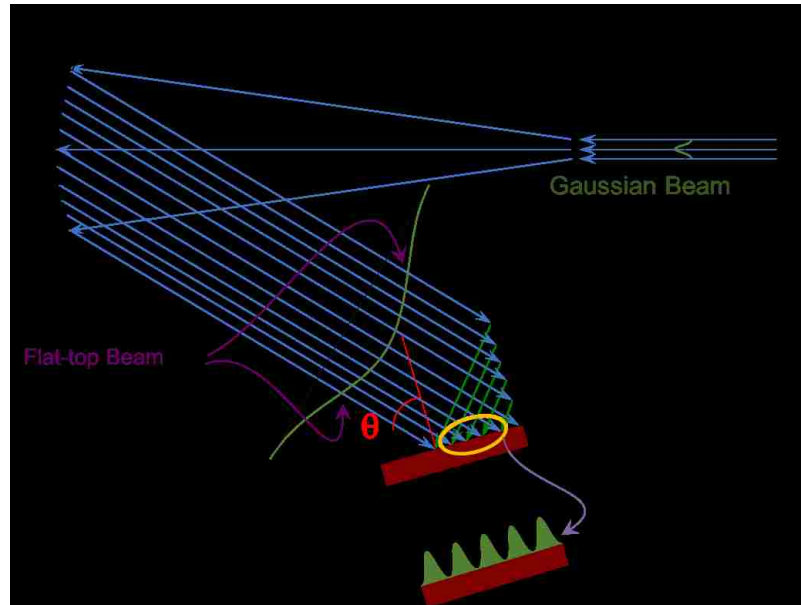
Figure 2.1: The IL setup showing the generation of the periodic nano-patterns on the photoresist through interference.

The reflected wave from the mirror is a collimated beam with a diameter larger than 6 inches (that is considerably wider than the size of the sample). While lowering the intensity of light, expanding the beam is necessary as it improves the spatial coherence over the sample. Moreover the power distribution over the sample will be more uniform as the intensity distribution across the beam becomes closer to a flat-top function as opposed to Gaussian.

This will insure identical intensity over the sample surface. Half of the beam is reflected from a mirror mounted perpendicular to the sample (represented by the black double-line) and interferes with the other identical half over the surface of the wafer (represented with the red rectangle). The interference illustrated here results in strips of dark and bright fringes. The bright regions being where the two beams of light interfere constructively and the dark regions being the regions where the two beams interfere destructively. After laser exposure and developing the photoresist, parallel strips of photoresist remain on the wafer.

2.2.1 Theory of IL

The relative phase between the two beams is a function of the incident beam angle and the location in the image-plane. This means that the pitch of the periodic interference pattern, can be controlled by changing the angle of the mirror, which in turn changes the angle of the incident beam with respect to the substrate (θ). This dependence can be expressed as the following equation (eq. 2.1), where d is the pitch, λ is the wavelength of the laser used and θ is the angle between the incident light and normal to sample substrate. This formula suggests that theoretically, the smallest pitch achievable by this set up is $\frac{\lambda}{2n_M}$ where n_M in our case, is the refractive index of air, which is 1:

$$d = \frac{\lambda}{2n_M.sin(\theta)} \tag{2.1}$$

When using IL setup in conjunction with equation (2.1), one should keep in mind to have an antireflection layer (ARC layer) of proper-thickness (coated on substrate before PR) to minimize internal reflections at PR-substrate boundary. The recommended thickness for the bottom anti-reflection coating (under the PR in contrary to top anti-reflection coating which is on top of PR) is $\frac{\lambda}{2n_{ARC}}$, where n_{ARC} is the refractive index of the Arc layer. The ARC layer is required to avoid multiple reflections that reduce the contrast of the original interference pattern (this is specially important for generating sub-micron patterns).

2.2.2 Maximum Sample Size in IL

The mechanism of fringe formation explained in Sec. 2.2 would yield in periodic fringes all over the image-plane if the laser used was composed of absolutely a single wavelength with infinitely small bandwidth. However no matter how good of a laser source we use, the spatial coherence is limited and this limits the exposure area.

This means that the sample size is limited and can not be larger than the spatial coherence length of the laser. Coherence-length can be calculated using (2.2) [7].

$$L = \frac{2ln(2)\lambda^2}{\pi n \Delta\lambda}$$

(2.2)

No matter how small the bandwidth ($\Delta\lambda$) is, there is an upper limit for the sample size that can be patterned with high fidelity. Another factor that influences the minimum feature size is the intensity profile of the beam. A laser beam by default has a Gaussian profile, being intense in the center and dimmer on the edges. If the beam is not flat top (constant amplitude), the resulting interference pattern will be affected and the fringe contrast will be higher at the center and considerably reduce toward the edges resulting in dimmer fringes. This will also result in patterns with smaller depth (for a negative photoresist) toward the edges from the center of the beam as illustrated in Fig 2.2. The same non-uniformity problem exists if the sample size is comparable to coherence length. Thus in order to obtain a larger sample, one needs to use a laser with smaller bandwidth. All the samples fabricated for this project are selected smaller than $1cm^2$.

2.2.3 Fabrication of A 2D Array of Features on A Silicon Wafer

In this section the details of the fabrication procedure required to fabricate an array of Silicon Nano-Pillars (SiNP) on a Silicon wafer will be explained. The substrate is a polished, (100) single crystal silicon wafer. The first step is to clean the wafer, then the wafer is coated with an antireflection and photoresist layers on top of it, and then exposed to $355nm$ laser light in the interferometric lithography setup and developed. After removal of Arc from the exposed areas of photoresist (developed regions), a thin layer of Cr or Ni is deposited all over the sample using electron-beam deposition method. The metal layer will be deposited both on the exposed silicon and on the
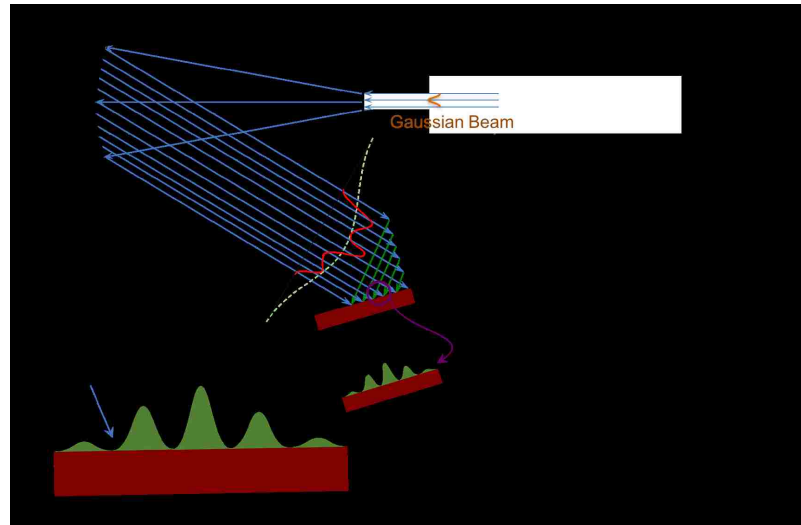
Figure 2.2: The impact of the beam profile being non-flat-top, on the interference pattern

regions covered with photoresist. Lift-off process is used to remove metal layer from the unwanted regions. Since the locations of the wafer where a metal-mask is not desired are covered with a layer of photoresist to begin with, an acetone gun is used to achieve proper lift-off (wash off the photoresist with the metal on it). Acetone dissolves the photoresist causing the metal layer over it, to peel off and get washed away. Acetone gun does this by blowing acetone with pressure over the sample. Finally an oxygen-plasma treatment is used for removal of remaining anti-reflection coating. The product of this set of procedures is a metal layer covering some specific regions of the silicon substrate. This metal layer protects/masks the silicon beneath, during subsequent etching processes and is commonly referred to as metal mask. The patterned silicon wafer is then etched to create the desired structure. Lift-off for metal patterning the silicon is necessary since photoresist etches easily in the plasma used for silicon etching.

Figure 2.3 illustrates the steps necessary to fabricate nanostructures using metal mask and plasma etching. Steps (a)-(d) of Fig 2.3 are common for both isotropic

and anisotropic etches. Figures 2.3(e) and 2.3(f) illustrate the characteristic shapes resulting from anisotropic and isotropic etching of the masked-wafer of Fig 2.3(d), respectively. Plasma etching can be "isotropic", "anisotropic" (other anisotropic etches can be found at [66]) or a combination of both. During anisotropic etching, the pressure of the plasma chamber is kept low (usually below $15mTorr$ for the system used here) and the power of plasma is increased. Lowering the pressure increases the mean free path of the etchant species and increasing the power, increases their momentum [101]. The combined effect increases the directionality of the etch resulting in a vertical etch. In the case of isotropic etching on the other hand, the plasma pressure relatively higher, and the power of the plasma is kept rather low. Short mean free path and lower momentum of the etching species means the etching will happen homogeneously in all directions. There is an other deterministic factor that plays a crucial role for vertical etching and that is the protective Teflon layer which will be discussed in section 2.3.

The procedure illustrated in Fig. 2.3 is used for fabrication of nano-pillars in this dissertation. The fabricated nano-pillars can vary in shape, configuration, concentration and critical dimensions. The details related to fabrication of each specific type of nano-pillars will be covered case-by-case in Section 2.3. Some applications of nanopillars, require further processing such as deposition of metallic and nonmetallic layers on top of the nano-pillars.

Fabrication of high quality metal masks and optimization of etching procedures paves the way to high quality nano-structures and nanopillars.. The generic steps required to fabricate a metal mask will be covered in this section. The following section will focus on some special cases of metal masks as well es proper etching techniques and further processing.
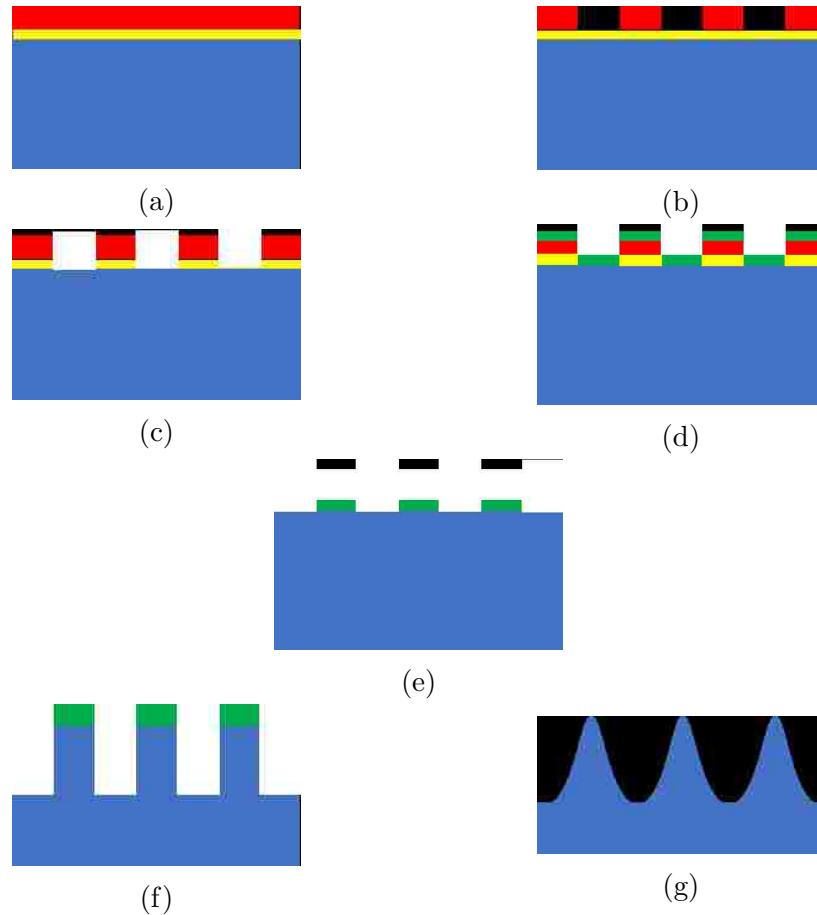
Figure 2.3: Silicon nanostructure fabrication steps (a) Spin-coated photoresist on a silicon wafer. (b) Patterned the photoresist using interferometric lithography. (c) The antireflection layers on the exposed areas is etched using oxygen plasma. (d) Deposition of a layer of metal (Cr or Ni) as the mask material. (e) Lift-off of mask and removal of the Arc layer by oxygen plasma afterwards. now only metal mask is left on the substrate. (f) Anisotropically etched substrate. (g) Isotropically etched substrate.The bulk silicon, Arc, photoresist, and the mask metal are shown in blue, yellow, red, and green respectively.

Wafer Cleaning

The standard procedure for cleaning the wafer is to run RCA processes. Depending on the type of the contaminations, either of the two different versions of RCA procedures (or both) can be used.

RCA *I*, cleans the organic contaminations from the surface of the wafer. In this process, the wafer is soaked in a solution which is composed of 1 part H_2O_2 (30%), 1 part NH_4OH(29%) and 5 part DI water. The solution should have a temperature of $75^{oC} - 80^{oC}$. The wafer is soaked for 10 minutes, washed with deionized (DI) water and then dried using a nitrogen gun.

RCA *II* targets the ionic and metallic contaminations. The solution used for RCA *II* is is composed of 1 part H_2O_2, (30%), 1 part HCL(37%) and 6 parts DI water. The rinse time and solution temperature remains the same as RCA *I* and the wafer needs to be rinsed off with DI water at the end. Then, the wafer is dried off by nitrogen gun.

In order to remove both organic and inorganic contaminations it is recommended to use both RCA *I* and *II* as it was done here.

One Dimensional (1-D) Periodic Array

A thin layer of "Barli 90AZ" or "ICON7" anti-reflection coating is spin coated on the silicon wafer at $3000RPM$ and baked at 200^{oC} for 1 minute. Then the wafer is coated with "NR7-500p", a negative photoresist, at $3000RPM$ and baked for 1 minute at 150^{oC}.

The wafer is cut into smaller pieces by diamond scriber and rinsed by DI water to wash off any possible silicon particles. The coated wafer in placed on the sample holder of Interferometric Lithography setup. The vacuum pump is used to fix the substrate on the holder. The mirror of the IL set-up is orthogonal to the substrate as shown in Figure 2.1. The pitch can be adjusted by changing the angular position of the mirror/sample assembly with respect to the incident beam. The sample is exposed at a "repetition rate" of 50 and pulse power of 50 to $75mJ$.

It should be noted that increasing the exposure time in a negative photoresist can result in larger feature size due to side exposure. Unless specified otherwise, the post-exposure bake is performed at 110^{oC} for 1 minute. A diluted $RD6$ developer $(RD6(or MF^{TM})/H_2O = 3/1)$ develops the NR7-500p negative resist in ≈ 90 seconds. Figure 2.4 shows the result of this process. The stripes obtained so far, are "1D" pattern.
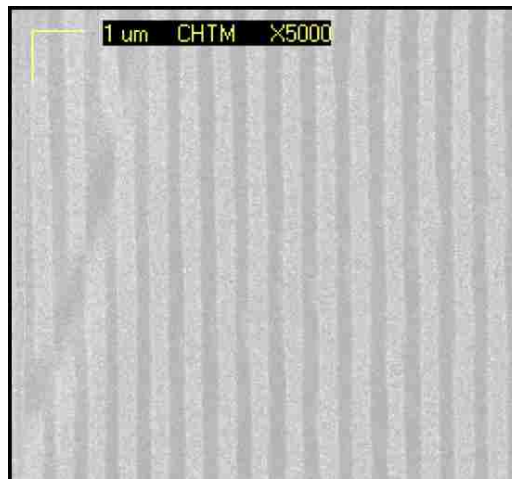
Figure 2.4: Simple lines generated for NR-7 resist spin coated over silicon.The good coherence length of the laser results in a uniform gap distribution between the lines.

Two Dimensional (2-D) Periodic Array

In order to fabricate a "2D" pattern, after the first exposure, the sample is rotated (90° in our case) and exposed again. The time required for the 2D exposure procedure is considerably less than the time required for 1D exposure procedure (usually by 30% to 50% less for each exposure). The sample then goes under 1 minute or a 40s, post-bake at 110^{oC} for1 minute for increasing cross linking in negative resist and is developed for 90 seconds by diluted $RD6$ developer. If the post exposure bake is not done, the whole resist peals off during developing. Finally the sample is washed by DI-water and dried by a nitrogen gun. Figure 2.5 shows an example of the resulting

2D photoresist pattern.
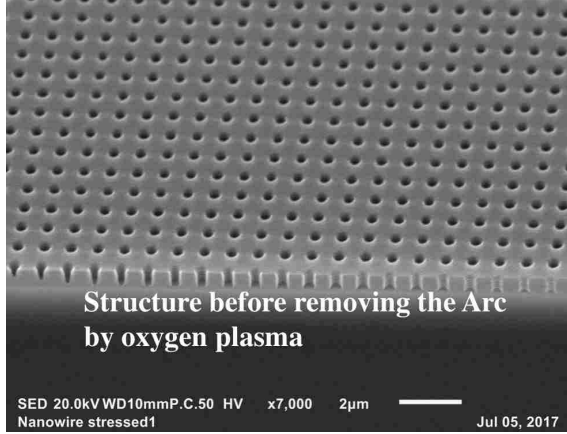
Figure 2.5: SEM image of the 2D nano-hole periodic pattern generated on photoresist before metal deposition.

A recipe of 2D IL patterning, has been shown in table 2.1. As can be seen light exposure time and post exposure bake both play critical role in dimension of the nano-holes developed after patterning (and backing which is done after light exposure). In all cases the power of the $3ns$ pulsed UV laser beam (355nm) is $5Watts$, and temperature of the post exposure bake is 110^{oC} developed using $MF_{321}^{TM}/H_2O = 3/1$ solution for 90 seconds.

Table 2.1: **Recipe for 2D IL patterning Using a** $5Watts$, $355nm$ **UV laser**

Exposure Time (s)	Resulting Photoresist Disk Diameter (40 seconds post-exposure bake)	Resulting Photoresist Disk Diameter (60 seconds post-exposure bake)
50	Not Developed	$170nm$
12	Not Developed	$220nm$
10	Not Developed	$260nm$
8	$200nm$	$310nm$
7	$230nm$	$350nm$
6	$300nm$	$420nm$

Note that the structure in Figure 2.5 is a 2D array of holes, because a negative

photoresist is used. We can obtain an array of disks instead of holes, if positive photoresist is used. The last point that needs to be considered in the case of 2D interference lithography is the nonlinearity of the photoresist. Because of this effect the edges of the pattern, which is expected to be rectangular, are rather curved after developing the resist. If the dimension of the feature size is small enough, the resulting shape after developing will be circular. The shorter the laser wavelength, the sharper the developed edges become and for getting circular patterns we must over expose the resist. 2D IL can be done for sample rotation angles other than the 90° mentioned, which can yield different features, like elliptical holes.

Metal Deposition

Although theoretically, the photoresist is developed and washed off of the holes (Figure 2.5), the underlaying Arc needs to be removed to expose the silicon substrate. A low energy oxygen plasma (Reactive Ion Etching or RIE) is used for this purpose. This process is also known as "ashing". After this procedure a $40nm$-thick Chromium or Nickel layer is deposited on the surface using electron-beam evaporator. Since the deposited metal layer is much thinner than the photoresist layer, the unwanted metal and photoresist can easily be removed by lift-off. Note that Acetone in the lift off process is not capable of removing the antireflection coating. A final oxygen plasma ashing is used to remove the left over antireflection layer. The result is a 2D pattern of deposited metal as shown in Figure 2.6.

2.2.4 Using IL For Creating 2D Nanostructures

In principle interference of two beams of light creates bright and dark regions with similar widths. Although exposure time as well as beam or photoresist imperfections can affect the pattern as shown in figure 2.4 for 1D case and in figure 2.7 for 2D
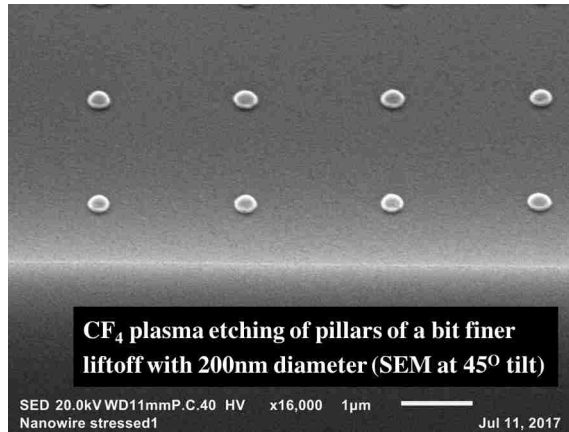
Figure 2.6: Metal Cr disks of 40 nm thickness and 300 nm diameter fabricated using interferometric lithography.

case, typically the exposed and unexposed regions are expected to have comparable widths

In the following sections we will discuss how to create patterns with unequal dark and bright regions and therefore samples with duty cycles larger or smaller than 50%.

Using IL for Creating Small Feature Sizes With Large Pitch Values

In this section, the aim is to change this equality between the widths of exposed and unexposed regions and generate samples where the feature sizes are merely a fraction of the distances between them. The features fabricated will thus be relatively far away from each other, enabling one to study the interaction of light with an individual feature (nano structure) rather than the overall effects.

In order to achieve considerably large ratios between the gaps and diameter of the features, one must increase the exposure time and reduce the post-exposure bake time. Increasing the exposure time will cause more of the photoresist to be exposed reducing the feature sizes however it can lead to incomplete development.
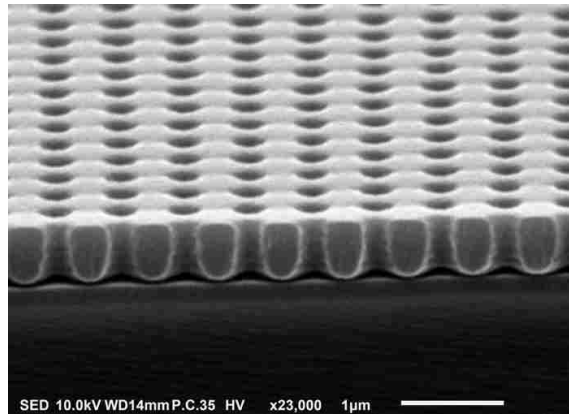
Figure 2.7: 2D photoresist patterned created by the IL setup and $355nm$ UV laser beam creating the low-pitch periodic nanopatterns on the photoresist. This has been done by increasing θ (see figure 2.1).

Reducing the post exposure bake time can overcome this problem and result in proper development of the photoresist.

(a)   (b)
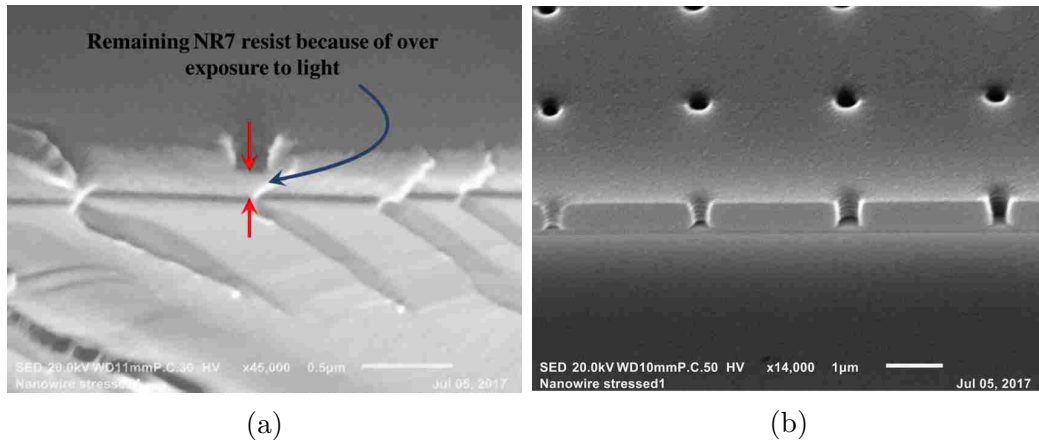
Figure 2.8: Creating high pitch PR pattern. (a) Over exposure of the PR (50 seconds at $5Watts$, post bake $60s, 110^{oC}$) showing the hole are not developed all the way to the ARC interface (Incomplete development means the photoresist is not removed completely from the holes during the development) (b) Reduction of post exposure bake to $40s, 110^{oC}$, improved the quality of the pattern and the holes.

Figure 2.8 shows a high pitch pattern created on a PR layer with $500nm$ thickness over $70nm$ antireflection coating. Figure 2.8(a), illustrates the incomplete develop-

ment and existence of left-over photoresist as a result of over-exposure (Incomplete development means the photoresist is not removed completely from the holes during the development). Figure 2.8(b) is fabricated by over exposure (50 seconds at $5Watts$) and reduced post-exposure time (40 seconds at 110^oC). As evident from the figure the photoresist is completely developed. The features have a diameter of sub $200nm$ and are located at a distance of $2.1\mu m$ from each other.

It should be noted that both, the light exposure and baking help in polymerization of our resist. The difference is that baking affects all of the photoresist film while light plays role in polymerization of only the exposed parts. Increasing the light exposure time reduces the feature size because, between the two exposed and unexposed regions, there are "semi-exposed" regions and by overexposure, polymerization occur in those regions as well. This and the nonlinearity of the photoresist polymerization (response to light), are the two main factors in reducing pattern dimensions as intended here.

As a final step, a low energy oxygen plasma is used to remove the anti-reflection coating from the bottom of the holes and exposing the underlaying silicon for metal deposition and further processing of this sample. Note that any left over photoresist can prevent proper adhesion of the metal mask to the silicon substrate resulting in improper etching.

To summarize, the coated photoresist in this approach has a thickness of $500nm$ and sits over the antireflection coating($100nm$). The exposure time in the case of small pores of figure 2.8 is 50 seconds and the power of UV ($355nm$) pulsed laser has is $5watts$. The post-bake time must decrease 30% while the developing time increases 30% (to 1 minute). The antireflection coating was removed by a $50Watts$ oxygen plasma, applied for $60seconds$ under $15mTorr$ ($15sccm$).

Using IL For Creating Large Features With Small Pitch Values

For certain applications (e.g. nano-pillar arrays used as anti-reflection coatings) the feature size has to be larger than the period, e.g. considerably larger than 50% of the period. In particular for antireflection structures, two main requirement should be satisfied. First, the pitch should be small (considerably smaller than the wavelength of light). Second, the 3D shape of the resulting nano-pillars should start from a pointy tip, comprising 0% of the unit-cell cross-section area, and gradually increase to 100% as the base of the nanopillars. In other words, the second condition means the pillars should merge with each other at the base. As shown in figure 2.9 first condition is satisfied by limiting the pitch to $630nm$. In order to satisfy the second condition, the metal masks should be in the form of circles circumscribed by the square of the unit cells. This means the circular patterns of the metal masks will be touching each-other each other as illustrated in Fig 2.9. The side view will be a continuous thin film over the bulk silicon and will not yield any useful information. For creating the highest diameter of the holes possible, the resist is under exposed while the post bake time is 60 seconds (instead of 40 seconds for high pitch case). Also the developing time decreases from 90 to 60 seconds due to lower mechanical stability of the photoresist.

Figure 2.10 shows an example of metal mask fabricated using a PR pattern generated by the above mentioned technique. This sample was fabricated using $500nm$ of NR7 photoresist on top of $70nm$ of ICON7 antireflection, covering a silicon substrate. The photoresist was exposed for $7s$ at $5Watts$, exposed again after rotating the sample by 90°, and post-baked for $60s$ at 110^{oC}. $40nm$ of Cr layer was deposited by e-beam evaporation. the unwanted metal and photoresist can easily be removed by lift-off. The reduced laser exposure results in larger pore size on negative photoresist.

The sample of figure 2.10(a) shows considerable non-uniformities of the metal
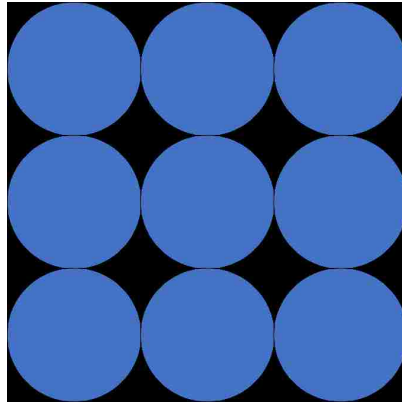
Figure 2.9: The ideal metal mask for fabrication of nano-pillar array used as nano-structured anti-reflection coatings is an array of circular metallic pads circumscribed by the square unit cells.
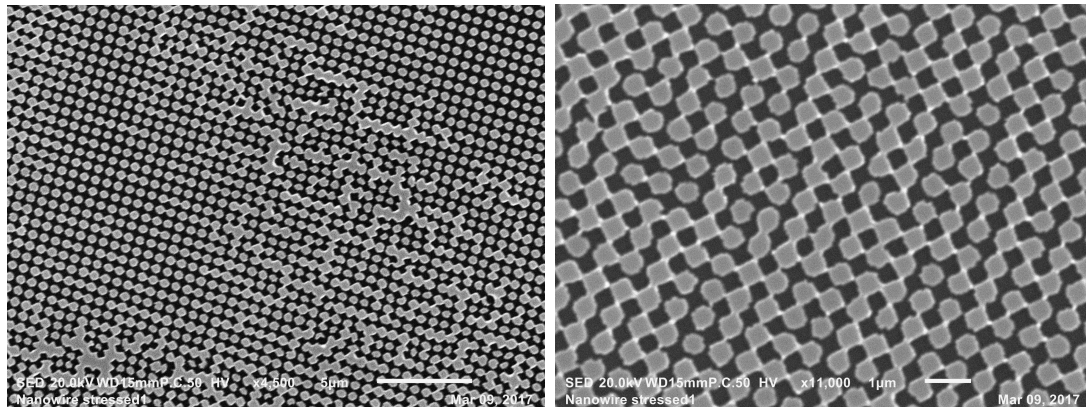
(a)	(b)

Figure 2.10: Top view of a metallic mask with high duty cycle (after lift off). (a) Small magnification to show defects caused by imperfections in photo-resist. (b) Close up view of a region.

mask with some regions completely fused into each other while figure 2.10(b) represents a much better quality metal mask with distinct circular regions, barely touching each other on four sides.

The non-uniformities observed in figure 2.10(a) are mainly in the form of metallic regions merging with each other rather than touching. These issues are more

pronounced at smaller pitches and thus need special consideration. The main reasons of these non-uniformities, superimposed on the main pattern, can be any or combination of the following:

- Non-uniformities in photoresist thickness

- Aged photoresist

- contaminations in photoresist

- Imperfections in the laser beam

The non-uniformities caused by photoresist degradation and contamination were eliminated by using a new photoresist. These laser beam imperfections were caused by diffraction from dust particles on the optical components as well as any dust particle floating in the air, which may have landed on the surface of the resist. Most of these imperfections were successfully eliminated. The sample of figure 2.10(b) is an almost ideal metal mask for fabrication of nano-pillars used as anti-reflection coating.

To summarize, it's also worth mentioning that for achieving the pores with diameters as large as the unit-cells (at $630nm$ pitch), the exposure time was reduced to 7 seconds (for comparison, fabrication of the half-duty-cycle samples would require 9 seconds). The reduced exposure time means the photoresist is not properly cured and therefore due to reduced mechanical strength of the polymerized resist (by exposure to UV light) it should be developed for a shorter time. Therefore the developing time is reduced for 30% from $90s$ to $60s$. After developing the photoresist, an oxygen plasma was used to remove the antireflection coating and expose the silicon before metal deposition. The plasma had a power of $50Watts$ and a pressure of $15mTorr$ ($15sccm$ O_2 flow). The sample was exposed to the plasma for $90seconds$. The thin

Cr or Ni layer was deposited using e-beam and then lifted off using an acetone gun. Afterwards the ARC layer was removed by oxygen plasma.

2.3   Etching The Nanopillars Out of Silicon

The metallic pattern created using one of the techniques descried in Sec. 2.2.4 (resulting from the IL, photoresist development, metal deposition and lift-off), is used as the mask to etch the exposed silicon regions and create the desired silicon structures (nano- pillars protruding off the silicon substrate). It is important to note that, photoresist can not be used as a masking material in plasma etching. The reactive ion etching (RIE) system used generates a plasma using O_2 and CF_4 gases. The plasma will produce free radicals and ions which will be accelerated toward the sample. Free radicals and ions can both etch the sample. The etching process and thus the nano-pillar profile can be tuned by controlling the exposure time, CF_4/O_2 flow-rate, Reactive-gas pressure, chamber-pressure, RF-power and etch time. As mentioned earlier in this chapter, dry etching can be used for isotropic, anisotropic or a combination of isotropic and anisotropic etches. Although pure isotropic and anisotropic etches are common too, in practice using a combination of both can offer a more diverse range of profiles. In this section a discussion of different etches, the mechanisms behind them and their distinct profiles will be discussed.

For anti-reflection, nano-textured coating application the nano-pillars should have a conical shape where the pillar cross-section decreases linearly as a function of pillar high. This is generally achievable by isotropic or a combination of isotropic and anisotropic etching. For field enhancement and plasmonic applications typically a more uniform cross-sectional area along the pillar is desired. This profile is achievable mainly by anisotropic etch or a combination of isotropic and anisotropic etch (RIE).

2.3.1   Isotropic Etch
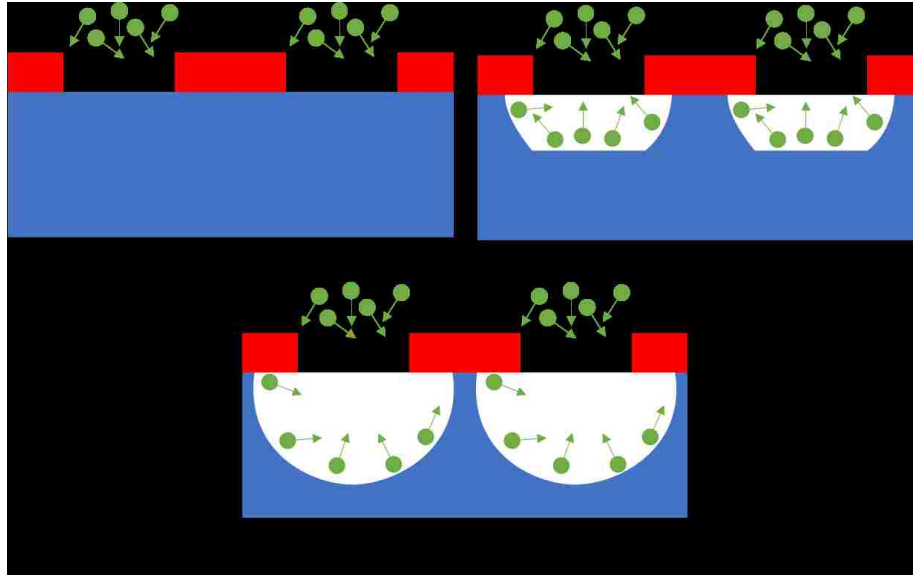
Figure 2.11: Reactive Ion Etching, isotropic etching

Figure 2.11 illustrates the isotropic etch progression. As the reactive species move toward the sample they collide with each other, changing directions. Thus the molecules move in random directions but their overall speed is toward the sample (see Fig. 2.11(a)). Once the reactive species reach the target, they will chemically react with the target molecules producing volatile gases that leave the chamber. Even these gases can collide with reactive species. The isotropic nature of the etch is controlled by the chemical etching which happens at the same rate everywhere (see Fig. 2.11(b & c)). Initially the etch moves downward since the initial exposed surface is flat ((see Fig.2.11(a))) but as the etch continues the edges smooth out ((see Fig.2.11(b))) and the etch profile gets spherical as illustrated in Fig. 2.11(c). The factors that are important to achieve isotropic etch are the chamber pressure and RF power.

Figure 2.12 shows two samples etched isotropically.The sample of fig. 2.12(a) was
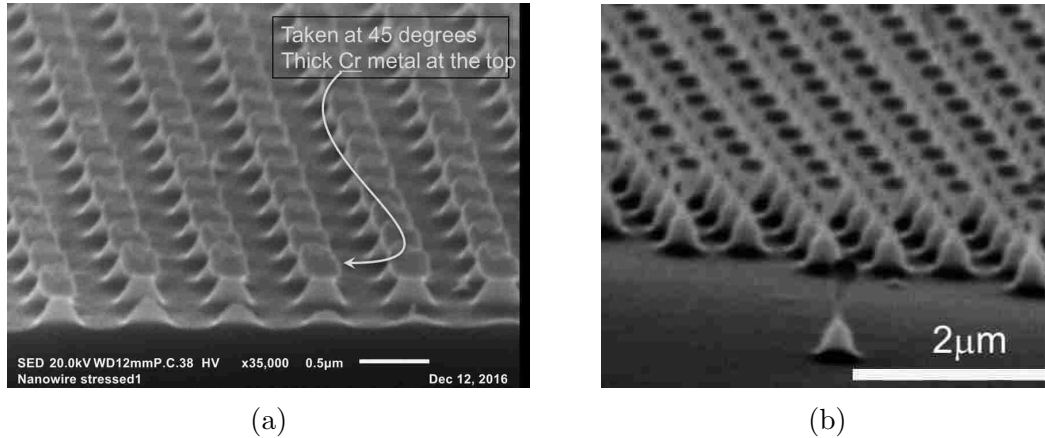
Figure 2.12: Isotropically etched silicon at different levels of oxygen and CF_4/O_2 at $50Watts$ (a) $CF_4/O_2 = 35/1$ (a) negligible under-etching beneath the metal mask at 25 minutes. (b) Isotropic etch can reduce the diameter to deep sub-micron dimensions.

fabricated using a metal mask with a period of $650nm$. The etch chamber pressure was $20mTorr$ with the flow rates of oxygen and CF_4 equal to $2SCCM$ and $35SCCM$ respectively. The sample was etched for 25 minutes at a power of $50Watts$. The sample of 2.12(b) was fabricated from a metal mask having a the same period. The etch chamber has a pressure of $20mTorr$ while etching using only CF_4 gas with $70Watts$ power. Then with the flow rates of oxygen and CF_4 equal to $3SCCM$ and $35SCCM$ respectively the sample was etched. The sample was etched at $50Watts$ for $20minutes$. The introduction of oxygen in the chamber has prevented the surfaces from being covered by a Teflon layer. This, in conjunction with the relatively low power, has made the etch isotropic. The sample of fig. 2.12(b) is significant in the fact that it represents the capability of fabricating samples with critical dimensions as small as $75nm$. The top sides which were initially etched by vertical etching (without oxygen) have become thinned considerably and the bottom side which is just etched isotropically has a tapered profile.
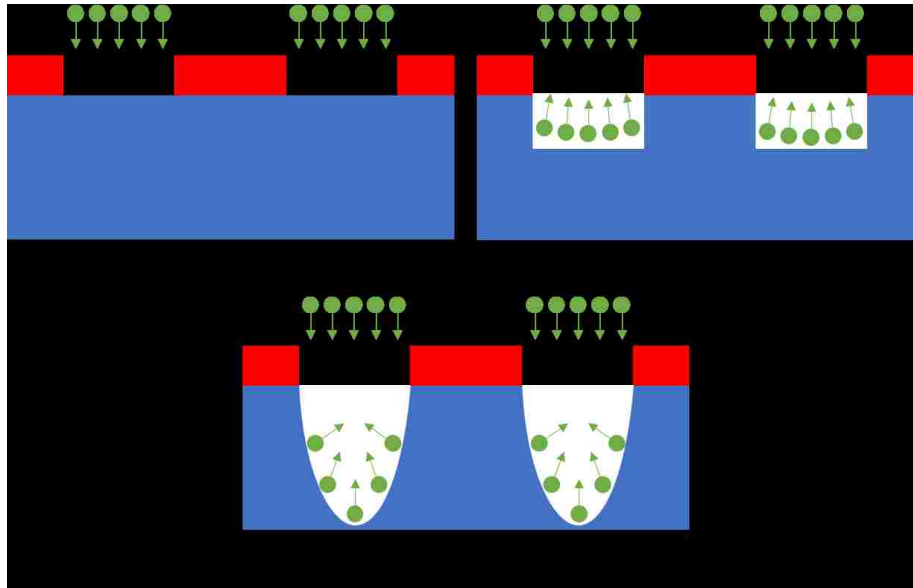
Figure 2.13: Reactive ion vertical etching

2.3.2 Anisotropic Etch

Anisotropic etch is a "line of sight" etch in which, the etching happens only in the direction of the ions. Anisotropic etch is mainly a mechanical etch achieved by bombardment of the sample with high energy ions. The ions are accelerated toward the sample and knock out target molecules upon impact. The RF power is generally higher to increase the momentum of the ions and the pressure is lower to increase the mean free path. Higher momentum will help with removing of materials upon impact and will also guarantee smaller deviations in ion-directions even in case of some collisions in their path toward the sample.

Figure 2.13 illustrates the anisotropic etch. As seen in Fig. 2.13.(a) the ions are accelerated toward the sample with high momentum. The ions have enough energy to remove molecules from the target upon impact and thus "dig" into the sample as illustrated in Fig. 2.13.(b). But as the etch gets deeper it gets more difficult for the produced gases to leave the chamber cavity and the collisions increase. These

collisions can eventually modify the nature of the etch and introduce some isotropic characteristics as well. This is usually an unwanted effect since as illustrated in Fig. 2.13.(c) it prevents the anisotropic etch to proceed vertically down and changes the etch profile [40]. One method to overcome this, is to cover the side walls with a layer of Teflon and protect them from being etched. The Teflon forms when the carbon radicals reacting with other radicals present in the chamber and covers all surfaces [115]. However the Teflon gets removed from the "line of sight" surfaces as soon as it forms. The Teflon deposited on the side walls protects them from reactive species helping the etch to proceed anisotropically for much longer [39, 97]. This method is illustrated in Fig. 2.14.
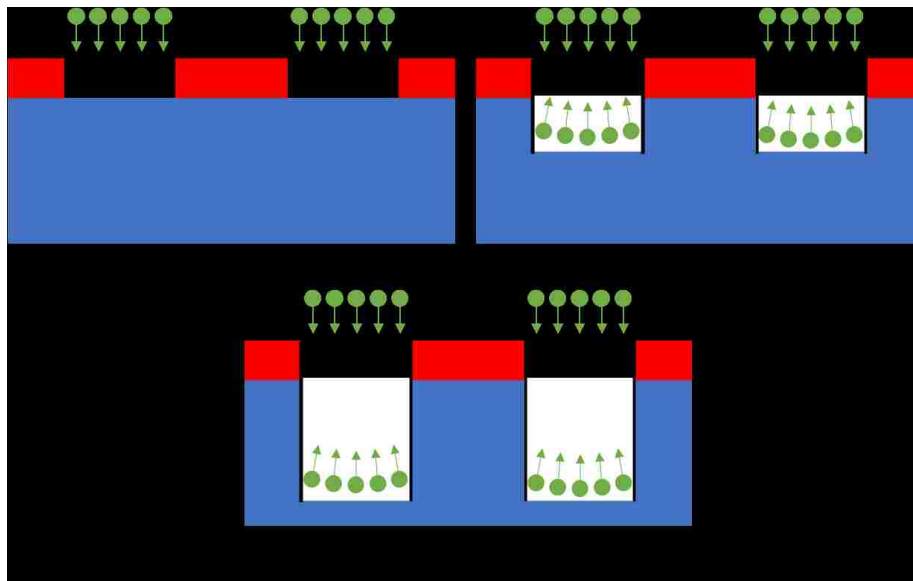
Figure 2.14: Deep reactive ion etching. The vertical surfaces of silicon are protected by a polymer formed by plasma gas chemical reaction with silicon.

Figure 2.15 shows an array of nano-pillars etched anisotropically. This sample was fabricated with using the same metal mask of fig. 2.12(b), the only difference being the type of etching. The pressure of the chamber was set to $15mTorr$. The $CF_4 : O_2$ ratio was $35 : 2$. The sample was etched for 25 minutes at a power of
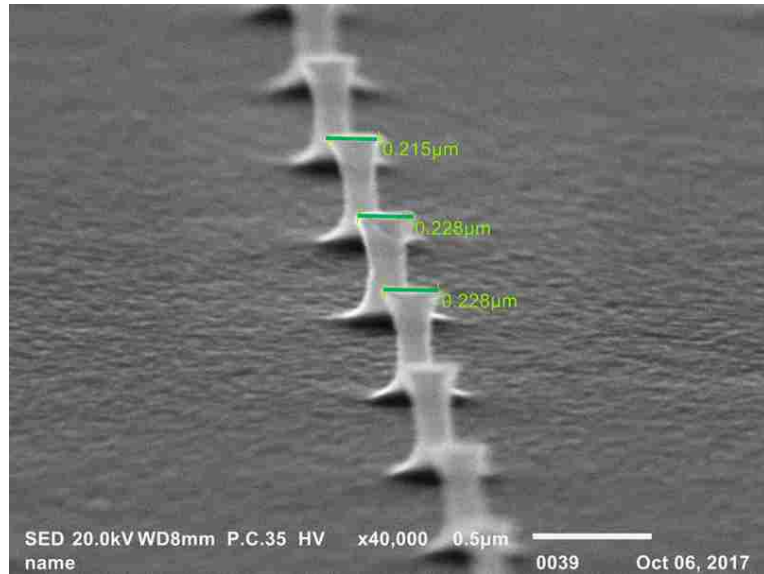
Figure 2.15: Cross section of the silicon nanopillars carved out of the silicon wafer nanopillars with diameter of approximately $230nm$.

$100Watts$. Some side etch is visible in the close up view of fig. 2.15. As explained earlier in this section, this was expected.

Figure 2.16 shows an other array of nanopillars fabricated anisotropically. The sidewalls of this sample doesn't show any sign of side etch, making this etch a completely vertical one. This is achieved by fine-tuning the etch process in such a way that side walls are completely protected and the etch happens only in the line-of-sight surfaces. The chamber pressure was $15mTorr$ and no oxygen was allowed in the chamber. The sample was etched for 25 minutes at $70Watt$. Although the lower power suggests that the etching will be rather isotropic, Teflon deposited on the side walls emerges as the prominent role player.
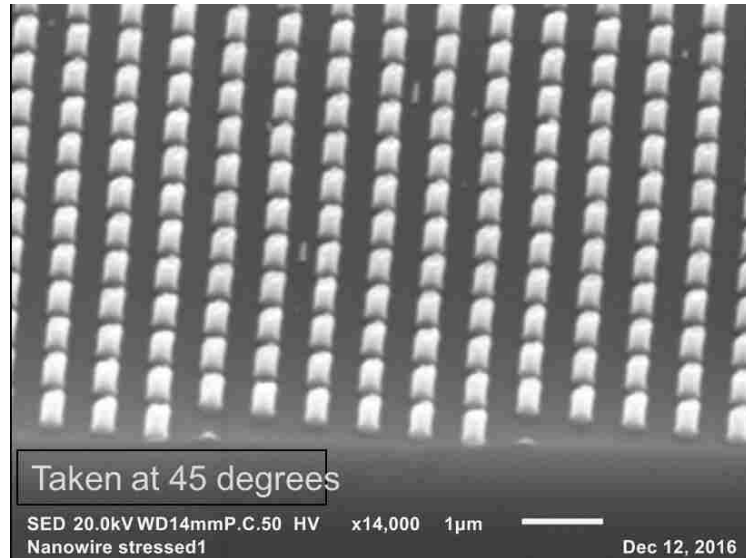
Figure 2.16: Nanopillars Carved out of the silicon wafer (a) The cross-section of the nanopillars etched out of silicon by CF_4. The period is $0.63\mu m$ and the pillar height and diameter are $490nm$ and $sub-200nm$ respectively. (b) Closer view of the cross section of the nanopillars showing nanopillars with diameter of approximately $190nm$

2.3.3 Combined Isotropic And Anisotropic Etch

As discussed in Sections 2.3.1 & 2.3.2, isotropic and anisotropic etches are two distinct etching methods. Each method has its own signature shape and both are equally important. However etches are seldom 100% isotropic or anisotropic. This is due to the fact that the physical and chemical etching mechanisms are always competing each other. A combination of the two methods can open the door to the possibility of fabricating a wide range of etch profiles. Figure 2.17 is one such example. This sample illustrates tapered nanopillars with linear sidewalls. If we cut the nanopillars by a plane parallel to the substrate, the cross section area of the pillars decrease from base to the tip. We later, in chapter 4, will use these kinds of gradual change of cross section areas. This sample was fabricated at a pressure of $10mTorr$ with a $CF_4 : O_2$ ratio of $35 : 5$. The RF power was $70Watt$ and the procedure took 20 minutes.
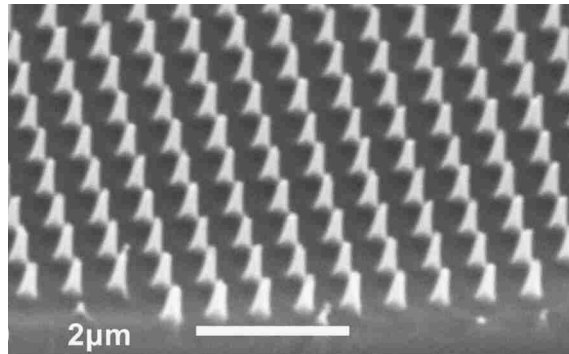
Figure 2.17: Sharp tips using a hybrid of isotropic and anisotropic etching.

2.4 NanoPillars as A Platform for Field Enhancement

While the tapered nano-pillars of Figure 2.17, with their tilted sidewalls and relatively pointy tips, are useful as nano-structured anti-reflection coatings, the nano-pillars of Figure 2.15 or 2.16 that have more vertical side walls (the side walls are closer to 90°) and flats top can serve as platforms for deposition of multilayer structures. Building up a metal-dielectric stack on top of the nanopillars of Figs. 2.15 or 2.16 can turn them to sites for producing optical field enhancement for Raman spectroscopy.

In order to create a stack of desired materials on top of the nano-pillars, the metal mask which was protecting the top surface of the nano-pillars during etching processes, is removed in acid etchant. Then a layer (or layers) of selected materials (mainly metallic) is deposited on the exposed top-surface of the nano-pillars. Figure 2.18 illustrates the steps taken for this purpose. The nanopillars fabricated as discussed in section 2.3.2 are topped with a metal as illustrated in fig. 2.18(a). This metal layer is used solely as an etch mask and needs to be removed before any further processing. This is accomplished by submerging the sample in metal etchant solution(see figure 2.18(b)). Once the masking metal is removed, electron-
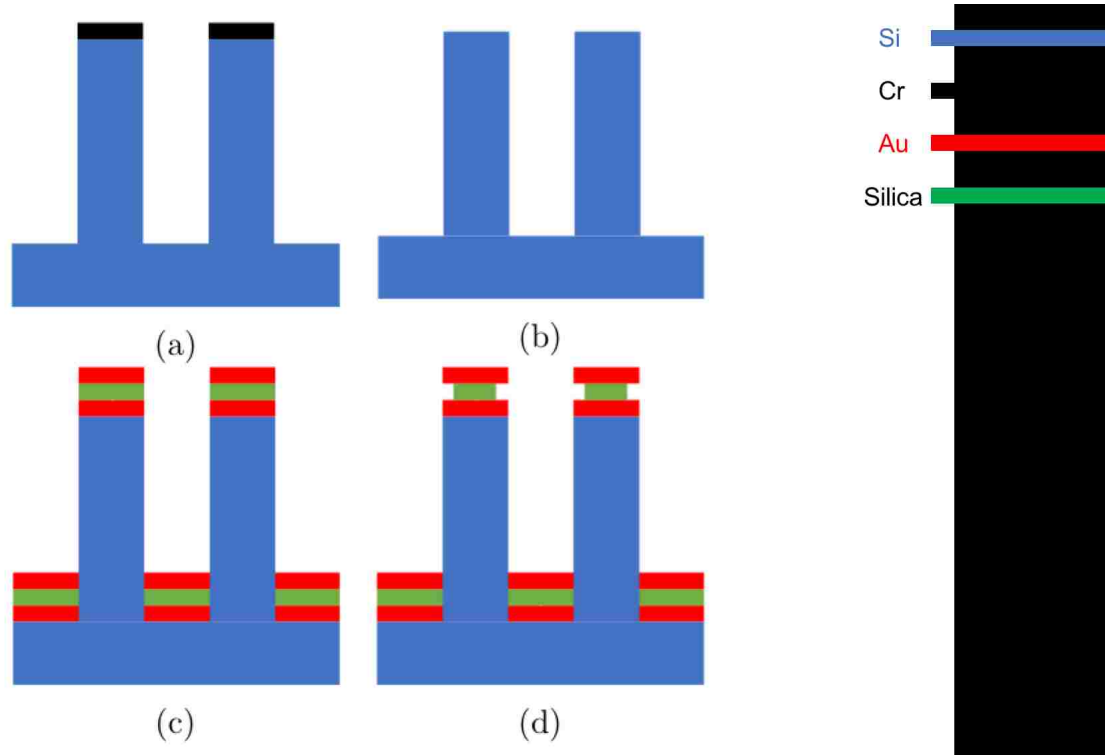
Figure 2.18: The fabrication process used to build a MIM-stack over SiNPs. (a) The fabricated SiNPs as described in figure 2.3(e) are fabricated with the metal mask still intact (Cr). (b) Metal mask is removed to expose the Si top-surface of the nanopillars. (c) A metal/dielectric/metal stack is deposited using e-beam deposition. (d) The dielectric between the two metallic disks of the stack is radially etched from the sides.

beam deposition is used to deposit one or more layers as illustrated in fig. 2.18(c)). The deposited layers cover the exposed top surface of the nanopillars as well as the substrate. The deposited layers are a sandwich of alternating metallic and dielectric layers refereed to as the metal/insulator/metal (MIM)-stack, in here. As a final step, the sample is dipped in a dilute HF acid bath. This radially etches the SiO_2 between the top and bottom metallic disks. The etch is done for only a couple of seconds. The goal is to remove SiO_2 from the rims of the metallic disks, as illustrated by the green layer in fig. 2.18(d). The etch rate may differ fro silica deposited by different methods [135]. Our oxide etches with rate of $150\frac{nm}{min}$, using a 0.4% diluted Buffer HF.

Depending on the materials used one can get different stacks with different properties. In this dissertation, the metals used for this purpose include Au, Cu, Ag and Al. These layers have a thickness of $25nm$. The dielectric layers are all made of SiO_2 and have a thickness of $15nm$.

In this dissertation we have also fabricated two samples using TiN and Ge instead of the metal layers. Neither TiN nor Ge are classified as metals. TiN is a semi-metal and Ge is semiconductor. However they have proven to outperform some metals in generating active plasmons in visible range, when treated with a plasma. Some metals actually fail to generate active plasmons in visible range. The fabrication processes followed in these two samples are identical to others with the only difference being the fact that only one layer was deposited instead of a stack. The thicknesses of TiN and Ge layers in their corresponding samples were $40nm$ and $25nm$ respectively. The samples were treated with $60Watt$, $200mTorr$, NH_3 plasma for 10 minutes.

Figure 2.19 shows a set of nanopillars coated with a stack of $Ag/SiO_2/Ag$ layers. The MIM-stacks on top of the nanopillars are better visible in the insets (which show the same sample at higher magnifications) and are used in Surface Enhanced Raman Spectroscopy (SERS). Once the stack is fabricated, the sample is submerged in a diluted Buffer HF [135] bath for 4 seconds ($150\frac{nm}{min}$, using a 0.4% diluted Buffer HF). This etches the $SiO2$ circumferentially ($10nm$ in the radial direction) exposing the rims of the metal nano-disks on top of the pillar. We have measured the etch rate for the oxide which is deposited using Ebeam evaporation.

2.5   Conclusion

This chapter provided details of each step and procedure used for fabrication of the nanostructures studied here. The custom made interferometric lithography system used here, is introduced and its operation mechanism is explained. The devices fab-
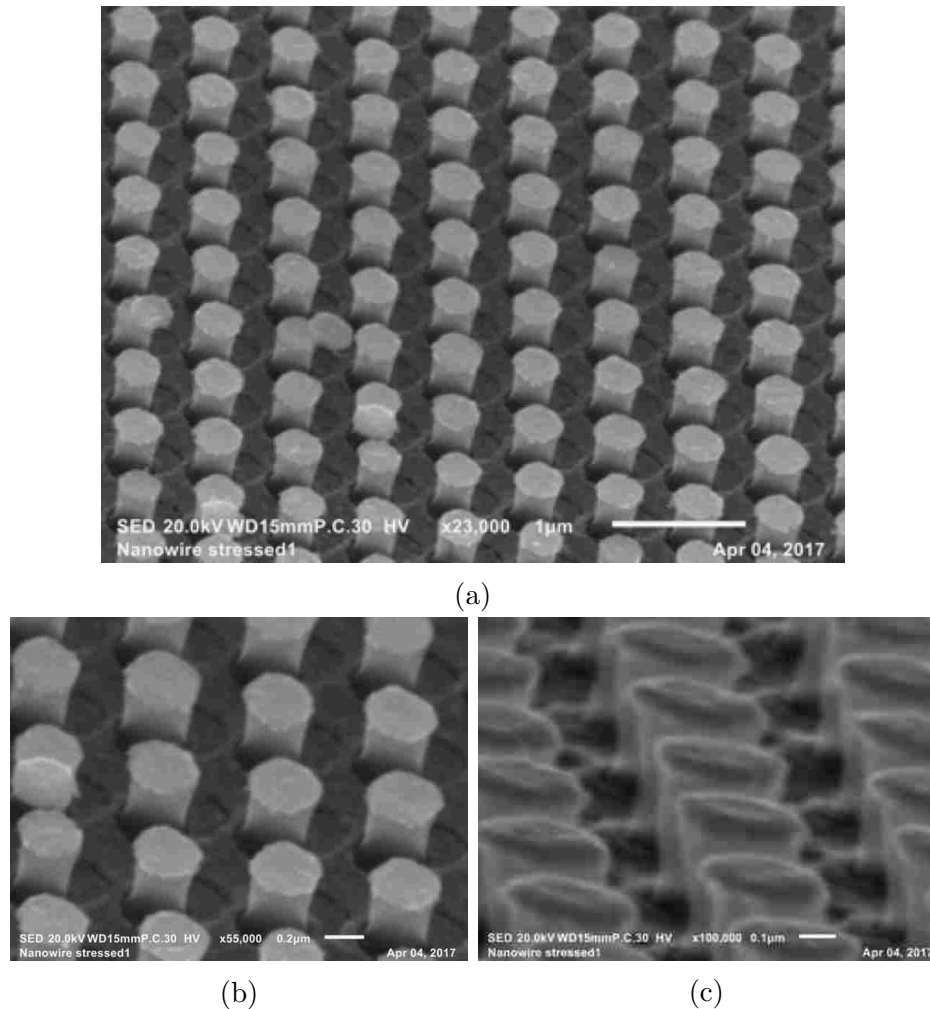
Figure 2.19: The nanostructure (Diameter of $330nm$)is coated with $Ag/SiO_2/Ag$. The fallen caps can be seen in some of the nanopillars. The cartoon in figure 2.18(d) shows the design (a) SiNPs with deposited Ag on top viewed from 45° angle (b) Closer view of (a), (c) the metal capped SiNPs viewed from 75° angle. The side etch is so small that can't be seen under SEM.

ricated in this chapter are divided into two main categories i.e. nanostructures used for NALs and nanopillars (with and without metal stacks on top) that are for Raman enhancement. The details of wet bench, interferometric lithography, metal-masks, lift-off processes and plasma assisted etching procedures are provided. Different processes used, allowed fabrication of different sample profiles ranging from semi-

parabolic to cylindrical structures. However this chapter didn't cover the deposition of metallic layers and metal/dielectric stacks over SiNPs or the surface treatments used in some samples. Since these are different from sample to sample, they will be explained on a case-by-case basis in Chapter 5.

Chapter 3

Measurement

3.1 Introduction

The measurements reported in this thesis are performed using a Fourier-Transform Infrared (FTIR) Spectrometer and a custom-made scattering measurement setup. FTIR is used for characterizing the IR transmission spectrum and the scattering setup is used for measuring elastic and inelastic scattering spectrum through and from nano-structured surfaces.

3.2 FTIR and Nicolet 10 iN Infrared Microscope

Fourier-Transform Infrared (FTIR) Spectroscopy is a fast and accurate method for measuring the infrared transmission, reflection, and absorption spectrum of a sample. The FTIR used in our measurements was a Nicolet 10 iN Microscope. Figure 3.1 illustrates the internal structure of this microscope. The operational principle of the microscope is shown in figure 3.2. A beam splitter is used to divide the light

coming from the mid-IR source, into two identical beams. One gets reflected from a fixed mirror and the other one, from a moving mirror. As shown in the figure both mirrors are corner cube mirrors. Besides improving mechanical stability, this also guarantees that the reflected beam is parallel to the original beam, reducing system complexity[1, 2]. The path length difference (and thus the phase difference) between the two beams results in constructive and destructive interference when the two beams are combined in the detector. Figure 3.2(b) shows a sample interferogram generated by the interferometer. A spectrum is obtained by performing a Fast Fourier Transformation (FFT) on the interferogram (Figure 3.2(b)). Besides the IR source, FTIR system is also equipped with a He-Ne laser source for calibration.
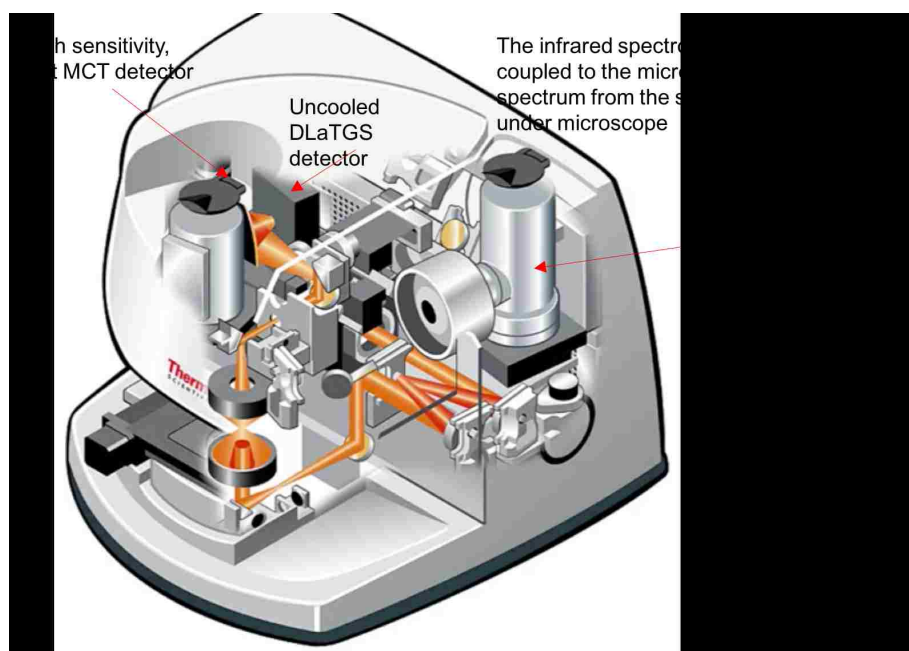
Figure 3.1: Internal structure of Nicolet 10 iN [2]

Before a successful measurement the device should be calibrated for the background transmission. This is done using an inert nitrogen atmosphere that fills the device chamber. The transmission of each sample is measured with respect to background for a range of IR wavelengths. The method can be used for solid, liquid, and

(a)

(b)
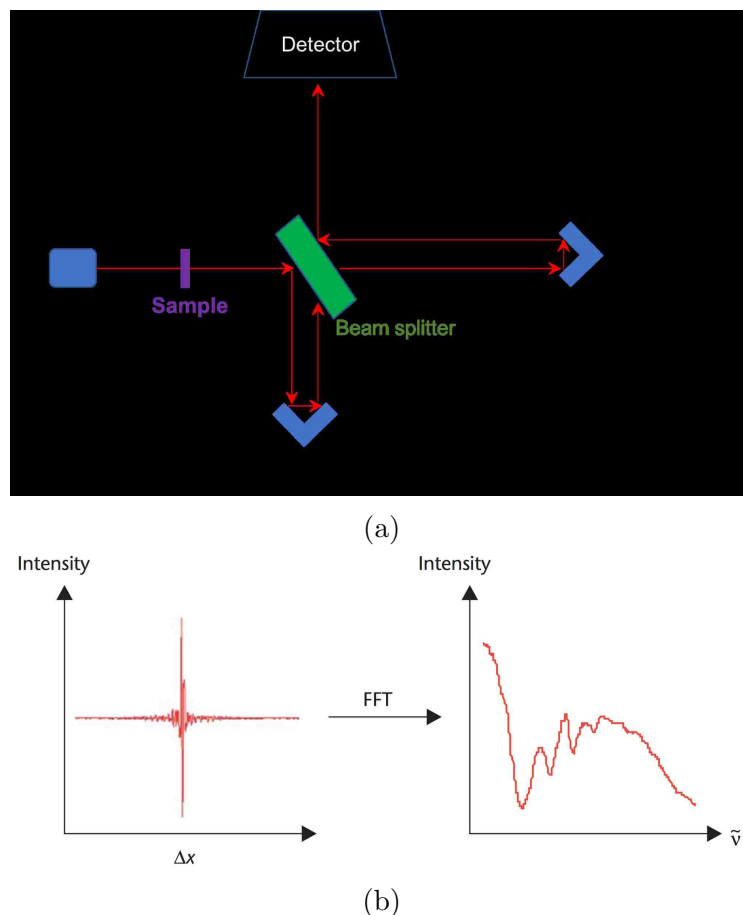
Figure 3.2: Operation principle of FTIR (a) Interference of the two beams for generating the interferogram. (b) interferogram versus Δx and the FFT from the interferogram showing the transmission of sample versus frequency [2]

gaseous samples. It can also be used both as a qualitative and quantitative method. Nicolet 10 iN is a fast and efficient FTIR tool capable of measuring IR transmission spectrum with high resolution in a reasonably small time interval. Figure 3.3 shows the optical path with in FTIR. As shown in the figure the IR beam is focused on the sample from the bottom and the transmitted beam is collected and guided to the top detector.

The angle of incidence for rays within the beam is between 25° to 45°. The two
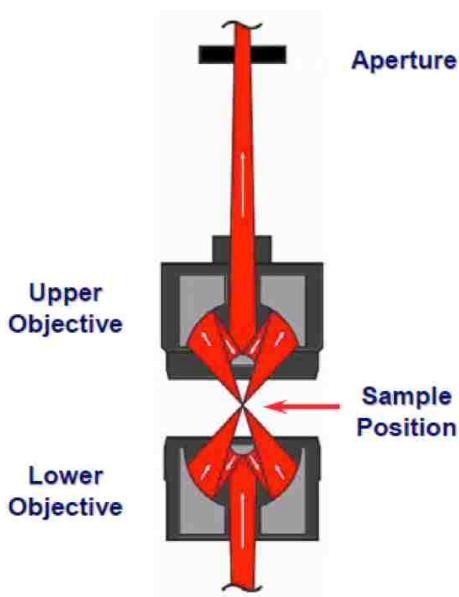
Figure 3.3: The optical path in Nicolet 10 FTIR

beams are focused on the sample passing to an $3 - 4\mu m^2$ area. In FTIR systems, the measurement speed can be modified, to address the state of the sample (gas, liquid, solid) and frequency resolution as well as signal to noise ratio requirements. Liquids and solids have broad natural line width, and don't require high resolution measurements (high resolution is not going to give any extra information about them) [2]. The device is equipped with a high speed interferometer which can perform up to 10 scans per second at $16cm^{-1}$ resolution and has the maximum resolution of $0.4cm^{-1}$. The range of wavelengths used for measurement can also be adjusted. One can also modify this easily using the settings available.

Nicolet 10 iN is equipped with two types of detectors. One of them works at room temperature, and the other one is cooled with nitrogen. The detector cooled with nitrogen provides higher speed and sensitivity. High resolution nitrogen cooled detector is used for measuring IR transmissions in all FTIR measurements performed in this dissertation. This detector is (MCT-A) works in spectral range of $7800cm^{-1}$

to $650cm^{-1}$ ($\lambda = 1300nm$ to $15400nm$). Before a measurement is performed on a sample one needs to make sure to clear the light path from any obstacles (such as a sample) and run the "Optimize" procedure. According to the manufacturer doing so, the system adjusts itself to maximize the amount of IR beam received from the source passing the vacuum space. This procedure needs to be run only once per each measurement session and is valid for all the experiments ran in one sitting.

In order to specify the exact location of the measurement the microscope is also equipped with an secondary LED light source which can be used to see a wider area ($500\mu m$) of the sample and make sure that the measurement will be performed on the correct spot of the sample. The measurement spot is specified by a cross sign in the center of the field of view. It is worth mentioning that the wavelength of the secondary light falls outside of the measurement range and will not affect the measurement.

3.3 Elastic and Inelastic Scattering Measurement

The Scattering Measurement Setup (shown in figure 3.4) is a home-made system that is capable of measuring both elastic and inelastic scattering. The light source can be a He-Ne laser or a lamp depending on the measurement. First part of this section will be focused on elastic scattering measurement and the second part on inelastic (Raman) scattering. The section will end with a discussion on Photoluminescence (PL) that usually interferes with Raman measurements.

3.3.1 Elastic Scattering

In an elastic scattering of light, the frequency and thus the energy of the scattered light does not change and remains the same as the incident beam. Here the elastic

scattering spectrum from the sample is measured when the the light is incident at a fixed angle. The scattering data reported are normalized to that of a bare silicon wafer. In all scattering measurements the temperature of the detector was maintained at approximately -70^{oC} (using liquid nitrogen).
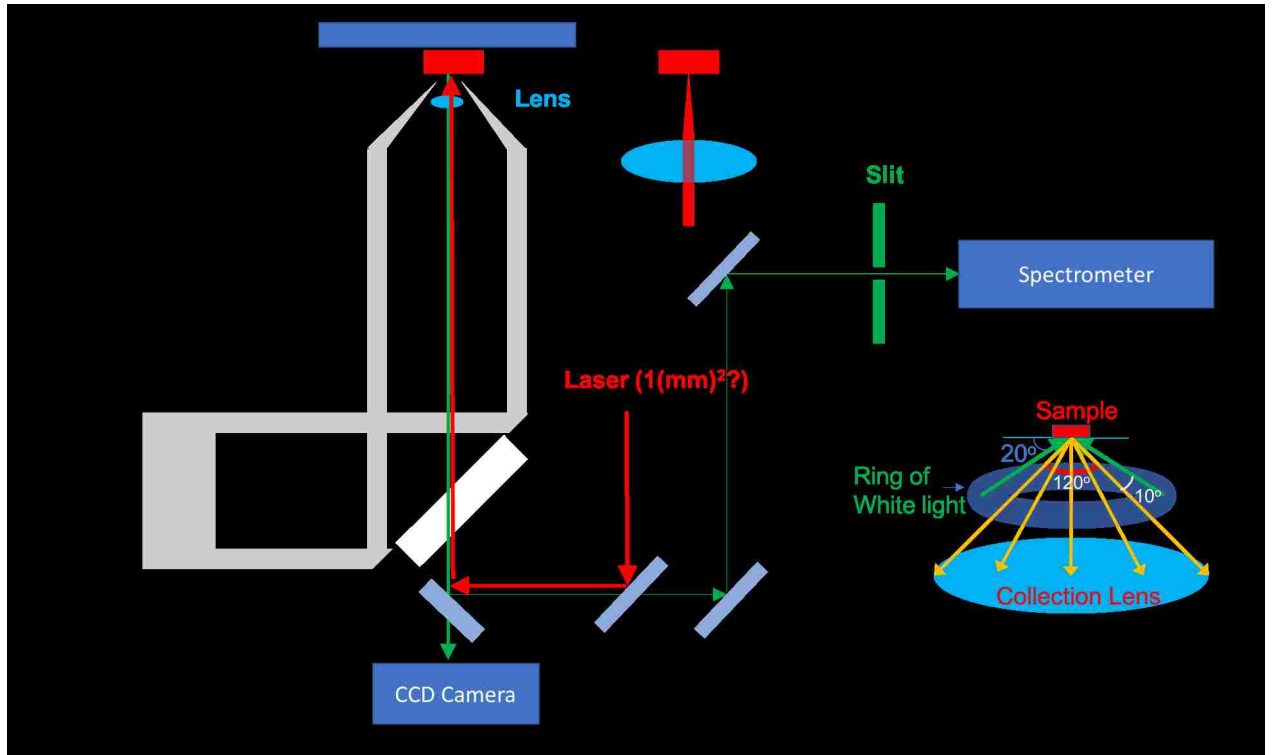
Figure 3.4: The Scattering Measurement Setup showing the incident and scattered beams

In this mode of operation, the incident beam comes from white light lamp (visible to near-IR spectrum). As illustrated, first a collimated beam is formed, then it's central region is blocked by an opaque disk resulting in an annular collimated beam of light (which is reflected towards the sample by a ring mirror). This beam is focused on the sample by a lens with NA of 0.9. The incident beam is focused on the sample with an angle between 20°-30^o(as shown in fig 3.4).The diffraction from the sample is collected over a 120° cone using the same lens. The collimated beam

from the objective is divided between a CCD camera (to generate an image of the sample) and a spectrometer (to measure the spectrum). Two $1200 grooves/cm$ and $150 grooves/cm$ gratings can be used inside the spectrometer. The grating diffracts different frequencies of light, pointing them toward different parts of the CCD. The CCD then generates the spectrogram. Note that the red ray, representing the laser and the mirror located between the beam-splitter (BS) and dichroic-mirror (DM) are removed in this mode of operation.
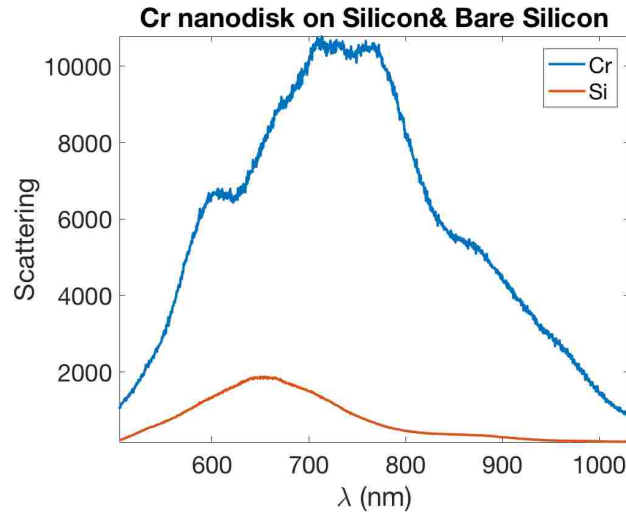
Figure 3.5: Scattering of Cr nano-plates lifted off over silicon surface. The pitch is $630nm$ and duty cycle is approximately 60%

The initial step in each measurement is to calibrate the device using a bare silicon wafer as the reference. After the calibration, one can measure the diffraction of different samples. Figure 3.5 shows an example of such elastic scattering data. This scattering spectrum is generated by nano-structures of Cr on a silicon (The sample was fabricated using Interferometric lithography). Chapter 5 will cover the scattering measurements in detail

Image Acquisition

The main CCD camera in illustration of Fig 3.4 is used to image the surface of the sample. The use of annular beam and capturing the 120° central portion of the light enables the setup to image deep sub-micron samples even using a regular incoherent white-light source. This is an obvious superiority over conventional microscopes. In figure 3.6 one can see an array of Nano-pillars with average diameter of $230nm$, and periodicity of $2100nm$.

20 µm
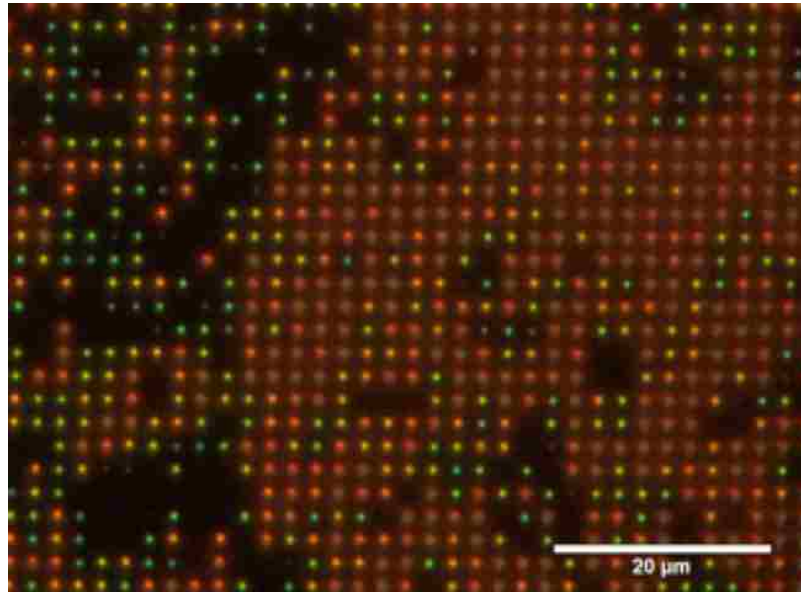
Figure 3.6: Bare SiNPs seen by microscope using CCD camera.

The difference in the height of the pillars beside empty (black) regions, can result in a difference in the scattered color, or equivalently different resonance frequencies inside the silicon nanopillars SiNPs (The missing nano-pillars are broken due to the mechanical stresses).

As an example figure 3.7 shows elastic scattering spectrum obtained from different regions of the sample shown in figure 3.6 using the $150groove/cm$ grating and white light illumination. It can be seen that the spectrum of the green region, as expected,

lies in green spectrum, but the intensity of this spectrum is significantly reduced.
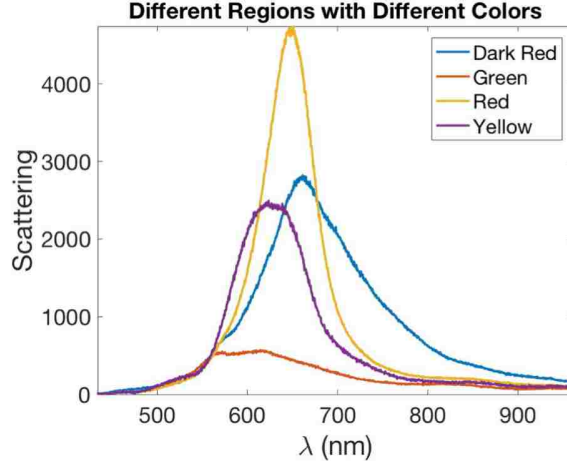
Figure 3.7: Spectrum of Bare SiNPs with $230nm$ diameter, $490nm$ height and $2100nm$ pitch scattering under white light

Figure 3.8 shows the uniform color of the image captured from the scattered light of gold nano-disks over SiNPs.The nano-pillars imaged here are $230nm$ in diameter however as the resolution of the system is limited by detected by the CCD the nanopillars in the image look bigger than 230nm (therefore one can not determine the diameter of nano-pillars using this microscope). The actual dimensions are measured using scanning electron microscope (SEM).

3.3.2 Inelastic Scattering

In inelastic scattering, the frequency of the scattered light is not equal to that of the incident light. In order to measure the inelastically scattered spectrum (and calculate the frequency shift relative to the incident beam), a narrow bandwidth laser should be used as the light source.

Here for measuring Raman (and Photoluminescence), a He-Ne laser with a wavelength of 632.8 nm is used as light source. As a part of the laser is also scattered
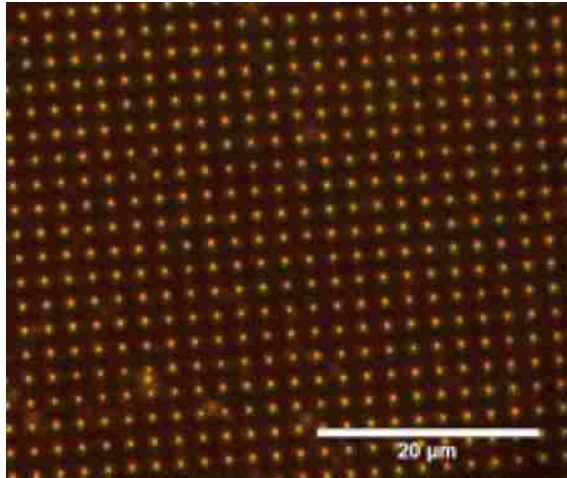
Figure 3.8: Photo of 230nm diameter SiNPs coated with Au layer, observed using the setup shown in figure 3.4. The pitch of the structures is $2100nm$. The dimensions are measured using SEM.

within the collection angle, high pass filter is used to remove $632.8nm$ light, so only the stokes shifted wavelengths reach the spectrometer.

For inelastic scattering measurement we use the high resolution $1200grooves/cm$ grating. Figure 3.9 shows the impact of the grating resolution on measured spectrum. Although it is not obvious in Figure 3.9, the finer resolution obtained by the $1200grooves/cm$ grating, comes with the cost of shrinking the bandwidth of the measurement. However this problem can be solved by "Stick and Glue" procedure. In this procedure, Raman data from multiple measurements covering different wavelength spans, can be combined to produce a single spectrum covering a wide range of frequencies.
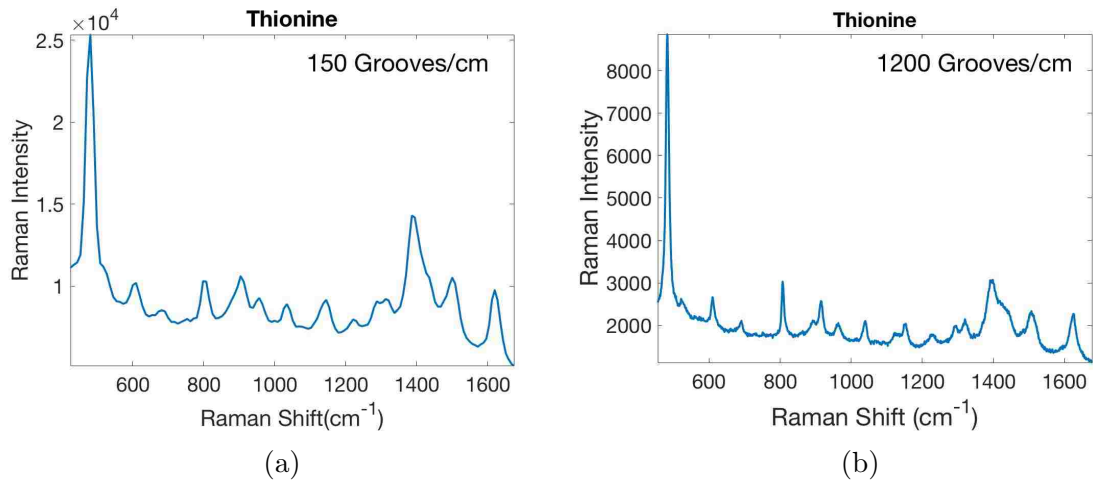
Figure 3.9: Measured Raman of Thionine by two different gratings. (a) Raman Spectra measured by a 150 grooves/mm grating. (b) Raman Spectra measured by a 1200 grooves/mm grating.

The power of the laser source can be adjusted in the 0 to $4mWatts$ range. However in order to prevent saturation of the detector it is recommended to limit the power to lower amounts, specially when scattering is caused by metallic nano-structures.
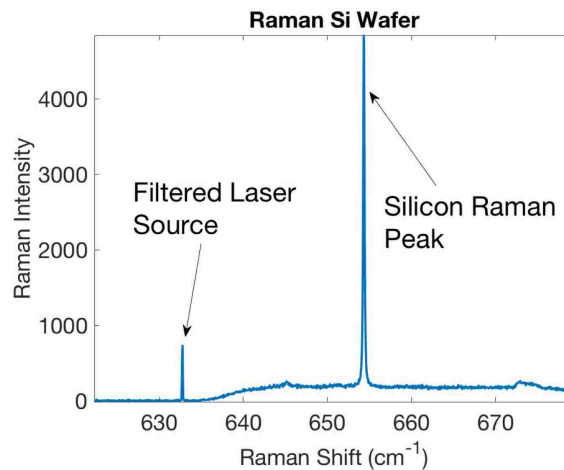
Figure 3.10: Raman Spectra of bare silicon wafer, peaking at $654nm$ corresponding to a Raman shift of $520cm^{-1}$. The small filtered laser signal is $632.8nm$.

The calibration of Raman spectrum is preformed by matching the Raman peaks corresponding to silicon. Silicon is selected for this purpose because it is the base of all the samples fabricated in this dissertation and also the silicon in the wafer, has only one type of bond yielding to a unique peak. Figure 3.10 shows the Raman signal obtained from a silicon wafer. The dominant peak corresponds to silicon and the the weaker peak belongs to the laser source which is attenuated by the high-pass filter before reaching the spectrometer detector. The Silicon peak is expected to have a shift of $520cm^{-1}$ from the laser used. For the He-Ne laser used here, this shift means that the silicon Raman peak should be located at $654.45nm$ as confirmed experimentally here. The measurement software can show the results, in the Raman Shift form, which is calculated by $(\frac{1}{\lambda_0} - \frac{1}{\lambda_0}) * 10^7$. The units of the resulting shift is cm^{-1}.

3.3.3   Photoluminescence

While measuring the Raman spectrum, PL is present in most Raman measurements as a background noise. The mechanisms or Raman generation and Photoluminescence are in some aspects very similar and sometimes Photoluminescence happens along side Raman. Choosing the laser source carefully decreases the PL substantially.

PL typically happens through band to band transitions while Raman is phonon-assisted phenomenon and happens by intra band transitions via virtual levels. Figure 3.11 illustrates the mechanisms for PL and Raman generation. Despite their different mechanisms both PL and Stocks-Raman result in signals with longer wavelengths compared to the excitation source (laser). Raman is the desired signal in all our measurements but PL generated by the target molecule is generally much stronger and can overshadow the Raman signal. Thus for evaluating the field enhancement by nanostructures one should choose molecules that generated PL at

(a)   (b)
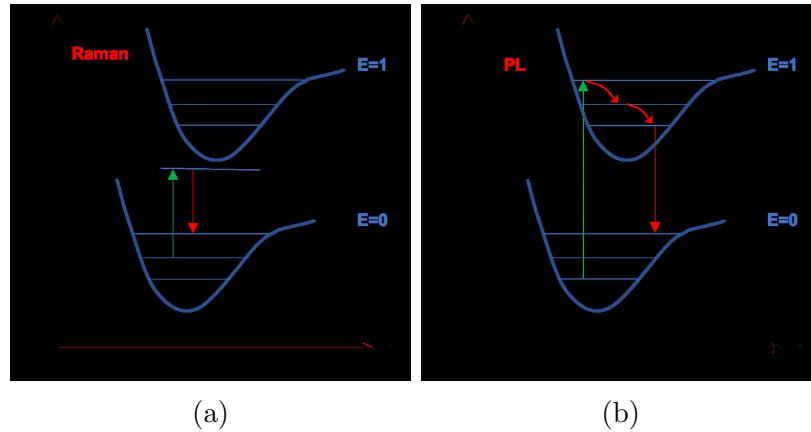
Figure 3.11: Inelastic scattering depicted versus Photoluminescence (PL) (a) Raman transition by a photon with energy less than band-gap excites the electrons to a virtual band, and by phonon assisted recombination generates Raman signal (b) Photon with energy equal or greater than band-gap excites the electrons to the electron conduction band and as depicted recombination from different conduction bands to the valence band can generate a broad PL pattern, depending on the excitation light and band structure.

wavelengths that do not overlap with the desired Raman Signal.

(a)   (b)
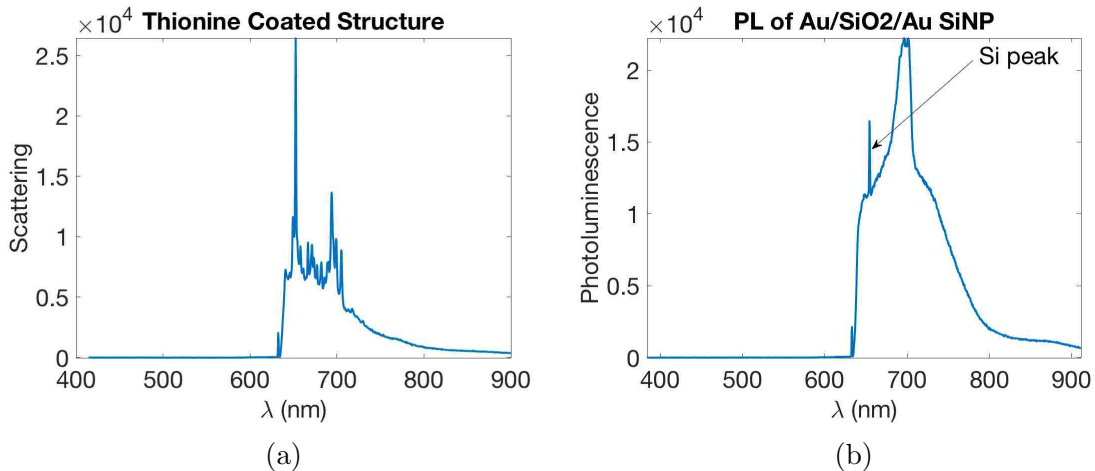
Figure 3.12: Measured Spectrum by 150 grooves/cm grating (a) Raman scattering spectrum of $Au/SiO_2/Au$ layer coated with thionine measured by $150 groove/mm$ grating. (b) Photo Luminescence of none-coated $Au/SiO_2/Au$ layer by $150 groove/mm$ grating.

The metallic nano-structures also generate PL. The source of this PL is plasmonic damping. The oscillating plasmons can radiate in a much wider wavelength range compared to the excitation laser. This happens through the band to band transitions inside the metal nano-plate, while the oscillating plasmon is oscillating in the metal nano-plate. Figure 3.12shows an example of measured scattering data. These plots illustrate the Raman peaks superimposed on the PL curve. Ideally one would prefer the overlap between Raman and PL frequency-spans to be as small as possible or have a PL signal which is smaller than the Raman signal. As will be seen in Chapter 5, besides other results, we have been able to achieve circumstances where the PL signal was considerably smaller than the Raman signal, allowing much better detections to be possible. The measurement setup (Figure 3.4) can detect both Raman and PL signals. To capture both signals the $150 grooves/cm$ grating is preferred as it allows measuring a broader spectrum.

3.4   Conclusion

Alongside optical microscopy, SEM, AFM, and ellipsometry, we have also used two other characterization tools which were highly crucial for this project. This chapter covered these two characterization methods, FTIR and Raman Spectroscopy. The specific FTIR used in this project is introduced and the basics of its mechanisms of operation are explained. The custom made Raman dark field microscope and different modes of its operation were also discussed in details. These equipment are equipped with white light as well as a $633nm$ HeNe laser source. The scattered light from the surface of the sample is guided toward the spectrometer for analysis through the same lens used for focusing the beam on the sample. For Raman measurement, a filter is added to the path of light scattered back from the sample, for filtering the elastically scattered $633nm$ red light.

Chapter 4

Nanostructured Antireflection Layers (NALs)

4.1 Introduction

When passing through the interface of two mediums, light can get reflected, diffracted, scattered or transmitted (see Fig. 4.1). This is due to the sudden change of refraction index at the interface. Using an intermediary medium, referred to as the "antireflection coating (ARC)", the overall transmission can be increased (The interference between the reflections from the two interfaces reduces the reflected intensity. If the refractive index of the antireflection layer is the geometric mean of the two, e.g. $\left(n_2 = \sqrt{n_1 n_3}\right)$, and its thickness is $\frac{\lambda}{4n_{eff}}$ then at normal incidence the reflection is zero.). These layers are called antireflection coatings since they started as thin homogeneous layers, deposited on the interface[145]. This is achieved using the established deposition methods such as thermal/electron-beam evaporation[147, 69] or plasma enhanced chemical-vapor-deposition (PECVD)[34] or sol-gel processes [32] which provide highly controllable deposition rates. By proper selection of the thick-

ness and refractive index, the presence of the ARC layer results in generation of two reflected waves (instead of one) with a relative phase of pi that cancel each other. The ARC layer should have a refractive index, intermediate to (ideally equal to the geometric average of) those of the two medium [36]. The effects of using an ARC is specially noticeable when the refractive indexes of the two medium differ considerably, to begin with [53, 145].
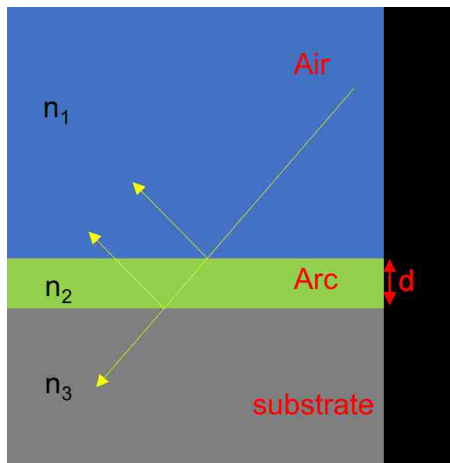
Figure 4.1: Illustration of light going from air (1) to an other transparent medium (3), through an antireflection-coating-layer (2) which uses destructive interferences of the reflected waves shown in yellow, for suppressing reflection.

A single layer of antireflection coating is not enough to achieve optimum transmission over a wide band range. Using multiple layers of ARC with proper refraction indexes and thickness reduces the reflection over a wider range of wavelengths and incident angles. There are two shortcomings to this approach though: 1) It is not always possible to find materials with the calculated refractive indexes 2) The difference in thermal expansion coefficients of the layers can yield to considerable residual stresses [12] and delamination, specially when high power lasers are used [137].

Nanostructured surfaces [41] (also referred to as Nanostructured Antireflection Layers or NALs in here), provide an alternative and much better solution. These are generally made in the form of an array of nanostructures. Both random and highly

controlled shapes are reported for NALs. The distribution of the nanostructures can also be random or organized. If all the nanostructures in a specific NAL sample have identical shape and are distributed with a specific order, the result will be a NAL in the form of a periodic structure which will not generate "grain-boundary scattering" in contrary to randomly distributed nanostructures.

The nanostructured antireflection layers yield increased spectral bandwidth and incident angle tolerances. Their main disadvantage is the potential increase in diffraction. At a first glance this can limit their use in LEDs [64, 79, 74] and solar cells [106, 33]. These applications require considerable light transmission and are not very sensitive to scattering. Also other applications such as transmission-windows for lasers [114] for example, require considerably lower scattering. Reducing the size of individual nanostructures (sub-wavelength) can considerably reduce the scattering of NALs, making them suitable for such demanding applications. Also, the pitch of the structure should be low enough to avoid diffraction effects.

The material to be used for a specific NAL is determined by the specific application as well as the fabrication method. Polymers have been used to fabricate NALs for low power applications such as light extraction from LEDs [149] [16] [62][64][79],[74]. They can be fabricated using nanoparticles spin-coated on a substrate [149], nano-imprinting[15] as well as more established lithography techniques. Moth-eye-shaped structures common for these NALs. Polymeric moth-eye structures are used over ITO for increased transmission ($400nm$ to $1100nm$) as well as increased hydrophobicity. Fused-silica moth-eye features, treated with chemicals to become hydrophobic, provide a wider transmission bandwidth ($400nm$ to $2300nm$) [80, 20]. A usual technique used for lithography of moth-eye structures is colloidal lithography. They are fabricated by plasma etching. The nano-spheres get etched while etching the substrate beneath them [86] creating a tapered profile. Silicon can be used as a mold to pattern a polymer over different substrates, like the one done over $GaSb$ surface by

Kanamori [63]. Chiu et al. [37] used Ni mask for nano-patterning the GaN surface. He created the Ni nanoparticles by annealing a thin layer ($10nm$) of Ni at 850^{oC}. This rapid annealing converts the Ni layer to numerous Ni-nanoparticles. Nano-particles are commonly used as masking materials for subsequent plasma etching. Lin et. al. [89] used Ni and poly-silicon mask to etch Sapphire.

Surface texturing [41] using Interferometric Lithography (IL) followed by plasma etching is an established method for fabricating NALs [74, 148] for higher power applications [53] or wherever suppression of reflection is needed. Fabrication of highly organized arrays of nanostructures with considerably small dimensions is possible using this method. Silicon is one of the common materials used for nano-structured antireflection layers, designed for infrared (IR) applications. Si is transparent at a portion of near-IR and mid-IR [116] region. However in absence of NAL, its high refractive index of 3.5 [48] causes too much reflection at the silicon/air interface. Nano-structuring the surfaces of silicon is used to improve transmission at the silicon/air interface in the IR and near-IR applications. The non-polymeric antireflection structures usually provide a higher laser damage threshold. The high damage threshold of fused-silica NALs has been investigated by [114] by a $8ps$ laser with wavelength of $1030nm$ [114]. Other groups have reported fabrication of $GaAs$ nanostructured antireflection layer by etching the $GaAs$ wafer coated with a layer of silica as the mask, using a plasma etching method [121, 73].

Different fabrication methods can yield nanostructures with different profiles. Some of the common structures used as antireflection layers are nano-pillars [142] and (micron-size) pyramids created by etching [139]. Improving the profile of the nanostructures can have considerable effect on the overall performance of the NAL. Structured anti-reflection coatings can be fabricated as a part of the substrate through patterning and etching. This will produce NALs with the same material and thus thermal expansion coefficient as the substrate. Such antireflection layers are more robust

and can tolerate considerable temperature changes without delamination since no residual stresses exist. This makes them ideal for high-power laser-beam-transmission as well as space applications [93].

4.2 Theory of Antireflection Layers

Theory and fabrication of nanostructured antireflection layers has been the focus of numerous reports such as [110]. Although many numerical methods have been developed and used to study transmission of light through the wide variety of experimentally fabricated structures, there is still a need for developing models for gaining mathematical insight into how these structures function with the goal of designing the optimum profile which can lead to optimum transmission for the specific wavelength.

By definition an anti reflection layer introduces an intermediary layer which replaces the otherwise considerable change of refractive index between the two medium by two smaller steps. It can be shown that this means the refractive index of antireflection layer/coating should ideally be the geometric average of the refractive indexes of the two medium. Deviation from the required refractive index reduces the performance of the antireflection layer. In eq. (4.1) n_i and n_t are the refractive indexes of the "incident" and the "transmission" medium respectively.

$$n = \sqrt{n_i n_t} \tag{4.1}$$

In order to achieve maximum transmission, the thickness of the antireflection layer should be equal to $\frac{\lambda}{4n_{eff}}$ [43], where n_{eff} represents the effective overall refractive index of the antireflection layer. This thickness will result in a phase change of π through the thickness of the antireflection layer [43].

4.2.1 Multilayer Antireflection

Using multiple layers instead of only one, can break the sudden change in the refraction index into even smaller steps, further smoothing out the transition. This has been proven to allow broader wavelengths to pass as well as increasing the angular tolerance [113]. In a multi-layer antireflection coating, each layer's refractive index should ideally be intermediate to the layer before and after. With the refractive indexes of the incident and transition mediums known, one can use equation (4.2) to determine the required refractive index for each intermediate layer. In this equation the 0th and $(N+1)^{th}$ layers represent the "incident" and "transmission" mediums respectively.

$$n_i = \sqrt{n_{i-1}n_{i+1}} \quad \text{where} \quad i = 0, 1, 2, ..., N+1 \tag{4.2}$$

Using the natural logarithm of each term converts the nonlinear equation between refractive indexes of subsequent layers (eq. (4.2)) to the linear recursive equation (4.3).

$$\ln n_i = \frac{1}{2}\left(\ln n_{i-1} + \ln n_{i+1}\right) \quad \text{where} \quad i = 0, 1, 2, ..., N+1 \tag{4.3}$$

Defining $A_N = \ln n_N$ one can write eq. (4.3) as eq. (4.4), which can be used to determine the required refractive index for each of the layers of an N-layered antireflection coating, for maximum performance.

$$
\begin{pmatrix}
2 & -1 & 0 & \cdots & 0 & 0 \\
-1 & 2 & -1 & \cdots & 0 & 0 \\
0 & -1 & 2 & \cdots & 0 & 0 \\
\vdots & \vdots & \vdots & \ddots & \vdots & \vdots \\
0 & 0 & 0 & \cdots & 2 & -1 \\
0 & 0 & 0 & \cdots & -1 & 2
\end{pmatrix}
\begin{pmatrix}
A_1 \\
A_2 \\
\vdots \\
A_{N-1} \\
A_N
\end{pmatrix}
=
\begin{pmatrix}
A_0 \\
0 \\
\vdots \\
0 \\
A_{N+1}
\end{pmatrix}
\tag{4.4}
$$

In this matrix A_0 and A_{N+1} are the only known parameters, referring to the logarithm of refractive index of the "incident" and "transmission" mediums respectively.

Equation (4.4) can be used to determine the required refractive index for each of the intermediate layers of a multi-layered antireflection coating. As the number of layers increase, the transition of refractive index becomes smoother, however it is almost impossible to match the required refractive indexes with the available materials.

4.2.2 Nanostructures as Antireflection Layer

Nanostructured surfaces provide an alternative to regular single and multi-layered antireflection coatings. Nanostructured antireflection layers are built in as part of the substrate (previously referred to as the "transmission medium") through micro-machining and thus is made from the same material as the substrate. This eliminates residual stresses and delamination problems, common with regular antireflection coatings. Figure 4.2(a) shows the SEM image of such structure created on a silicon chip. The distance between two corresponding points adjacent structures determines the period and pitch in a specific direction. If the period of the structures and thus their sizes are considerably smaller than the wavelength of light, the optical wave interacts with the nanostructure as if it's a continuous layer with an effective refractive index less than silicon and more than air. As a result, light will pass through the nano-structured layer without diffraction [127].

The NALs can be studied as 2-D arrays of semi-cone-shaped structures illustrated in Fig. 4.2(b). For ease of explanation and understanding, the NAL of this figure is illustrated as isolated nanostructures but they can merge at their base as well. Each unit cell is composed of a nanostructure and the air surrounding it. The pitch in each direction is the distance from a point in one unit cell to the corresponding point
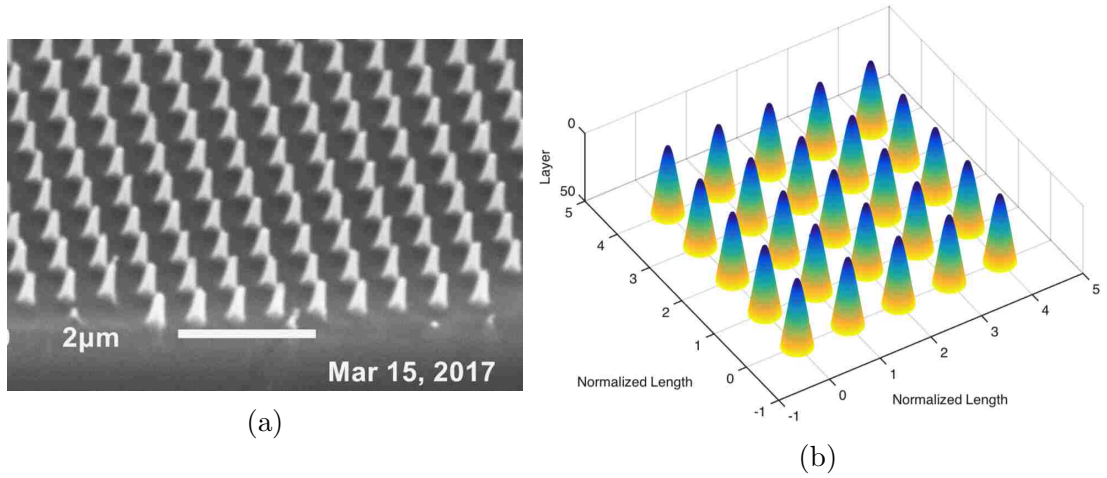
Figure 4.2: NALs for improving transmission (a) A micro-graph of silicon NALs carved out of a silicon wafer (b) Eliminating the substrate, a NAL can be studied as a 2-D array of semi-cone-shaped nanostructures.

in the adjacent unit cell. One can also consider the NAL of Fig. 4.2(b) as thousands of infinitesimally thin cross-sections, on top of each other. Each horizontal cross-section of Fig. 4.2(b) will have periodic regions of silicon and air. The percentage of the each cross-section occupied by silicon is referred to as the "Fill-Factor", at that elevation and has a deterministic factor on its optical properties. Using eq.(4.5) one can calculate the refractive index at each cross-section as function of the fill factor and the refractive indexes of the materials composing it, i.e. air and silicon in here. This means a nanostructured antireflection layer can be modeled as numerous homogeneous antireflection coatings stacked on top of each other, with each layer's refractive index being equal to the effective refractive index at that elevation. Thus by controlling the fill factor one can effectively engineer the refractive index to any desired value overcoming the difficulty faced in homogeneous antireflection coatings.

$$n_{(z)} = p_{(z)}\, n_{Si} + \left(p_{(z)} - 1\right) n_{Air} \tag{4.5}$$

In eq. (4.5), $n_{(z)}$ and $p_{(z)}$ are the effective refractive index and the fill-factor at height z, measured from the surface of the silicon wafer. A gradual change in the

fill-factor (from 0% at the top to 100% at the bottom) results in refractive index gradually changing from that of the air on top to that of silicon at the bottom [56, 110]. Although eq. (4.5) is used for special case of silicon nanostructures surrounded by air in here, it can be used for other materials as well.

4.3 Optimum Profile Design

In this section the optimal profile for the periodic nanostructures is calculated. In order to achieve optimum transmission, the profile of the nanostructures should be designed such that the refractive index at each cross-section follows the geometric average rule of eq. (4.2). The height of each cross-section and subsequently the total height of the nanostructures is an other important parameter that should be determined. The design process thus can be divided into two main steps, i.e. determination of the fill-factor and the thickness of each cross-section of the nanostructures.

4.3.1 Determination of the Fill-Factor

Each cross-section of a specific NAL can be considered a thin antireflection layer. Simultaneous solution of eqs. (4.4) and (4.5) determines the refractive index of every cross-section layer, required to achieve optimum transmission between adjacent layers. This calculation can be done for any desired number of cross-sections. Increasing the number of cross-sections result in finer increments in refractive index between layers and thus better transmission. Although theoretically one can divide the NAL to any number of horizontal segments, it was observed that no significant improvement is achieved by increasing the number of cross-sections by more than 100. Thus all the calculations performed here are reported for 100 horizontal cross-sections.

Figures 4.3(a)& 4.3(b) show the calculated refractive index and the fill-factors

required for each of the 100 cross-section layers comprising a silicon LAN. The cross-section layers are numbered from 1 to 100, starting at the top. Fig. 4.3(a) shows that as expected, the refractive index continuously increases from $n = 1$ (the refractive index of air) to $n = 3.5$ (the refractive index of silicon) as we go from layer 1 to 100. Fig. 4.3(b) shows that the fill-factors required at each cross-section increase continuously from $p = 0$ to $p = 1$ (or 100%) at the bottom. In other words, layer 1 is completely composed of air. The percentage of the area composed of silicon, at each cross-section, increases continuously over the NAL's height. The last layer is completely composed of silicon. This means the nanostructures should start from a point at the top and merge together at the base.

(a)   (b)
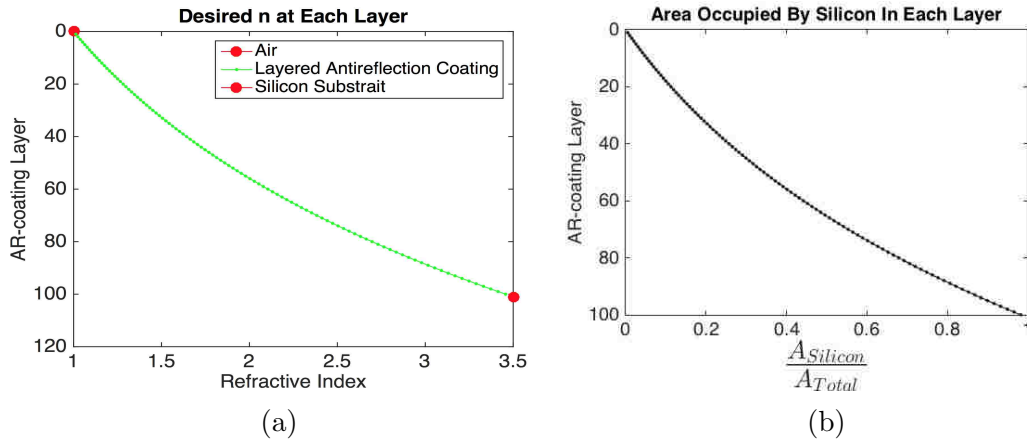
Figure 4.3: The calculated refractive index of each cross section of the NAL (a) The refractive indexes increase gradually from Layer 1 to Layer 100. $n_{Air} = 1$ and $n_{Si} = 3.5$. (b) The Si Fill-Factor changes gradually from 0% at Layer 1, on the top, to 100% at Layer 100, in the bottom.

It worth mentioning that interferometric lithography, used to fabricated NALs in here, results in 2-D Cartesian arrays of nanostructures and thus a 100% fill-factor at the base is best achievable by nanostructures with rectangular cross-sections However as the dimensions approach $100's$ of nanometers and smaller, circular cross-sections are more feasible experimentally. A circular base can either be enclosed in the square boundaries of the unit cell or enclose it. 100% fill factor using a circular cross-section,

is only possible in the later case.

Having determined the percentage of the unit cell area occupied by silicon at every cross-sectional layer of the silicon nanostructures, the width (for nanostructures with square cross-section) or radius (for nanostructures with circular cross-section) of the nanostructures can then be easily calculated at each layer. Also the fact that fill factor is a percentage rather than an absolute value provides considerable flexibility when it comes to physically fabricating the designed NALs. The actual dimensions are determined by multiplication of the fill factor by the selected pitches in x&y directions.

4.3.2   Cross-section Thicknesses and Profile Design

Although a taller [110] nanostructure helps achieving smoother transition, it is not necessarily the best approach. Not only taller nanostructures are more difficult, time consuming and expensive to fabricate, they are considerably more vulnerable to mechanical damages. It's crucial to maximize transmission while limiting the nanostructured height.

Simulation results (please refer to Sec.4.4.3 for more info) have shown that the performance of a nanostructured antireflection coating increases as its overall thickness (in other words the height of nanostructures) increases but the trend saturates at a thickness which corresponds to a phase change of π in the light as it travels inside the nanostructure. Further increase of the NAL thickness or thus the height of nanostructures doesn't result in any noticeable improvement in transmission. Thus the minimum height of nanostructures which can still result in optimum transmission, is the one which results in a phase difference of π in the light.

Eq. (4.6) describes the total phase-change in the light as it travels through the

NAL as the summation of the phase-changes in each cross-sectional layer.

$$\sum_{i=1}^{N} k_i t_i = \pi \tag{4.6}$$

In this equation t_i and k_i are the thickness and the wave vector at each of the N layers, correspondingly. The wave vectors can be expressed as $k_i = \frac{2\pi n_i}{\lambda}$, where λ is the wave length of the light at air (incidence medium). n_i is the effective refractive index of each layer calculated in equation 4.5.

$$\sum_{i=1}^{N} n_i t_i = \frac{\lambda}{2} \tag{4.7}$$

Using the method of [110] and eq.(4.7), the thickness of each layer can be calculated as in eq. (4.8). Figure 4.4 shows the calculated thickness required at each cross-section layer.
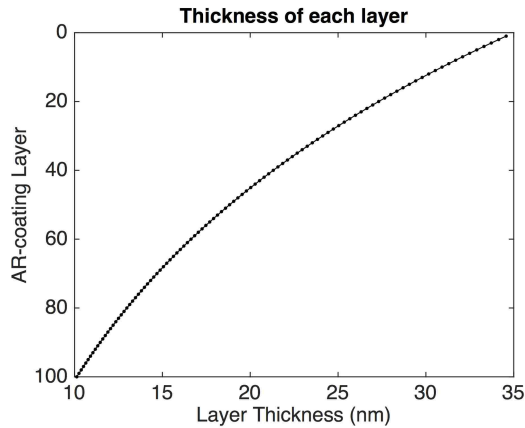
$$t_i = \frac{\lambda}{2N n_i} \tag{4.8}$$

Figure 4.4: The required thickness of each of the 100 cross-sectional layers of a NAL that will maximize transmission of of a $4\mu m$ light from air into silicon substrate.

Having determined the fill-factor and thickness at each of the cross-sections of a NAL, one can plot the ideal profile for a nanostructure as shown in Fig. 4.5. The
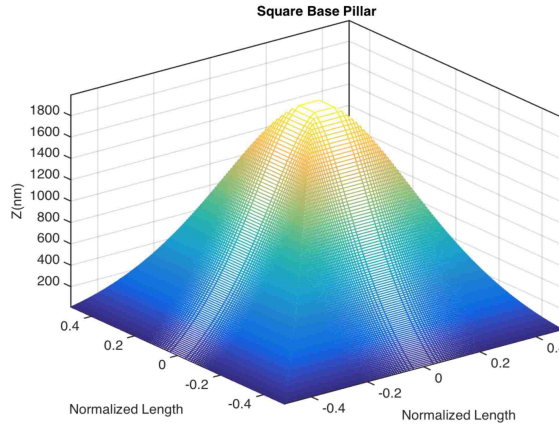
Figure 4.5: Nano-pillars with square cross section

input parameters in the design each profile are the refractive indexes of the incident and transmission medium and the wavelength of the light. Choosing the incident transmission media as air and silicon, the optimum profile can be designed for each wavelength.

It should be noted that the x & y axis in Fig. 4.5 are in units of "normalized-length" (which can also be interpreted as the 1-D fill-factor). This method of expressing the results offers considerable flexibility. By multiplication of the results obtained in normalized-length, with the pitch (controlled by interferometric lithography setup), one can readily obtain the shape of the optimal profile of the nanostructure in units of nm for the specific wave-length and pitch.

An other important consideration about the calculated profile of Fig. 4.5 is that the designed nanostructure starts as a point at the top (with a fill factor of 0%) and gradually widens to occupy the unit cell completely at the base. Thus each of the designed nanostructures merge with their immediate neighbors as well as with the silicon substrate. As the light travels through the depth of a nanostructured antireflection coating designed using this method, the effective refractive index changes gradually from that of air to that of silicon maximizing transmission. The simulation

results of the next section will study the performance of these nanostructures using numerical methods.
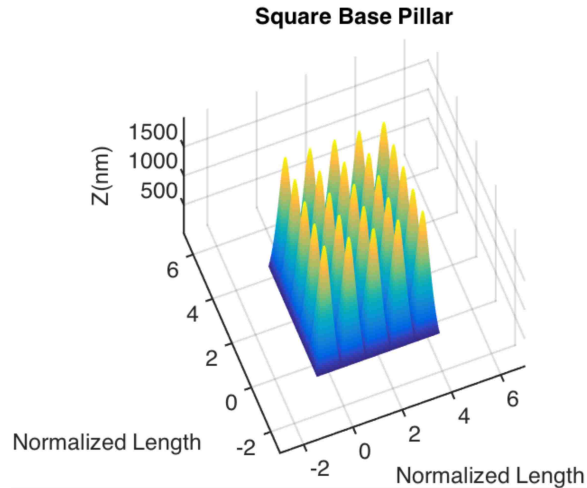
Figure 4.6: A NAL composed of a 2D array of nanostructures. For avoiding diffraction, it is essential to keep the pitch of nanostructures well below the wavelength of light.

Fig. 4.6 illustrates a NAL made of an array of the designed nanostructures. In order to prevent any diffraction from the nanostructures it is essential to keep the pitch of the nanostructures well below the wavelength of light.

4.4 RCWA Simulation Results

Extensive numerical studies have been reported on the performance of NALs of different shapes and materials. These reports use different methods including Effective Medium Theory (EMT), Finite Difference Time Domain (FDTD), Transfer Matrix Method (TMM), Finite Element Method [50] and Rigorous Coupled Wave Analysis (RCWA). Using these methods, researches have simulated the behavior of different designs such as cylindrical, cone shaped, parabolic and moth-eye structures [118]. The main method used here to simulate the performance of the proposed profile

is RCWA although some FEM has been used as well. RCWA method solves the electromagnetic field equations (4.9) and (4.10) to study the scattering of electromagnetic waves in particular by periodic structures. Here RCWA will be used to study the scattering as a function of the geometry and shape of individual elements of the periodic structure.

$$\nabla \times \mu_r^{-1}(\nabla \times E) = k_0^2(\epsilon_r - \frac{j_0 \sigma}{\omega \epsilon_0}).E \tag{4.9}$$

$$E(x, y, z) = E(x, y).e^{-ikz} \tag{4.10}$$

Equations (4.9) and (4.10) relate the geometry of nanostructures to the electric field (and the coupled magnetic field intensity H) and to the transmission of different wavelengths. This dependence is more considerable at smaller wavelengths (compared with the pitch and dimensions of the nanostructures) but decreases as the wavelength increases. The simulations performed here, cover a wide range of wavelengths and pitch values as well as substrates materials other than silicon.

4.4.1 Transmission Through NAL with Optimized Profile

In this section transmission of mid-IR (MIR) light through nanostructured antireflection layer (NAL) is studied. All NALs used in these numerical analysis have the same optimized height & fill-factor profile but different pitch values. The height and fill factors used in this section are optimized for wavelengths between $4\mu m$ and $9\mu m$. Figure 4.7(a) shows the RCWA simulation results for transmission of MIR light ($3\mu m < \lambda < 9\mu m$) through NALs as a function of the wavelength (λ) and the nanopillar pitch. The profiles of the nanopillars used in this simulation are designed to be optimal at every specific λ. These results show that, the transmission drops considerably at large pitch values due to the diffraction from nanostructures. At very small pitch values on the other hand, transmission drops very slowly. This is due to over simplification of the interaction by the effective refractive index concept

(that is an approximation and doesn't distinguish between profiles as opposed to exact solution to Maxwell equations). The peak values of transmission (represented as a bright yellow region in figure 4.7(a)), seem to fall along a transverse line in the λ-pitch plane. Fig. 4.7(b) shows this behavior much better by capturing the top view of the transmission data. This figure reveals that transmission is maximum along the $pitch = 0.28\lambda$. Table 4.1 reports the values of transmission on a couple of points along this imaginary line, confirming this observation.
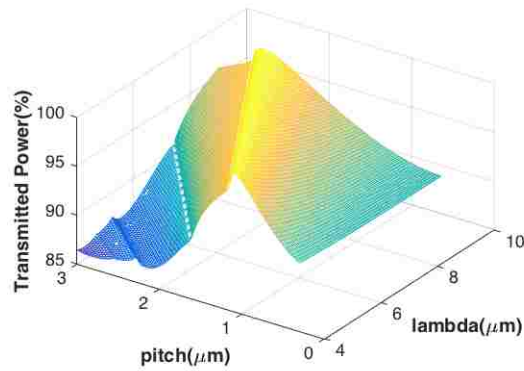
(a)
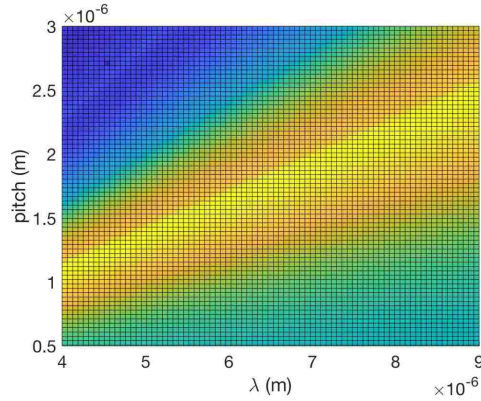
(b)

Figure 4.7: Transmission of IR light ($4\mu m < \lambda < 9\mu m$) through NALs (a) 3-D representation of transmission results. (b) Top-view representation of transmission results of part (a). The yellow line represents the maximum values corresponding to transmission for $pitch = 0.28\lambda$ (the transmission reduces away from the yellow region)

As the pitch to wavelength ratio becomes larger, scattering to high spatial frequencies increases and therefore the scattering free transmission efficiency (zeroth order transmission) is reduced. To better understand this phenomenon we again refer to figure 4.7. The maximum transmission happens along the yellow line. The data in table 4.1 is also alongside this yellow line. On the right hand side of this yellow line (larger wavelengths region at a fixed pitch), according to the simulations, all the energy is transmitted through the zeroth order (scattering free transmission). On the left hand side of the yellow line (lower wavelengths at the fixed pitch) we always see scattering to higher spatial frequencies, which drastically decrease the zeroth order transmission. By cutting the surface of figure 4.7 along pitch and λ axis, these variations can be observed more clearly as shown in figure 4.8.

Table 4.1: **The maximum transmission values at different wavelengths for optimal shape and pitch (air-silicon interface)**

Index of refraction	$\lambda(\mu m)$	Pitch(μm)	Optimum Transmission
$n = 3.5$	4	1.11	0.9906
$n = 3.5$	7	1.91	0.9911
$n = 3.5$	10	2.7	0.9910

In addition to the profile of nanostructure, the transmission is affected by the angle of incident beam and pitch of the NAL. According to [22, 103], the angle of of scattered light is related to the angle of incident light and pitch through:

$$k^2 n_2^2 sin^2(\theta_{mn}) = \left(kn_1 sin(\theta)cos(\phi) + \frac{2\pi m}{d_x} \right)^2 + \left(kn_1 sin(\theta)sin(\phi) + \frac{2\pi n}{d_y} \right)^2 \quad (4.11)$$

where d_x and d_y represent the pitch values in the X and Y directions respectively (corresponding to the NAL on top of the substrate). θ and ϕ are the polar and azimuthal angles for the incident beam (incident k-vector).θ_{mn} specifies the propagation direction of the transmitted (diffracted) wave (m and n are integers defining the diffraction order related to the periodicity along x and y directions respectively).
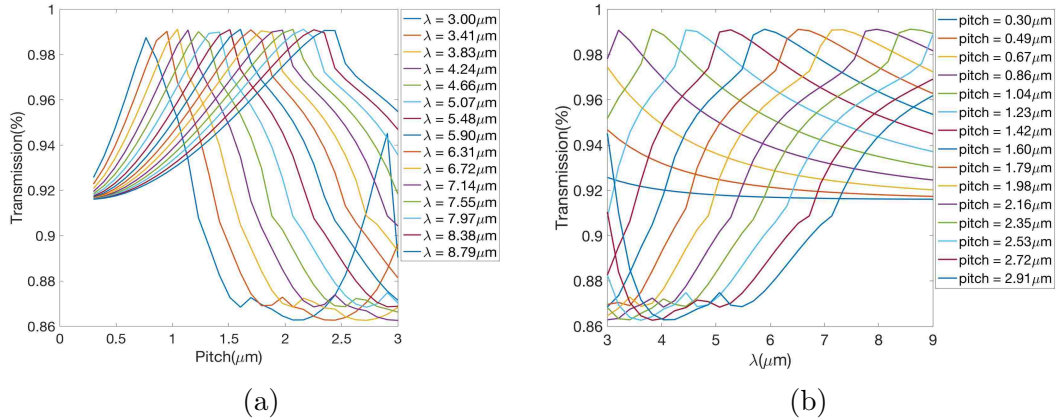
Figure 4.8: 2D cut planes from the 3D transmission data in Figure 4.7(a). (a) Transmission versus pitch at different wavelengths. (b) Transmission versus wavelength at different pitches.

n_1 is the refractive index of the incidence medium (usually air), and n_2 is the refractive index of the substrate. If the pitch is small enough, the equation has solutions for larger values of m and n. When the angle of incidence is zero there is a simple relation for the pitch $Pitch$ to refrain diffraction is:

$$Pitch = \frac{\lambda_{inc}}{n_2} \qquad (4.12)$$

where n_2 is the refractive index of the substrate.

In our theoretical estimation of transmission we have assumed the angle of incidence to be zero. Also the features of the periodic nano-texture are considered small compared to wavelength, so the transmission will mainly occur at zeroth order.

4.4.2 Transmission Through NALs With Parabolic Profile

An alternative profile previously reported for NALs is the parabolic profile. Figure 4.9(a) shows the RCWA simulation results for NALs with parabolic profile. Parabolic profile is not the ideal profile and the corresponding peak transmission

values are less than that of the optimal profile presented in the previous sections as evident from figure 4.8 however the differences are in the range of less than couple of percents. Note that when using high power lasers, even the smallest improvements can have significant impact on system performance. It should also be mentioned that parabolic designs, based on RCWA simulation results, improve the transmission over a broader wavelength range.
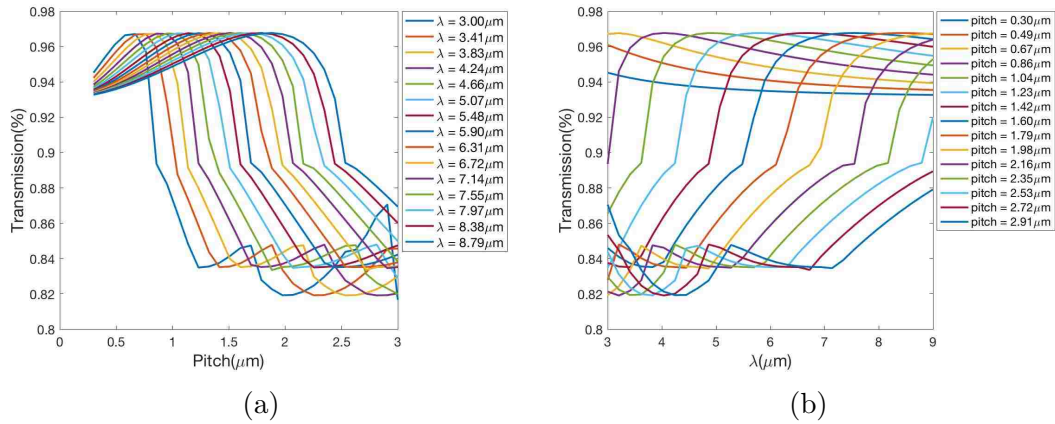
Figure 4.9: Transmission through NAL with parabolic profile.(a) Transmission through NAL plotted versus pitch at different wavelengths. (b) Transmission through NAL plotted versus wavelength at different pitch values.

Table 4.2: **Maximum transmission at optimal pitch values (for parabolic profile) through substrates with different refractive indexes.**

Index of refraction	$\lambda(\mu m)$	Pitch(μm)	Transmission
$n = 1.5$	4	0.8	0.9997
$n = 1.5$	7	1.5	0.9997
$n = 1.5$	10	2.1	0.9993
$n = 2.5$	4	0.8	0.9873
$n = 2.5$	7	1.5	0.9882
$n = 2.5$	10	2	0.9873
$n = 3.5$	4	0.8	0.9632
$n = 3.5$	7	1.5	0.9698
$n = 3.5$	10	2	0.9633

Although the main focus of this study is transmission through a silicon substrate, Table 4.2 also shows a the transmission data for three different substrate materials with different refractive index values at multiple λ and pith values. The simulation results of this table confirm that for the same λ and p values, the transmission is smaller for larger substrate-refractive-indexes. In general it is well understood that as the index contrast between the background and substrate medium increases the transmission decreases making the use of antireflection coating more crucial.

4.4.3   Increasing Height to Wavelength Ratio

The nanostructures studied so far, had a height of $\frac{\lambda}{2n_{eff}}$ which would result in a phase-lag of π in the light as it travels through the nanostructure. For simplicity we will refer to this height as h_π. This value is different for different profiles. The h_π is actually half of the value commonly used in other reports. However our simulation results indicate that increasing the nanostructure-heights further than h_π won't result in any significant increase in transmission at a specific wavelength. This section is devoted to study the effects of NAL thickness (nanostructure-heights) in transmission of IR-light.

The results of Fig. 4.10(a) & Fig. 4.10(b) show how transmission changes as a function of nanostructure height. Each of the nanostructures of Fig. 4.10(a) is designed for a different λ and pitch values. The selected pitch and λ values fall on the $\lambda = 3.7 * Pitch$ line of Fig. 4.7(b). This guarantees that the profile used will yield maximum transmission and the observed effects are only due to the change in nanostructure height. As can be seen the transmission increases as the nanostructure-height increases. The transmissions reach almost 100% as the height reaches h_π. As shown in Fig. 4.10(b), all curves of Fig. 4.10(a) overlap when the nanostructure-heights are normalized with respect to to their corresponding h_π. Thus Fig. 4.10(b)
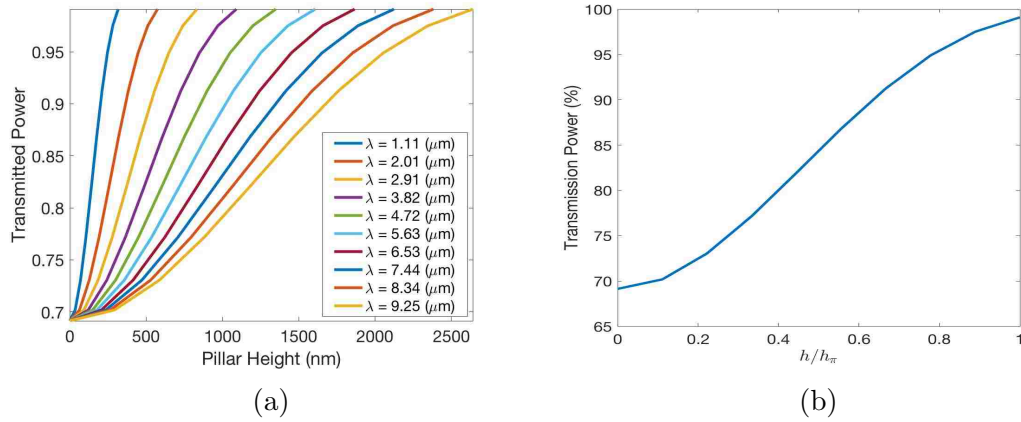
Figure 4.10: The transmission versus pillar height for different wavelengths. The total phase shift is π where T = 99.1% (a) Transmission versus NAL height. $\lambda = 3.7 * Pitch$ as discussed in Fig. 4.7(b). (b) All transmission curves overlap when the nanostructure-heights are normalized with respect to the h_π for each design.

can be used to study the effect of nanostructure-height on transmission through NAL for all the wavelengths of interest.
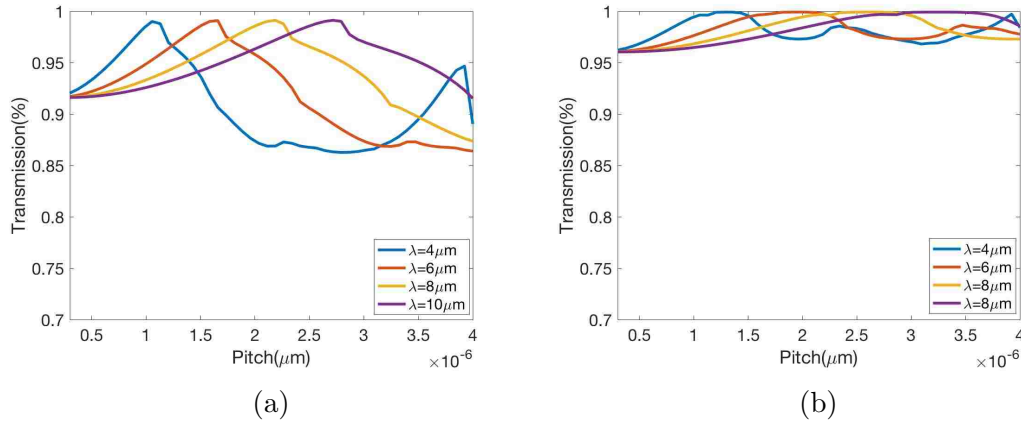
Figure 4.11: Comparison of the transmission bandwidth between two sets of nanostructures with heights of (a) h_π and (b) $2h_\pi$.

The results obtained here indicate that NALs with a thickness of h_π provide maximum transmission while keeping the nanostructure heights at minimum. Further

increase of nanostructure-heights can increase the transmission over a larger band-width. Fig 4.11 shows the simulated transmission of nanostructures with heights of h_π and $2h_\pi$. Thus depending on the application one might find either h_π or $2h_\pi$ as the ideal nanostructure height.
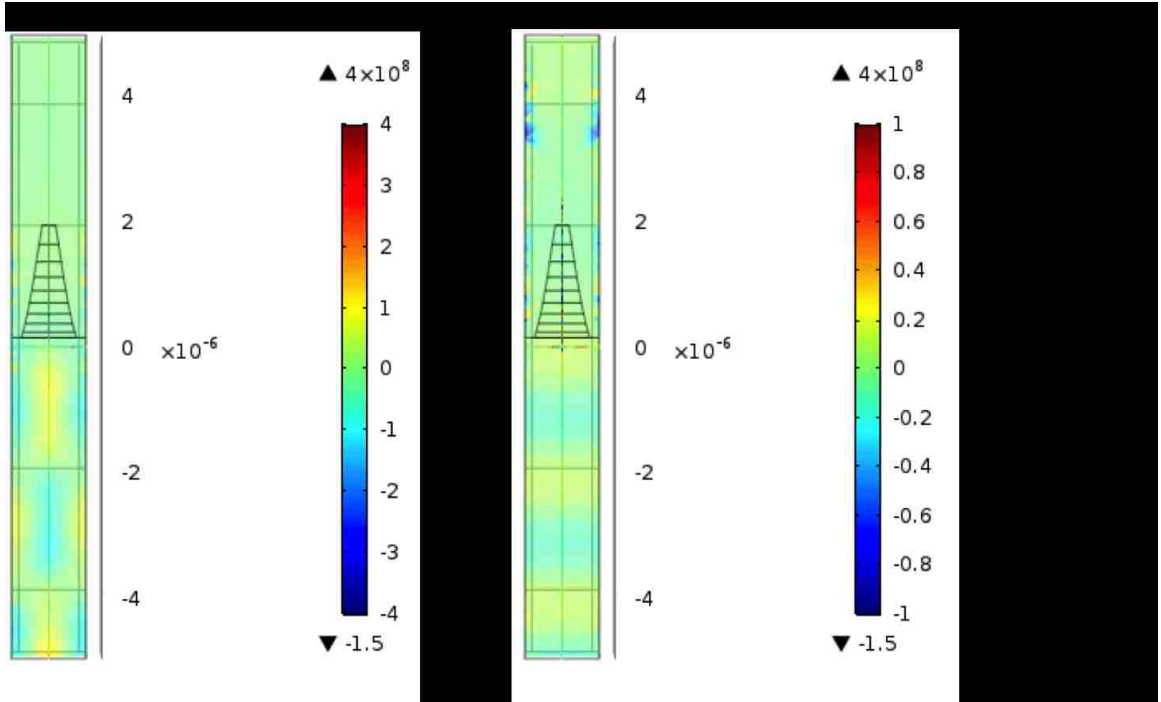
Figure 4.12: Both identical pillars height designed for $7\mu m$ wavelength. (a) Transmitting wavefront when incident beam is a $4\mu m$ light (the height is equivalent for a roughly 2π phase shift for this wavelength) (b) The illumination is at $7\mu m$ equivalent to π phase shift of the light

In a recent work, Wang et al. [132] showed that when the ratio of height to wavelength of nanostructures increase, the wavefront is distorted as it passes through the NAL. The finite element simulation results of Fig. 4.12 show a comparison between the transmitted wavefronts for nanostructures with heights of h_π and $2h_\pi$. These results are in good agreement with the results of [132] revealing that as ratio of height to wavelength is increased the wave is diffracted into higher spatial frequencies.

Over all the results of this section indicate that h_π is the optimal height for the nanostructures and in order to obtain maximum transmission at a target wavelength, the pitch should be set as using the $\lambda = 3.7 * Pitch$ relationship according to figure 4.7(b) and 4.8.

4.5 Experimental Results for IR Transmission Through Silicon and Effects of NAL

As explained in Chapter 3, an FTIR microscope is used for measuring IR transmission through the samples with NALs. The specific microscope used, can run measurements in both "Reflection" and "Transmission" Modes. Fig 4.13 shows the comparison of these two modes for IR transmission through a microscope slide as well as two-side-polished silicon wafer. Silicon is inherently transparent through a portion of the infra-red (IR) regime.
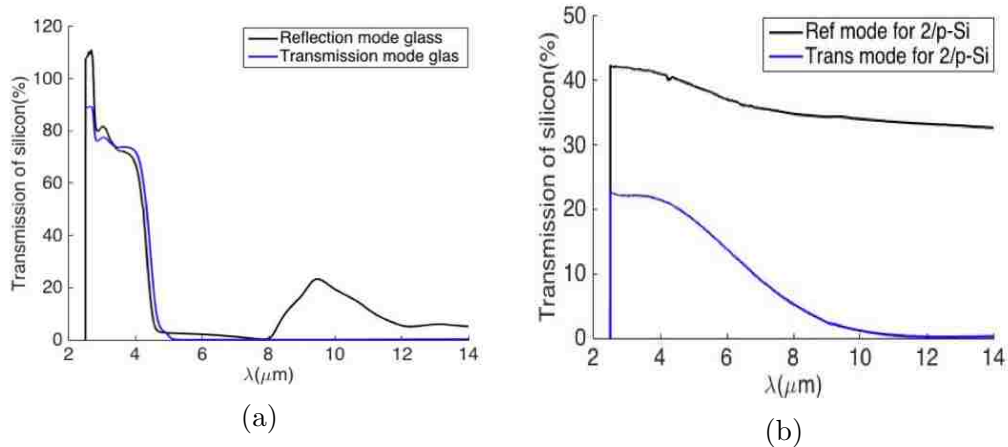
Figure 4.13: Transmission of materials with known IR transmission profile have been measured for calibration. (a) Transmission through a microscope slide (b) Transmission through a double-side-polished silicon wafer, using two different reflection and transmission modes.
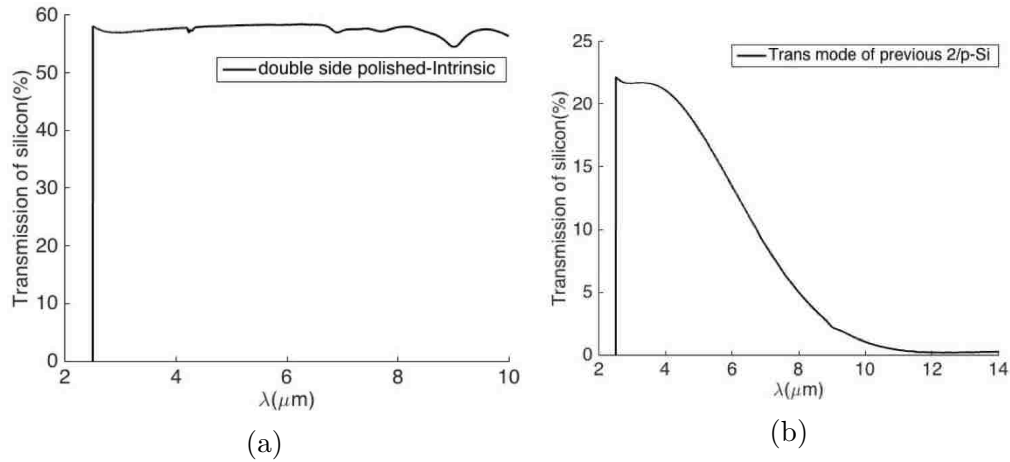
Figure 4.14: Transmission of IR through two (100) double side polished silicon wafers, (a) Intrinsic (b) Highly doped.

The transparency bandwidth can change significantly based on the manufacturing method of the wafer and impurities present. Figure 4.14 compares the transmission bandwidth of an intrinsic silicon wafer with a highly doped one. The transmission is shown for two intrinsic silicon wafer with different manufacturing technology of silicon wafer in figure 4.15. Overall if high transmission is needed, one should choose intrinsic silicon. [126].
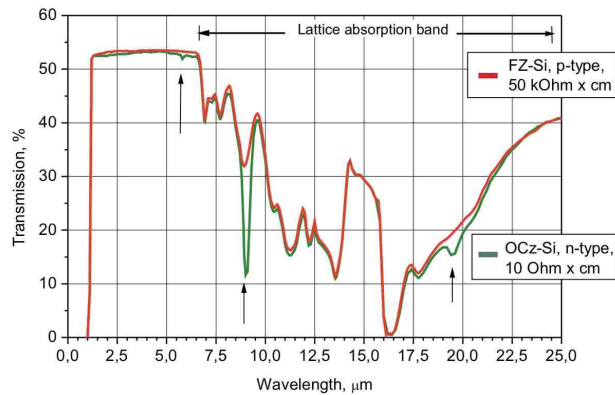
Figure 4.15: Effects of positive and negative doping on transmission bandwidth[126].

As shown in figure 4.15 and according to [126], the optical grade Czochralski

silicon crystal can be used in a wave length region of $1\mu m$ to $6\mu m$ while the float zone silicon crystal can perform from $1\mu m$ to $14\mu m$. All the nanostructured antireflection layers whose experimentally-measured transmission data are reported here, are fabricated using identical intrinsic silicon wafers.

A total of four samples will be presented and discussed here. In the first (Fig. 4.16) and last (Fig. 4.19) samples the nanostructures are fabricated only on one side of the wafer while samples 2 and 3 (Figs. 4.17 & 4.18) have nanostructures on both sides.

(a)   (b)
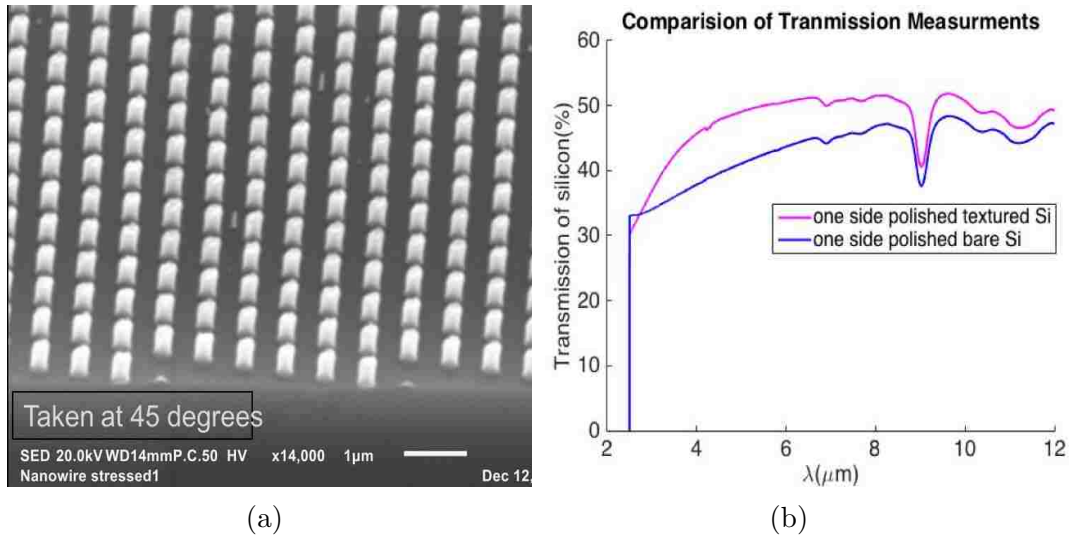
Figure 4.16: Vertical profile. 40% duty cycle corresponds to 16% of unit cell. No significant change of transmission is observed (a) One-sided-polished intrinsic Si wafer with a NAL fabricated on the polished side. The nanostructures demonstrate relatively large pitch values, low duty cycle and straight side-walls. (b) Transmission of the fabricated NAL is compared to the intrinsic one-side-polished silicon wafer.

In the sample of figure 4.16(a) the nanostructures are relatively spars, covering a considerably small portion of the unit-cell also they have vertical sidewalls. Vertical sidewalls means the fill factor remains relatively constant with a refractive index intermediary to that of air and silicon. Also the relatively small fill-factor means the effective refractive index is numerically closer to that of air. These factors are expected to significantly reduce the performance of this NAL as confirmed by the

experimental data of Fig. 4.16(b). This transmission plot obtained is not significantly difference from a bare Silicon wafer. This emphasizes the importance of the nanostructures profile, and fill-factor, in their performance.

(a) (b)
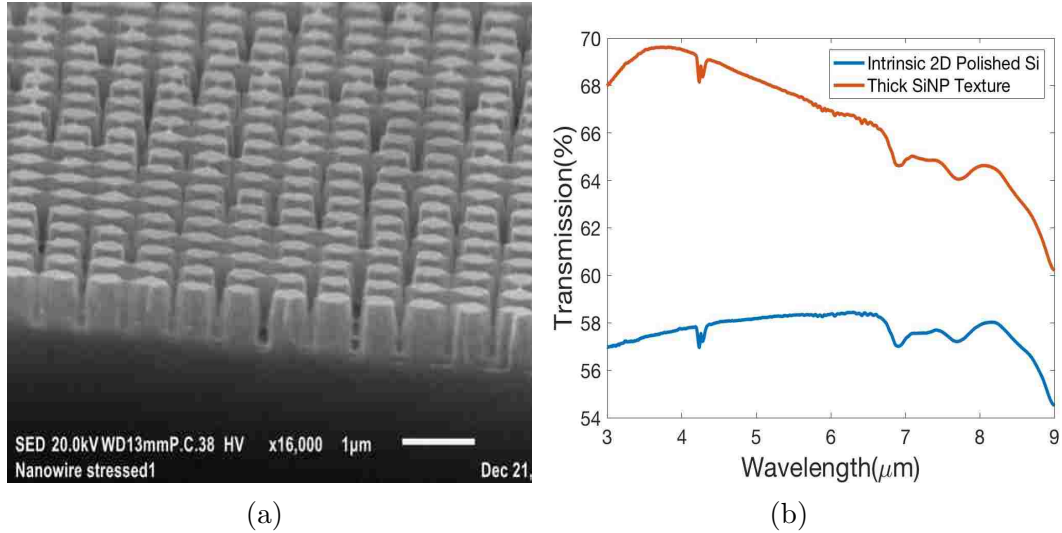
Figure 4.17: 84% duty cycle means 70% of the cross section area is covered by vertical NAL. We should consider the sqrt of the transmission measured to get T for one layer (which reaches 83%) (a) SiNPs (b) Transmission of bare and double-side-nanostructured intrinsic silicon

Samples number 2 and 3 were fabricated with the goal of achieving 100% fill-factor at the base. As can be seen in Figures 4.17(a) and 4.18(a), the fabricated nanostructures represent much higher fill-factors than that of Figure 4.16. In figure 4.18(a) the fill factors reduce from $\approx 100\%$ fill-factor at the base to a smaller value at the tips, through optimizing the etching process, yielding a higher transmission compared to figure 4.17.

The experimental transmission data of Figs.4.17(b) & 4.18(b) might not look very impressive at a first glance since it is not even close to the simulation results. However it should be noted that these experimental data are for double-sided samples. As long as the reflections are little (around 10%), if the transmission through one interface

(a)   (b)
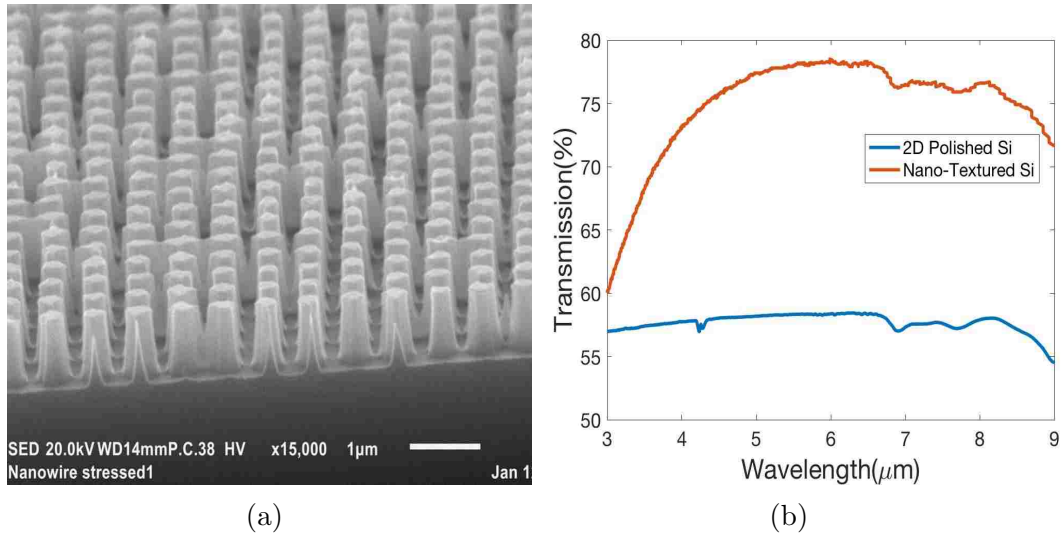
Figure 4.18: Transmission from double side taper NAL(a) High duty cycle thick nanostructures with near 75% fill factor at the base and tapered sidewalls. (b) Transmission of (2 side polished) bare and double-side nanostructured intrinsic silicon

is denoted by $T\%$ the transmission from a two sided sample will be T^2. This means in order to obtain transmission data corresponding to a single interface one should calculate the square root of the transmission data obtained from a double sided sample (See Fig. 4.20(b)). Comparison of the square root of the transmission data in Figures 4.17(b) and 4.18(b) with the transmission percentage of Fig. 4.16(b) would then reveal the considerable improvement achieved by samples 2 and 3.

Figure 4.19(a) shows the fourth sample which presents a profile very close to the optimal profile designed in section4.3. These nanostructure are fabricated on the polished side of an intrinsic silicon wafer using inductive couple plasma (ICO). Currently we are waiting the ICP to fabricate identical structures on both sides of the wafer since the available RIE can't perform homogeneous etching required to fabricate these profiles.

Finally, a comparison is done between the experimentally measured transmis-

(a)

(b)
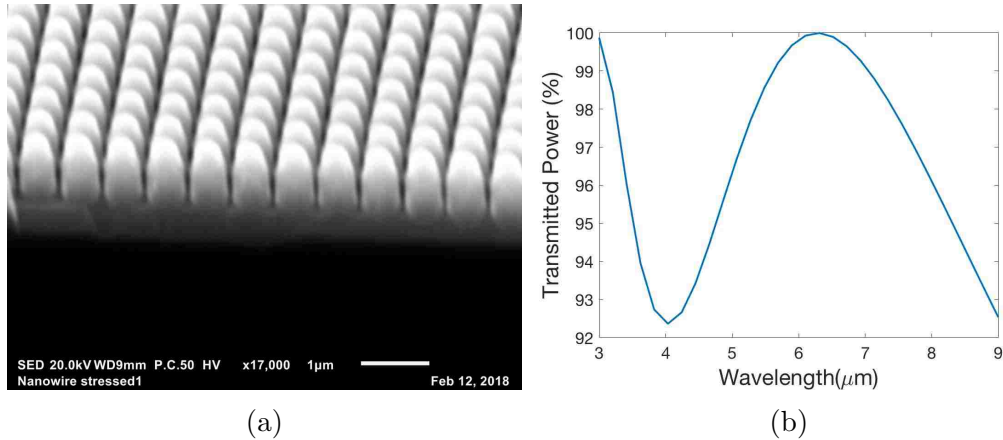
Figure 4.19: Tapered profile fabricated by ICP and CF_4.(a) SEM image of the NAL. (b) The transmission calculated by RCWA (the measured transmission is not available).

(a)

(b)
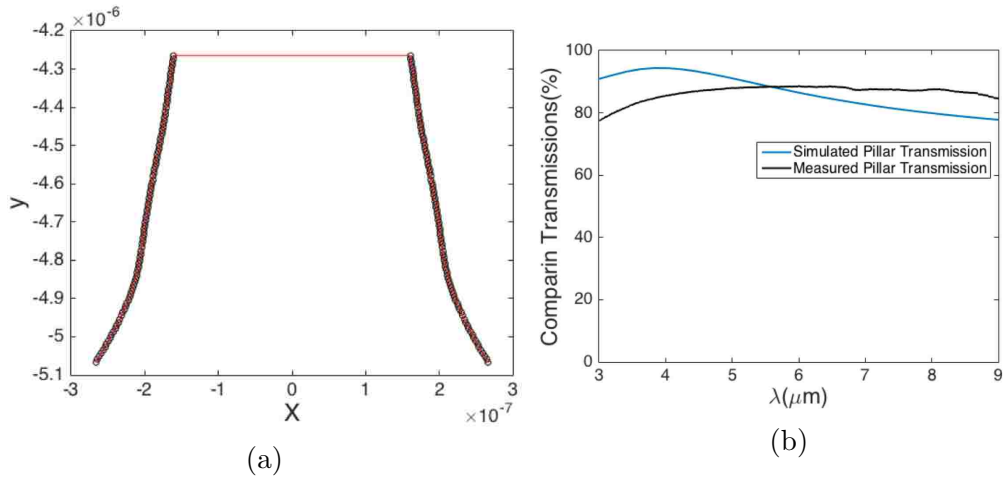
Figure 4.20: Simulation of structures transmission by RCWA (a) Average profile of the nanostructures of Fig 4.18(a) is obtained and used to perform numerical simulations using RCWA. (b) Comparison of RCWA and experimental results for transmission percentage through NALS into the underlaying bulk silicon

sion data and simulation results for one of the fabricated samples. The sample of Fig.4.18(a) is used for this purpose. The average profile of the fabricated nanostructures are obtained from the micro-graphs and reconstructed in MATLAB (see Fig. 4.20(a)). RCWA method is used to determine transmission through the obtained

profile. The experimental and simulation results for this specific sample are compared in Fig. 4.20(b). The one-interface transmission data are obtained by square root of the two-sided experimental data of 4.18(b) and then compared by simulation results. Fig. 4.20(b) show considerable agreement between experimental and simulation results as well as some small differences that can be due to the simplifications inherent to the RCWA method.

4.6 Conclusion

Nanostructured antireflection layers were studied in this chapter and found to offer significant advantages over traditional multilayer deposited antireflection coatings. NALs etched out of a substrate, have the same material as the substrate minimizing any thermal stresses. NALs are designed to optimize transmission of infrared light ($3\mu m$-$7\mu m$) from air to silicon substrate. As long as the pitch and dimensions of the nanostructures are kept small compared to the wavelength of the light, the refractive index can be engineered in NALs through changing the "Fill-factor". This allowed continuous transition of refractive index from air to the silicon substrate resulting in considerably high transmission. Using the analytical method derived in this chapter, the optimal fill-factor profile of the NALs were designed and was analyzed using RCWA method. The effect of different geometrical parameters on the performance of the designed NALs were studied numerically. It was determined that besides the fill-factor profile, the pitch of the nanostructures have significant effect on their performance. According to our results, in order to maximize transmission for a specific wavelength one should select $pitch = 0.275\lambda$. Our studies show that after the fill-factor profile, height of the nanostructures is the most deterministic factor in the overall transmission. The transmission increases considerably with increasing nanostructure heights but it saturates at a height which corresponds to a π phase

shift of the light transmitting through the pillars. The bandwidth of the transmission (versus different incident wavelengths) grows broader as we increase the height, but increasing the height over the π shift, will introduce diffraction and the k vector of the transmitted light will no more be orthogonal as the k vector of the orthogonal incident plain wave. NALs with different profiles and pitch values were fabricated and tested experimentally. The experimental results were found supporting the theoretical and analytical results.

Chapter 5

Raman

5.1 Introduction

5.1.1 Objective : Characterization, and Application of Plasmonic Resonators on Silicon Nanopillars (SiNPs)

The main objectives of this study are understanding the electromagnetic behavior of gold nanodisk and gold nanodisk stacks (with silica nanodisks in between) on a silicon nanopillar (SiNP) and the application of the corresponding field enhancement (through plasmonic resonance) in Raman spectroscopy. This study consist of four parts; 1) Theoretical analysis of resonant modes and the absorption/scattering cross-sections of SiNPs and comparison with experimental results. 2) Theoretical analysis of resonant modes and the absorption/scattering cross-sections of gold nanodisk and gold nanodisk stacks. 3) Theoretical analysis of resonant modes and absorption/scattering cross-sections of gold nanodisk and god nanodisk stacks on top of SiNPs including local field enhancement in these structures. 4) Experimental study of Raman scattering by selected molecules in the vicinity of silicon pillars with gold

nanodisks (or gold nanodisk stacks) on top.5) Experimental study of Raman scattering by selected molecules in the vicinity of silicon pillars with non-gold metallic and semi-metallic nanodisks.

This chapter starts with a review of the main concepts. Next I calculate the resonant frequency and distribution of electromagnetic modes in SiNPs using finite element modeling. The scattering and absorption cross sections for SiNPs are calculated using finite Difference Time Domain (FDTD) method and then compared with experimental measurements. The plasmonic modes of gold nanodisk are calculated using analytical method, and also a simple RLC model is developed for this resonating system. The scattering/absorption cross-sections for gold nanodisks and gold nanodisks stacks are calculated using FDTD in the presence and absence of silicon substrate.

Next the behavior of the gold nanodisk (single and stack) on top of SiNP is studied by calculating the absorption/scattering cross-sections of the structure using FDTD method. Based on the outcomes of similar calculations for isolated SiNP and gold nanodisks, the interaction between plasmonic and dielectric modes are investigated. After identifying the resonance frequency of these structure, the location and magnitude of field enhancement is evaluated using FDTD simulation with excitation wavelength matched to the resonance frequencies extracted from the absorption/scattering spectrum.

In the experimental section,the plasmonic local field enhancement by gold nanodisks and nanodisks stacks are used to enhance the Raman scattering by methylene blue and thionine molecules. The measured Raman spectra are used to evaluate the field enhancement for each structure. In addition to enhanced Raman emission, in several cases decomposition of methylene blue has been observed.

The last section of this chapter is a preliminary study of the impact of the material

properties of the nanodisk on field enhancement. I have measured Raman scattering in the vicinity of SiNPs that instead of gold nanodisks, are covered by Ag, processed Ge, TiN, and CuO nanodisks.

5.1.2 Raman Enhancement Using Plasmon and Dielectric Resonance

While most photons scattered from molecules have the same energy as the incident ones (elastic scattering), a very small fraction can scatter inelastically. Raman-Scattering is the inelastic scattering of photons by molecules that are excited to their higher vibrational or rotational levels. The frequency (energy) of these photons that is shifted (usually to a lower frequency) relative to the incident photons, can be used to identify molecules and their internal energy structures. Since approximately only 1 in every 10 million photons are scattered through Raman process, it is essential to increase the strength of the interaction by resonant enhancement techniques. Nanostructures made from different materials, with different configurations and shapes have been used for this purpose.

Resonant enhancement can occur both in dielectric and metallic nanostructures. In metallic nanostructures the enhancement is a result of localized plasmon resonance. The local resonant field generated by optically excited electronic resonance is larger than the incoming optical field by the so called "field enhancement factor". Field enhancement at the frequency of incoming radiation increases the efficiency of the Raman process proportional to the second power of the field enhancement factor. Additionally as the molecule excites the plasmonic resonance, the field enhancement at Raman frequency increases the scattered radiation also proportional to the second power of the field enhancement factor. As such in the presence of plasmonic resonance, the overall efficiency of Raman scattering is enhanced by the fourth power of

field enhancement factor.

The presence of multiple plasmonic modes in the bandwidth of interest can be also important in achieving considerable field enhancement. The field-enhancement happens mainly at the resonance frequency through coupling of the propagating plasmon wave to the localized mode. Zhang et. al. [144] used Bessel equations to study these modes. It is important to emphasize that, although existence of different modes can be positive factor in Raman enhancement, the most important factor is the coupling of the plasmonic waves with the localized modes and the resulting field-enhancement and polarization of test molecule.

In dielectric nanostructures, the field enhancement is a result of the optical resonance formed by the dielectric boundary. However as the resonant field is not confined on the surface (where the interaction with molecules occur), the resulting enhancement (both in generation and radiation efficiency) is more complicated and has to be analyzed on a case by case bases.

In addition to field enhancement, the Raman scattering efficiency can be enhanced also by charge transfer between nanostructure and the molecules.This is a less understood mechanism and its strength strongly depend on the chemical composition of the nanostructure and the molecule. In this chapter we also report observation of this phenomenon for certain molecules.

Plasmonic structures, such as the metallic nanodisks and the metal/dielectric stacks have been extensively used for field-enhancement [120]. Silicon nanostructures have been also demonstrated to be capable of Raman generation [133, 131]. Silicon Nano-cones, deposited by CVD and with tips as sharp as $5nm$, have been reported to yield an enhancement of 1000 [27]. Some recent reports have used silicon-nano-pillars for field enhancement and Raman generation [72, 24]. While they attribute their observations to field enhancement by silicon, Wang et al.'s results [131] attribute

the relatively weak Raman signal obtained using Si and Ge nanostructures to the chemical enhancement caused by hydrogen bonds on Si and Ge.

Field enhancement sites can be increased by stacking multiple layers of plasmonic layers, separated by a thin dielectric layer. Maximum field-enhancement usually happens at the edges of the metal and in the dielectric region between metallic nanostructures[120, 140]. In the later case, the field won't be very accessible for the target molecules and thus can't play a role in SERS. Zhang et al. have investigated the different modes of metal-dielectric-metal and corresponding optical resonances [143].When using more than one plasmonic layer, separated with a thin layer of dielectric, the resonant fields of these layers can couple. As such the resonance frequency of the single plasmonic disk, can split into two resonance frequencies of a metal/dielectric/metal stack (usually an even mode [30, 47]). It is possible to reduce the wavelength of the odd modes and "blue-shift" them from far-infrared to near-infrared, by reducing the oxide-thickness between the metallic layers[47]. Zhang et. al [144] investigated multi metal/dielectric stacks and the possible modes that can form. According to this study, "Only symmetrical modes survive for small dielectric thickness" for multilayer stacking [144]. Cao et al. [28] reported a considerable decrease in reflection and wide angular tolerance, achieved by a stack of 32 metal/dielectric layers (Au:Si , $10nm : 20nm$). They've attributed this to synergistic effect of "slow light" mode and localization of surface plasmon [28]. In fact the absorbed light has turned to plasmonic waves coupled with localized surface plasmons (LSP) [90].

Note that excessive field enhancement can also lead to degradation of the target molecules. Tesema et al. [123] investigated N-demethylation of methylene blue molecules to thionine in presence of plasmon and red light . Mukherjee et al. [99] investigated the effect of hot electron in hydrogen dissociation on gold nanoparticles under visible light. In this case, the surface plasmons excited on gold, decay into hot

electrons with energies between vacuum and that of metal work function, transferring into resonance of hydrogen molecule absorbed, triggering its splitting into two. The absorbed energy by nanomaterial will ultimately turn into heat (if not radiated back) as in any absorber of light [99, 96, 123]

Raman measurement is used by researchers for detecting traces of different materials. Therefore in contrary to other sensors usually designed for quantitative measurements [95, 13, 98, 49, 68, 71, 107], we have focused on maximizing sensor signal intensity for purpose of enhancing SERS structures capability for detecting minute traces of molecules, without quantizing it.

5.2   Optical Response of Bare SiNPs

This section focuses on SiNPs, e.g. nanostructures etched out of silicon. The details of the fabrication procedure of these structures are explained in chapter 2. Studying the scattering of light from SiNPs provides an understanding of their role in Raman generation. The optical response of SiNPs are studied both numerically and experimentally. SiNPs can serve as a substrate for metal/insulator/metal (MIM)-stacks. 5.4. However silicon's high refractive index makes it possible to achieve light-confinement and cavity resonance at visible wavelength. Silicon is a common choice for dielectric nano-resonators as it is relatively cheap and benefits from a very mature processing technology. The SiNPs of figure 5.1 illustrate one example of such structures.

Due to low density of fee electrons in the absence of doping, SiNPs interact with light primarily through their bound charges [38]. This means that when a SiNP is illuminated, the field is mainly confined inside the nanopillar and the scattering observed under dark-field is solely the result of participation of the bound charges and no plasmonic resonance effect takes place.
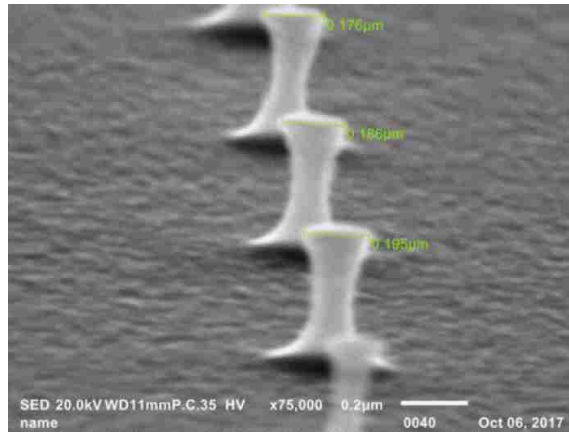
Figure 5.1: An SEM image of SiNPs fabricated by interferometric lithography (IL) and plasma etching (see chapter 2 for fabrication details). The specific SiNPs batch presented in this figure, have an average height and diameter of $400nm$ and $186nm$ respectively. SiNPs will be fabricated with $230nm$ diameter for Raman generation, and scattering measurements.

5.2.1 Permittivity of Silicon
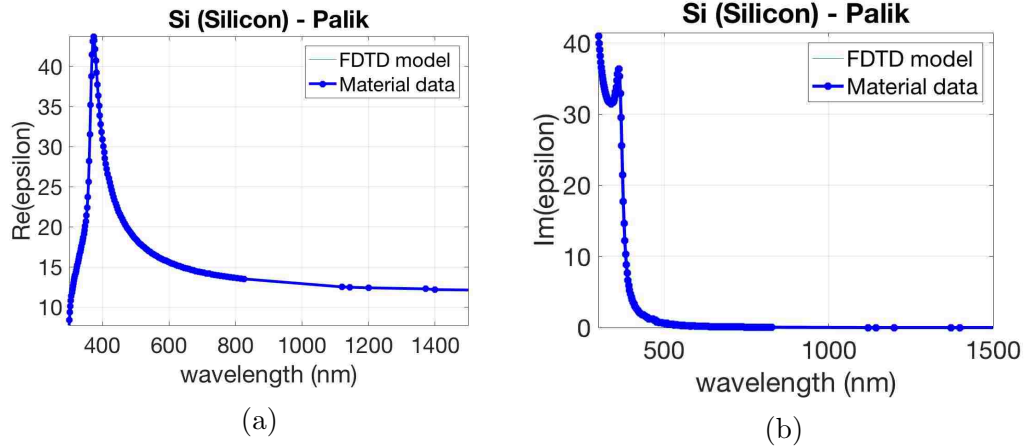
Figure 5.2: Permittivity data for silicon as provided by Lumerical software's data base. Dots show Palik's [105] experimental data used by Lumerical as the reference. The continuous line is a curve fit performed by Lumerical in order to determine permittivity at any intermediary wavelength.(a) Real part of silicon's permittivity (b) Imaginary part of silicon's permittivity

Permittivity of silicon has a deterministic effect in our subsequent analysis and numerical studies. The permittivity data used in our simulations are directly obtained from the database of LUMERICAL software. Lumerical uses a curve fit to the experimentally measured permittivity values of Palik [105] in order to determine permittivity at any intermediary wavelength as well. Figure 5.2 is duplicated from Lumerical's database and shows Palik's data along side the fitted curve.

5.2.2   Field-Enhancement by SiNP

As a dielectric resonator, SiNP can sustain confined optical resonance. Confinement and resonance together result in optical field enhancement. Fig. 5.3 illustrates a
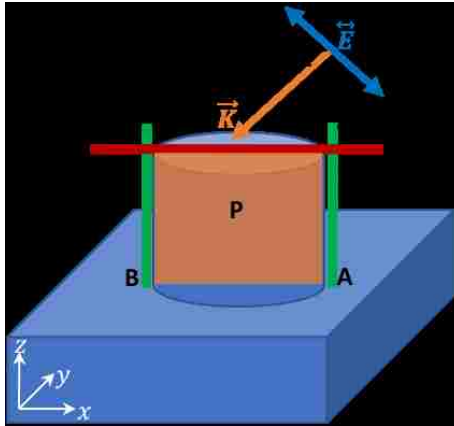
Figure 5.3: Illustration of the SiNP used for simulating the field enhancement and scattering. The lines AA, BB and CC are the locations where most of the simulations results are reported. These probe lines are located $1nm$ away from the structure surface.

SiNP and the lines along which the field enhancement is monitored in our simulations. Unless specified otherwise, the simulations reported in this chapter are done for a single nanostructure (bare SiNP and SiNP with a MIM-stack on top). The optical modes in these structures are excited by a 4 femto-second optical pulse with a wavelength of $630nm$. Fig. 5.4(a) shows the calculated near field resulting from
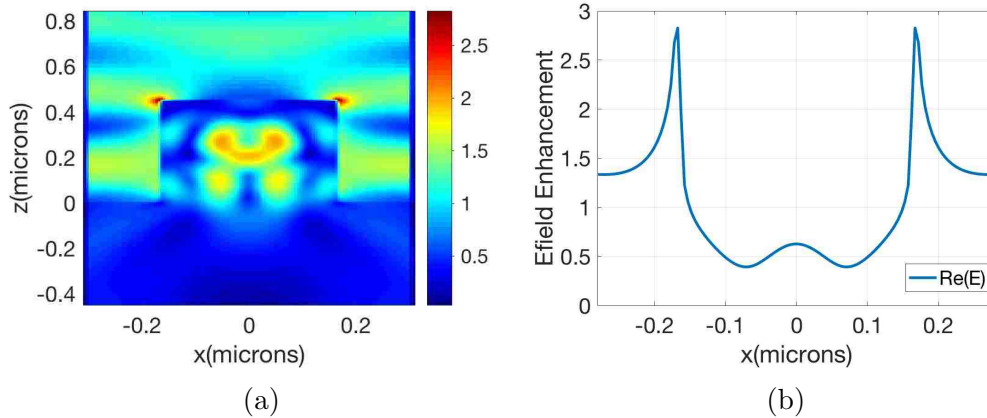
Figure 5.4: FDTD simulation results for E field intensity (a) Near field scattering by a SiNP on a silicon substrate (calculated with source power of unity). (b) field along C-C line on top of $450nm$ high SiNP.

illuminating a silicon nano-pillar. As shown in the figure the excitation of a resonant mode of the SiNP supports the capability of dielectric nanostructures to sustain and enhance the E-field. However with the exception of the sharp edges (on top), significant portion of the field resides inside the nanostructure and therefore is not accessible for surface interaction with molecules. Fig.5.4(b) shows the field along the C-C line and as expected, as mentioned above the field enhancement is maximum at the edges. Note that the enhancement is quantified relative to an incident field of unity. All the field enhancement measurements will be done along a line parallel to laser incidence, $1nm$ away from the plasmonic disks or SiNPs. The maximum of the fields happen at the edges of the metal disks.

5.2.3 Scattering Cross-Sections of SiNP: Numerical Analysis

It is well-known that SiNPs with different dimensions appear with different colors under the dark field microscope (see Fig. 5.6). This observation indicates that the scatterings is frequency dependent and in particular some peaks should be observable

in the visible region. The location and the amplitude of these scattering peaks are also associated with the resonances in SiNP and therefore the corresponding field enhancement. Given that local field enhancement is very difficult to measure, usually the scattering and absorption cross-sections and their frequency dependence are the primary sources of information about the field enhancement and performance of the SiNP as a Raman enhancement site. As such we have used finite difference time domain (FDTD) method to investigate the impact of SiNP geometry (both height and diameter) on the optical responses of SiNPs. Fig. 5.5 shows the calculated
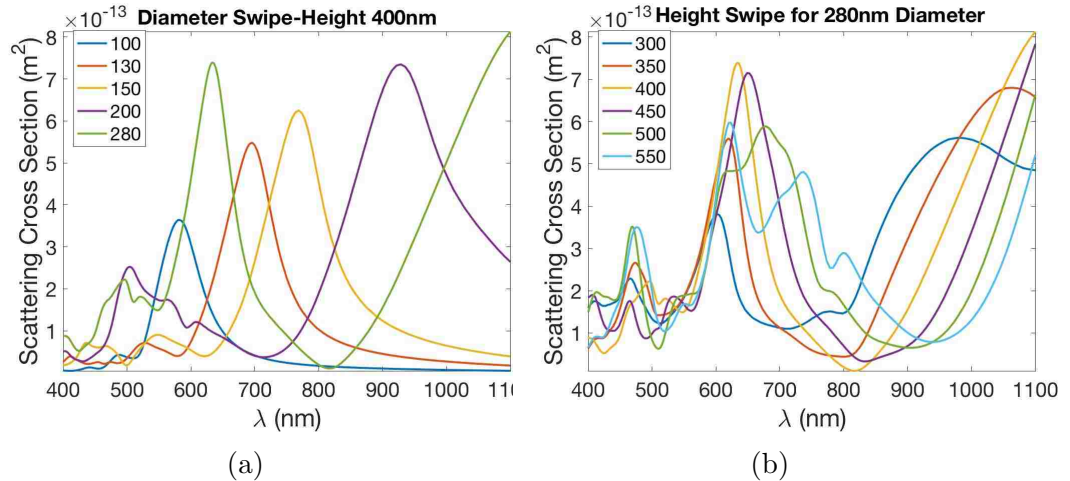
Figure 5.5: Calculated scattering cross-section for SiNPs with different diameters and heights. (a) Height $= 400nm$ and diameter$=100nm$, $130nm$, $150nm$, $200nm$ and $280nm$. (b) Diameter$=280nm$ and height $= 300nm$, $350nm$, $400nm$, $450nm$, $500nm$, and $550nm$.

scattering cross-section as a function of excitation wavelength, at different heights and diameters. In part-a the height is kept constant at $400nm$ and the diameter is changed ($100nm$, $130nm$, $150nm$, $200nm$ and $280nm$). In part-b the diameter is kept constant at $280nm$ and the height is changed ($300nm$, $350nm$, $400nm$, $450nm$, $500nm$, and $550nm$). As evident from the plots, that at a fixed height the resonant peak can be tuned by changing the pillar diameter without significant impact on its spectral width (that is proportional to the quality factor of the corresponding

resonant mode). On the other hand changing the pillar height at a fixed diameter mainly affects the resonant bandwidths and not the location of the peaks. These results provide a guide line for selecting the optimal wavelength for a given SiNP geometry of fabricate SiNPs for field enhancement at a given wavelength. For the wavelength used in our experiments (633nm), a SiNP with a diameter of 280 nm and height of 400 nm seem to be optimal (results in the largest and narrowest scattering). Note that at controlling the pillar height and diameter in nano-scale is a challenging and in practice one can only get close to the optimal values. While a strong and narrow resonant peak indicates the presence of a high-Q resonance within the SiNP, the resulting field enhancement and its usefulness for Raman enhancement is not guaranteed and require further investigation (regarding the location and the magnitude of the enhanced field).

5.2.4 SiNPs Scattering Cross-Section: Experimental Results

The fabricated SiNPs of Fig. 5.6 are $400nm$ in height and $230nm$ in radius. The periodicity of this nano-pillar array is $2.1\mu m$. Scattering data of white light by these silicon nano-pillar structures are shown in Fig 5.7. In order to determine the scattering of the light from a single SiNP, the light should be focused on a single nanopillar. While the beam spot size can not be in the scale of a single SiNP ($230nm$ in radius) but it can be focused to a size smaller than the period of the array ($2.1\mu m$). Fig. 5.7(a) shows the results of 20 measurements.

As can be seen, the scattering can be different based on the position of the light compared to the single SiNP (we can not center the light in the middle of pillar since the pillar is much smaller than the wavelength used in measurement). This is because, different incident angles on SiNPs can stimulate different resonance frequencies. However averaging the results of 20 data-sets can presents the scattering
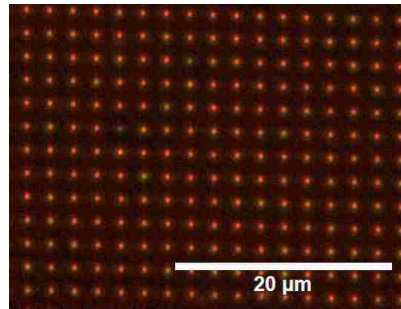
Figure 5.6: Dark-field image of a SiNP array fabricated using Ni mask over silicon. The nanopillars are $400nm$ in height and $230nm$ in radius. The pitch is $2.1\mu m$

(a)   (b)
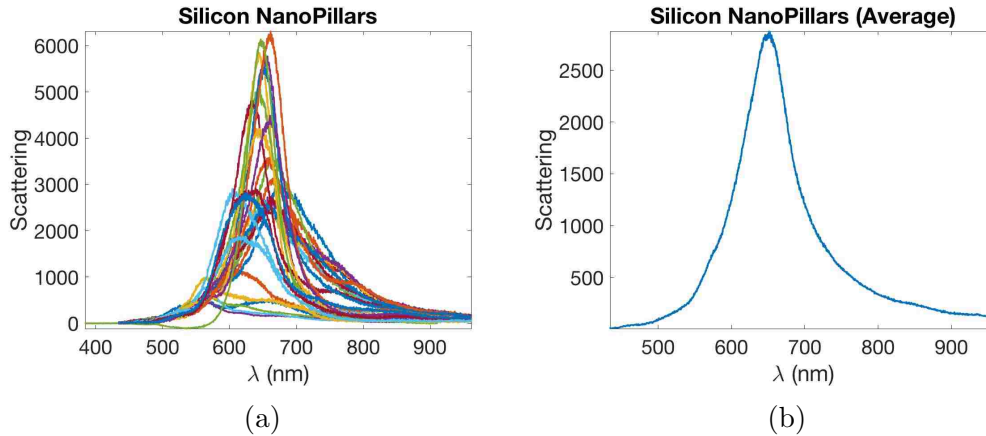
Figure 5.7: Experimentally measured scattering cross-section of an individual SiNP. (a) Shows the results of 20 measurements. The variations associated with optical alignment. b) is the average of the 20 measurements.

cross section of nanopillar more reliably (see Fig. 5.7(b)). The variation of the peak wavelength and the spectral shape is most probably associated with simultaneous excitation of various modes. However the average value of the measured scattering cross-section is in relatively good agreement with the simulation results in terms of the resonant wavelength (in particular with the green curve in Fig. 5.5(a) corresponding to the SiNP with height=400 nm and diameter=280 nm).

5.3 The Absorption/Scattering Cross-Sections of Gold Nanodisk And Gold Nanodisk Stacks

The objective of this section is to find the resonance frequencies and absorption/scattering cross-sections of the gold (Au) nanodisks as well as $Au/SiO_2/Au$ stacks (also referred to as MIM stack). The structures studied in this section are considered to be surrounded by air and don't have any substrates. Along with the previous study (for SiNP), this study will allow a better understanding of the absorption/scattering cross-sections of the more complicated structures in the form of gold nanodisks that will be discussed later. Both scattering cross section and resonance frequency play a decisive role in generating Raman signal. Clearly if the excitation laser wavelength is closer to the scattering cross section peak of the metallic nanostructure, it will generate a larger localized plasmonic resonance for the Raman enhancement.

5.3.1 General Formulation of Plasmonic Nano-Disk Resonators

Eq. 5.1 can be used to investigate the plasmonic effects of the metal dielectric junctions in cylindrical structures. This equation can be written in the Hankel form of eq. 5.1, [143],

$$E_z(\rho, \phi, z) = a(z) \left[H_m^2(k_{gsp}\rho) + r_m H_m^2(k_{gsp}\rho) \right] e^{im\phi}$$

$$k_{gsp} = k_0 \sqrt{\epsilon_d + 0.5 \left(\frac{k_{gsp}^0}{k_0} \right) + \sqrt{\left(\frac{k_{gsp}^0}{k_0} \right)^2 \left[\epsilon_d - \epsilon_m + 0.25 \left(\frac{k_{gsp}^0}{k_0} \right)^2 \right]}}$$ (5.1)

whew k_0 stands for the vacuum wave vector and $k_{gsp}^0 = -2\epsilon_d/\epsilon_m$ stands for the wave vector of the Surface Plasmon Polaritons (SPPs) in the limit of very small gap thickness ($d \to 0$). Depending on the boundary conditions, toroidal modes [8], Di-pole, Quadra-pole [143] and other modes are possible. For example, toroidal resonances

[143] can happen if Dirichlet boundary condition exists at the edges of the dielectric layer($E_z \rho = 0$). From the resonance condition that can be achieved from these Hankel equations it's possible to estimate the frequencies of the scattering cross section peaks. While analytical solutions for simple cases may provide some physical insight, practically determination of resonance frequencies and absorption/scattering cross-sections for more complex structures can be done only using numerical methods.As such in this section we use FDTD for these calculations.

5.3.2 Cross Sections Calculated by FDTD Method

Here we calculate the scattering and extinction cross sections of stand-alone gold nanodisks as well as a stack of two gold nanodisks separated by a 15nm-thick layer of SiO_2. The diameters used for studying stand-alone gold nanodisks ($25nm$ thick) cover a wide range from $60nm$ to $330nm$. The $Au/SiO_2/Au$ ($25nm/15nm/25nm$ thickness) has been only studied at $diameter = 50nm$ & $230nm$. The two later dimensions match the samples that are fabricated. The structures are considered to be suspended in air for the purposes of these simulations. Figure 5.8 shows the absorption, scattering and extinction cross sections for stand-alone gold nanodisk as well as $Au/SiO2/Au$ stacks, while Figure 5.9 shows the movement of the peak frequency for different diameters.

Also the results of Figure 5.8 are summarized in Fig. 5.10. These diagrams show the impact of diameter on the peak-value of scattering cross-section as well as the wavelength where it happens. The simulation results indicate that these parameters (the peak-value of scattering cross-section as well as the wavelength where it happens) increase as the diameter of the nanodisks increase. In order to study the effect of adding a second Au disk the scattering data of Figures 5.8(d) and 5.9(a) are compared in Fig. 5.11. By changing the single disk to stack, the peak at $827nm$ wavelength
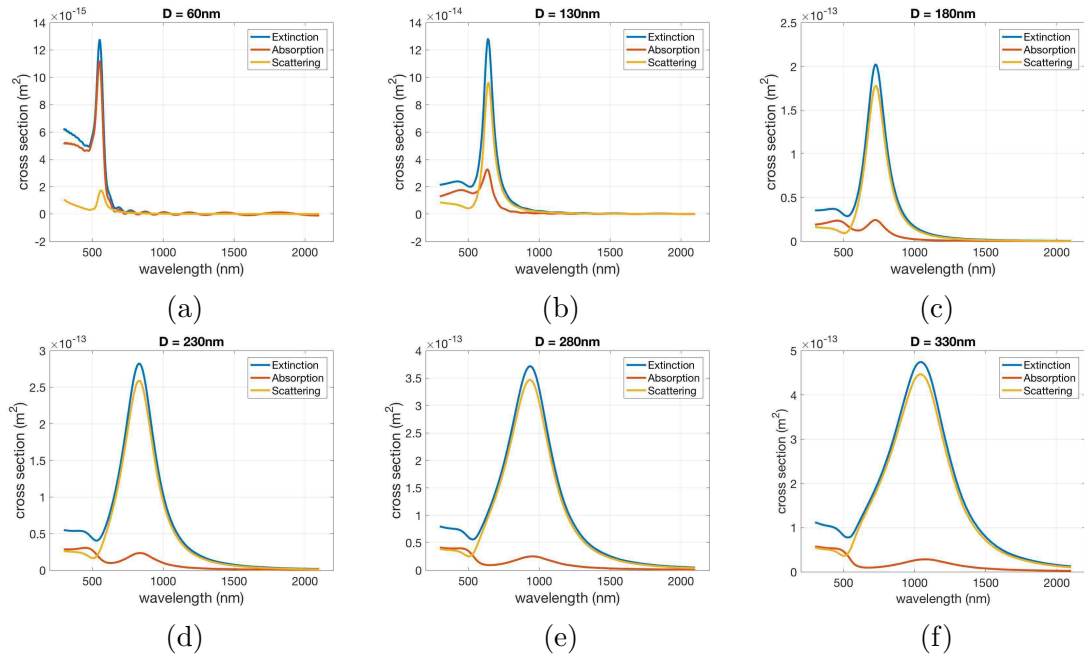
Figure 5.8: Extinction, Scattering and Absorption cross-sections of gold nanodisks of different diameters floating on air (without substrate) are calculated using FDTD method. Each sub-figure represents the results for a specific diameter and $25nm$ gold thickness. These diameters are: (a) $60nm$ (b) $130nm$ (c) $180nm$ (d) $230nm$ (e) $280nm$ (f) $330nm$.

moves to $808nm$. For the case of stack, as seen in figure 5.11 a secondary peak appears too, at $1400nm$. The smaller peak at near-IR is thus the result of interaction between the nanodisks. It is also evident that the absorption has increased in near-IR without any scattering increase at the same wavelength. Theoretically we know that there is a peak in infrared which is related to odd modes. Odd mode means that the plasmonic waves of the upper and lower disks are antisymmetric. Therefore, the far-field radiations from this mode cancel out and we don't detect any scattering at infrared (due to pi phase difference between the two plates oscillation). However electric field exists between the top and bottom metal disks, inside the dielectric or air between the two plasmonic disks.
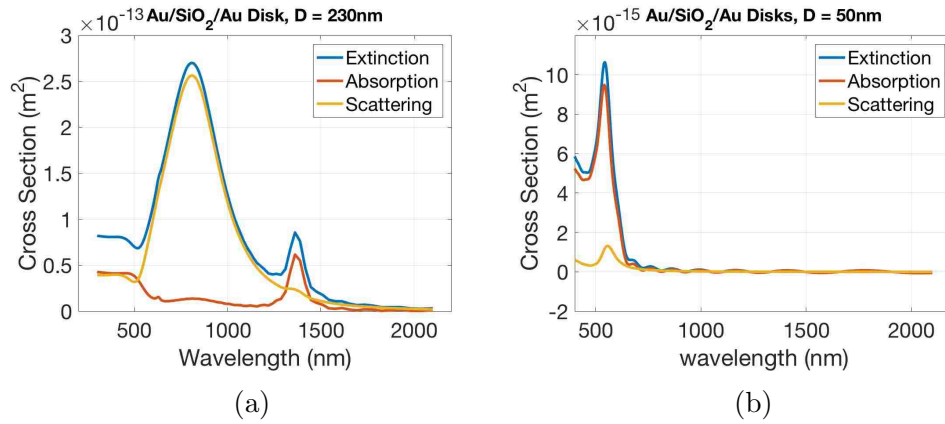
Figure 5.9: Scattering cross-sections of stacks of different diameters, calculated using FTDT method. These diameters are: (a) $230nm$. The minor peak at $1400nm$ belongs to odd mode resulting from closing two single disks (this is in agreement with literature). (b) $50nm$. Whole the spectrum has blue shifted. We expect the peak here at visible to be the same odd mode in Figure 5.9(a) which has blue shifted.
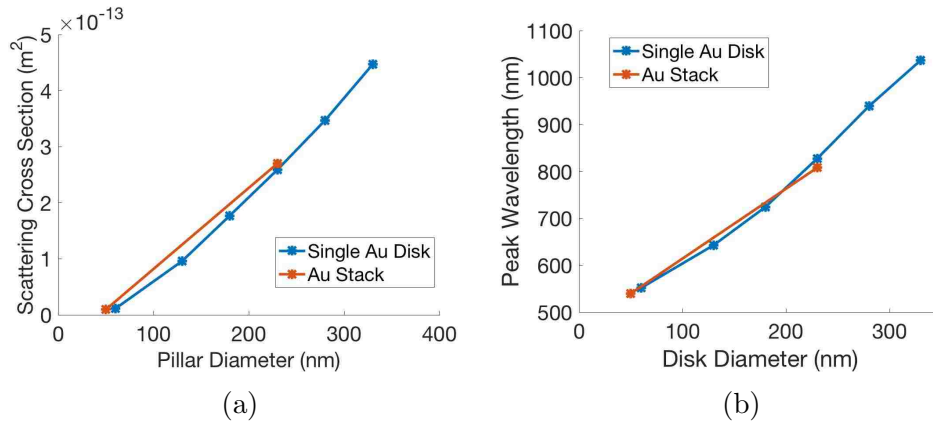
Figure 5.10: Summary of the simulation results for scattering cross-sections of gold nanodisks as well as $Au : SiO_2 : Au$ nanodisk-stacks with different diameters. (a) Peak value of the scattering cross-section as a function of disk diameter. (b) Wavelength at which the cross-sections reaches its maximum value as a function of disk diameter.

5.4 Plasmonic Structures on Top of SiNP

The main purpose of this section is to study the effects of lifting the metallic nanodisk or metal/insulator/metal (MIM) stacks, off the substrate through fabricating
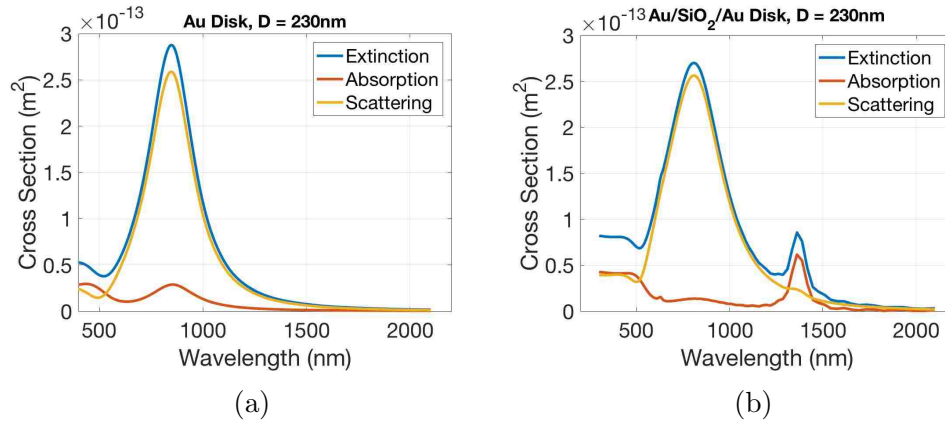
Figure 5.11: The scattering data of 230nm plasmonic disks repeated here for ease of comparison. (a)Au nanodisk (b) $Au/SiO_2/Au$ nanodisks-stack

them on SiNPs (note that collectively we refer to these as plasmonic nanostructures). We will study both single metallic layer and metal/dielectric/metal cases (stacks). The dielectric/semiconductor SiNPs of Sec. 5.2 can be used as a platform for deposition of metal and metal/dielectric/metal stacks (see Sec.5.3). The SiNP can positively effect field enhancement of metallic structure used in Surface Enhanced Raman Spectroscopy(SERS). The metallic nano-structures deposited on the nanopillars are highly exposed and offer high ability to generate field-enhancement and Raman scattering from different molecules. These structures usually generate very high electric field enhancements specially at the edges of the metal tips. Plasmonic structure (with negative real permittivity and usually low imaginary permittivity) can focus the field outside of the nanostructure, mainly near the edges. The field enhancement by plasmonic structures, is mainly achieved by involvement of the metal's surface plasmons. Surface plasmons are oscillations of conductive surface electrons of a plasmonic metal [144]. Using two metallic layers which are separated by a thin dielectric, can yield in significant field enhancement, at a relatively different resonance frequency compared to that of a single metal. This resonance happening at the same frequency for both plasmonic disks is called a hybridized resonance. One resonance frequency of a single

disk, by putting them closely on top of another disk with same type and dimension, yields two frequencies related to odd modes (at lower frequency) and even modes (at higher frequencies).

Numerical analysis (FDTD) is used to study the field enhancement location and magnitude. These simulations are used to compare the effects of a single Au layer over a SiNP and a stack of $Au/SiO_2/Au$ over a SiNP. Also considerable simulations are used to study the effects of diameter, dielectric-side-etch, polarization, angle-of-incidence, SiNP-height on field enhancement. We have briefly checked if the mesh resolution of our simulations is in an acceptable range.

5.4.1   Field Enhancement

FDTD simulations are carried out using Lumerical to study electric field enhancement in devices composed of plasmonic structures (single metal layer or MIM) fabricated on top of dielectric nano-pillars. Three main studies have been done here; two of them, using only one plasmonic layer on nanopillars and one with a metal/dielectric/metal stack on nanopillars. The structure studied in Figs. 5.12(a), 5.12(b), 5.12(c) are Au nanodisks and $Au/SiO_2/Au$ stacks, respectively. The nanopillars of Fig. 5.12(a) & 5.12(c) are made of Si while the nanopillar of Fig.5.12(b) is made of SiO_2. All the diameters used here are $80nm$. The nanopillars have a height of $400nm$. The Au layers are $25nm$-thick while the SiO_2 separating the two layers of gold in Fig. 5.12(c) has a thickness of $20nm$. The input pulses used for these calculations have a wavelength of $633nm$.

A close look at the results of Fig.5.12(a) reveals that although some enhancement is visible, half-way up the nano-pillar, the main enhancement is confined to a small region close to the edge of the Au layer. This is expected, considering the difference in permittivities of Au and the SiNP. Note that as shown in section 5.4.6. In addition
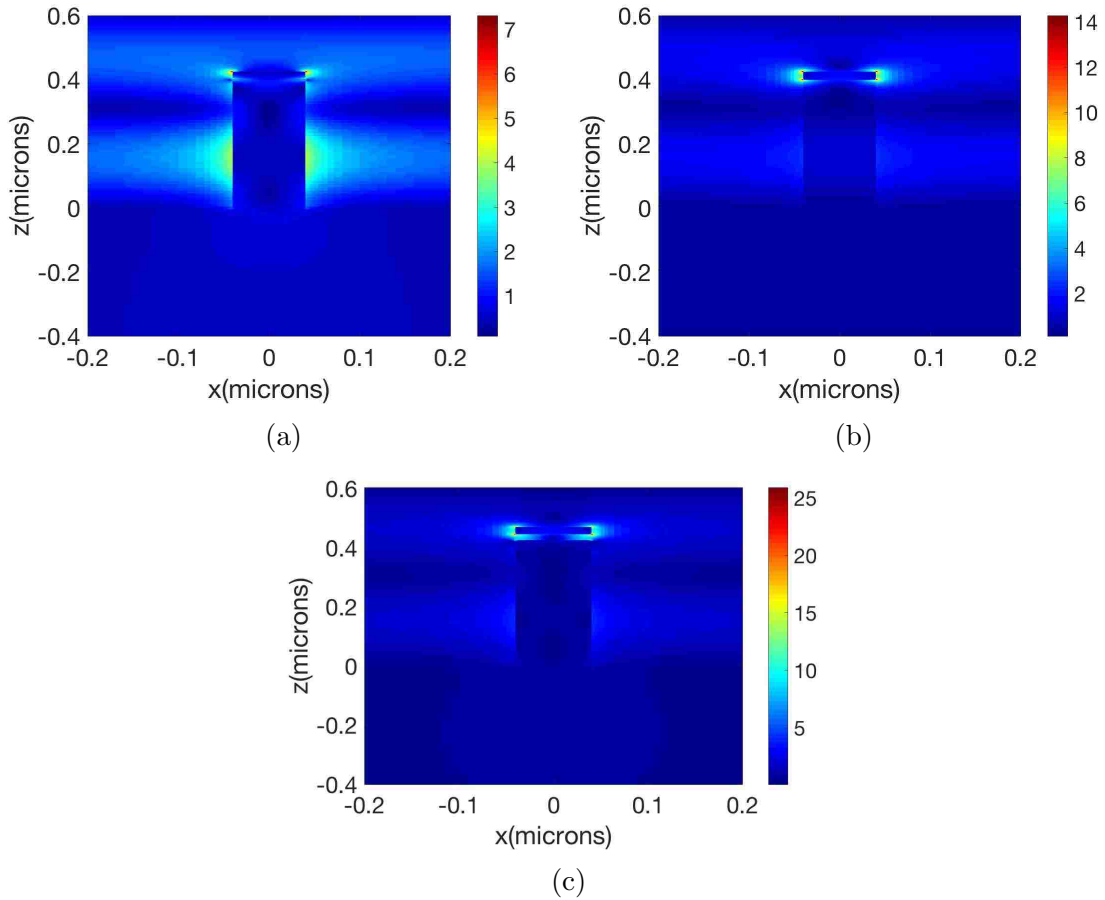
Figure 5.12: Electric field magnitude for plasmonic structures over nanopillars. All structures have a diameter of $80nm$. The height nanopillars are $400nm$. The thicknesses of Au and $SiO2$ layers are $25nm$ and 20 respectively. The configurations used are: (a) Au layer over Si nanopillar; (b) Au layer of SiO_2 nanopillar and (c) $Au/SiO_2/Au$ layers over Si nanopillar

to the interaction between the Au nanodisks in stack, the coupling between the plasmonic modes and the SiNP modes plays an important role in the overall field enhancement.

Replacing the SiNP with silica (SiO_2) nanopillar allows further enhancement in the field as can be seen in Fig. 5.12(b). While the enhancement is improved by more than twice, our studies are only focused on SiNp. A closer look at the results of

Fig. 5.12(c) reveals that the field around the lower Au-layer is not even comparable with the field around the top Au-layer. The reason can be understood by referring back to the results of Figs. 5.12(b) and 5.12(a) and the fact that the only difference between the structures used, is the material of the nanopillars. The top Au-layer of Fig.5.12(c) is deposited over a layer of SiO_2 which is a dielectric while the lower Au-layer is on a semi-conductive SiNP.

5.4.2 Effect of Changing The Diameter

The effects of the diameter on the electric field and its enhancement in $Au/SiO_2/Au$ stacks over SiNPs, is studied over a wide range of diameters. Except their diameters, all the physical parameters of the nanostructures studied here are identical to those used in Sec. 5.4.1. Figures 5.13(a)-(d) show the numerical simulation results and the field distribution around the nanostructures for $d = 40nm, 90nm, 260nm$ and $340nm$, respectively. The relationship between the peak value of the field and the diameter of the nano-pillars is summarized in the graph of Fig. 5.13(e). As can be seen in this graph, in general larger fields are observed at smaller diameters but optimized diameter is not necessarily the smallest diameter studied.

5.4.3 Effect of SiO_2 Side Etch

Slightly Etching the rim of the oxide-layer between the two Au-layers will expose the edges of the metallic layers. This can have significant impact on the resulting Raman signal as it improves the interaction cross-section of the enhanced field with the target molecules. Except the slightly smaller diameter of SiO_2 (etched $10nm$ from the sides), all the physical parameters of the nanostructures studied here are identical to those used in Sec. 5.4.1.
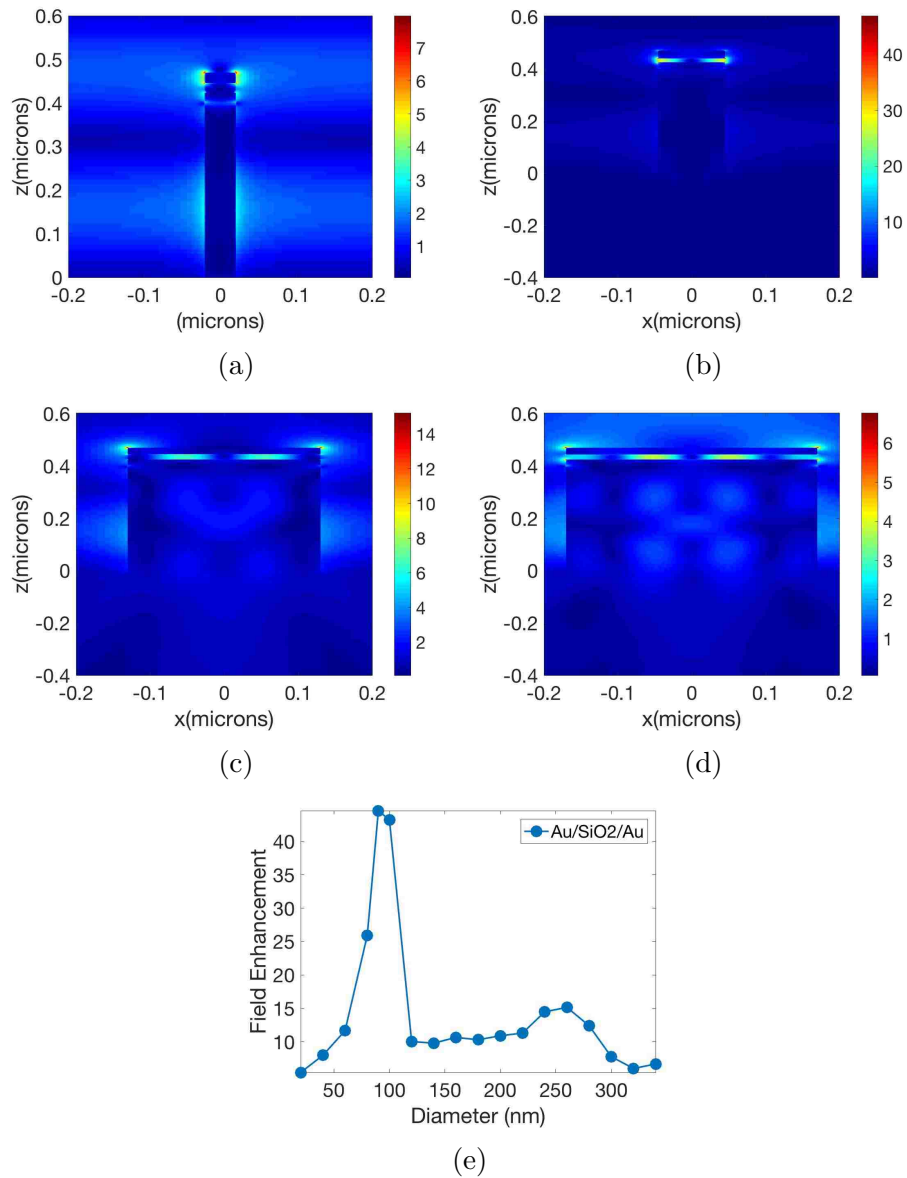
Figure 5.13: Excited E-field distribution for various diameters of nanostructure ($Au/SiO_2/Au$-stack on SiNP). (a) $d = 40nm$ (b) $d = 90nm$ (c) $d = 260nm$ (d) $d = 340nm$ (e) Peak value of the electric field is plotted as a function of diameter.

Fig. 5.14 shows the electric field distribution after the diameter of SiO_2 layer is reduced by 10nm. Reducing the SiO_2 diameter does not effect the field distribution considerably but slightly increases the peak value.

107
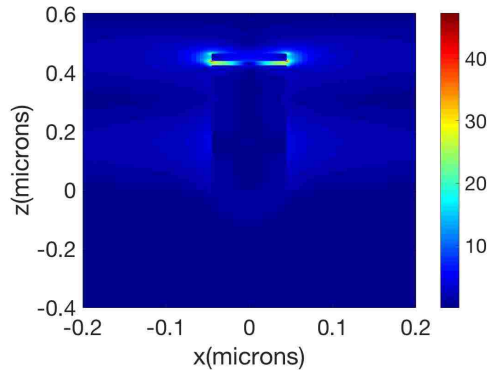
Figure 5.14: Electric field after etching the SiO_2 layer for $10nm$ around its rim. This exposes the Au layers at the edges. The field distribution is almost not effected by this etch process.

5.4.4 Effect of Polarization and Angle of Incidence

The polarization of the light and the angle at which it illuminates the nanostructure, can have a significant effect on the achievable field enhancement. All the physical parameters of the nanostructures studied here are identical to those studied in Sec. 5.4.1. However the polarization (TE or TM) and the angle of incidence are varied to study their impact. Fig. 5.15 shows the electric field distribution and its peak values resulting from illuminating a $Au/SiO_2/Au$-stack on a SiNP, when the incident beam is TM polarized. The light source illuminates the sample with different incident angles ranging from $0^o - 60^o$. 0° corresponds to normal incidence to the top surface (Au layer). As evident from part-e, the maximum field enhancement occurs when the Au-SiNP is illuminated with a TM polarized beam at 30° incidence angle. Fig. 5.16 shows the electric field when illuminating the nanostructure with a TE light with an incident angle 45°. The numerical results show no considerable enhancement when using a TE source for any of the incidence angles used. Thus only the simulations results for 45° incident angle case, are presented here.
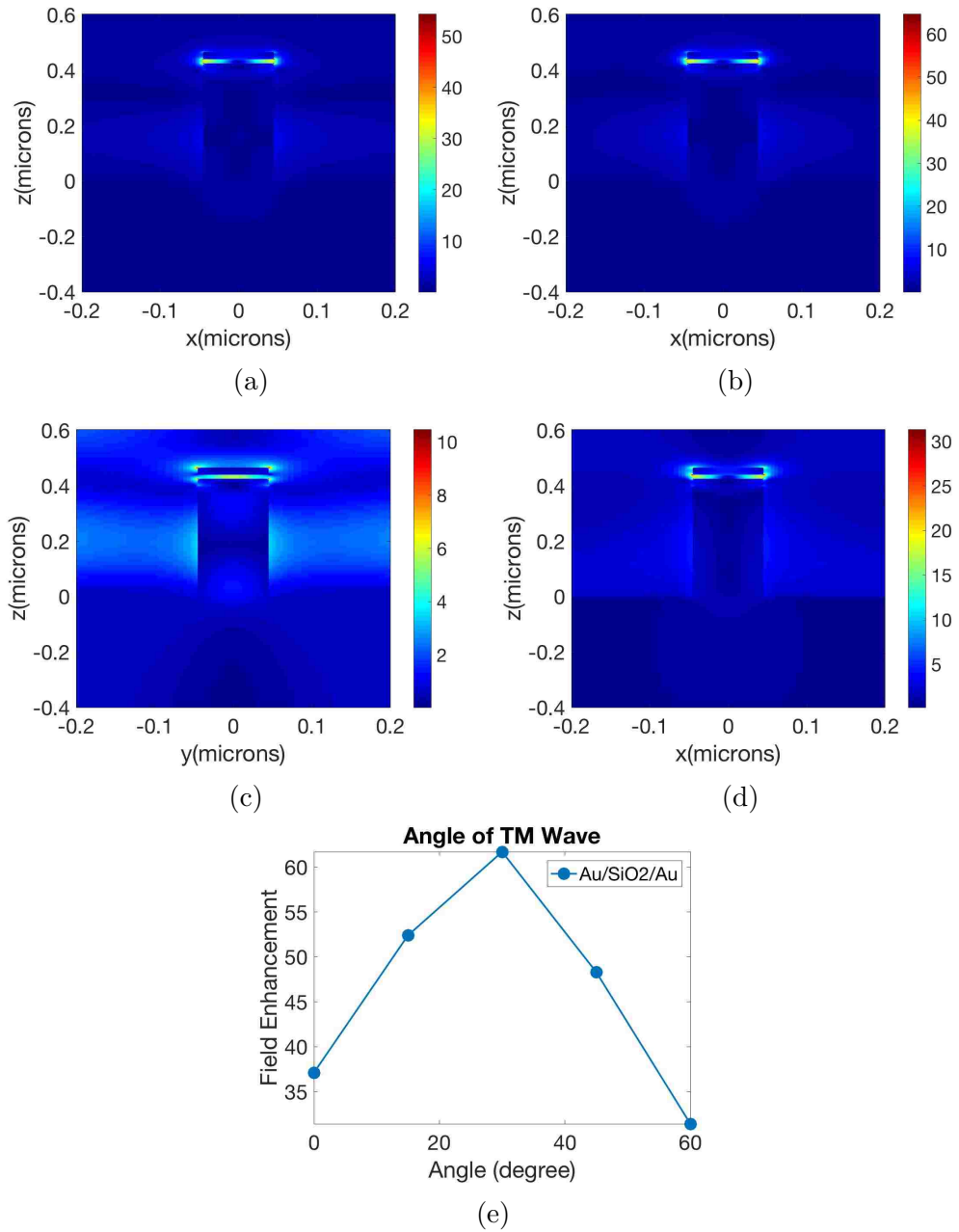
Figure 5.15: Electric field when illuminating a $Au/SiO_2/Au$ nanostructure fabricated on a SiNP with a TM polarized-light at different incident angles of (a) 15°, (b) 30°, (c) 45°, and (d) 60°. (e) Maximum E-field plotted against incident angles for TM illumination.
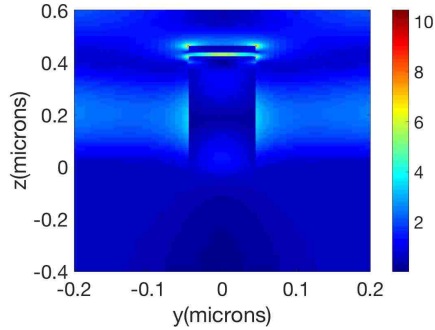
Figure 5.16: Electric field distribution when $Au/SiO_2/Au$-SiNP nanostructure on the silicon substrate is illuminated by TE polarized-light with an incidence angle of 45°

The comparison of field enhancement factor (EF) at table 5.1, for different designs, shows the effect of material of nanopillar and effect of stacking on top of SiNP (height is fixed at $400nm$). Also at fixed radius of $45nm$, effect of angle is shown for stack over SiNP. For each polarization, the maximum field, happens at a different angle, which is written beside each of the polarizations at table 5.1.

Table 5.1: **EF for Plasmonic Structures on Nano-Pillars (FDTD)**

NP Radius (nm)	Illumination Angle (^{o})	Enhancement Factor		
		Au/SiNP	$Au/SiO_2 - NP$	$Au/SiO_2/Au/SiNP$
40	Orthogonal	7	14	25
45	Orthogonal	-	-	44
45	TM 30° $*$	-	-	62
45	TE 45° $**$	-	-	11

$*$: Optimum angle for TM
$**$: Optimum angle for TE
Illumination source E-field: $1(V/m)$

5.4.5 Scattering Cross-Sections of SiNPs With $Au/SiO_2/Au$ Stack

In Figure 5.17 and 5.18 the calculated extinction, absorption and scattering cross-sections for gold nanodisk(s) on SiNP are compared to those of the isolated gold nanodisk and SiNP in order to understand the possible formation of coupled modes. The calculations are performed for two sets of nanostructures with diameters of $50nm$ and $230nm$. In figure 5.17(d) (gold nanodisk on SiNP) two peaks at $530nm$ and $669nm$ have emerged that existed neither in Figure 5.17(a) nor 5.17(b) (i.e. these peaks are missing in the cross sections of floating gold nanodisk and bare SiNP). The same holds for silicon stack ($Au/SiO_2/Au : 25nm/15nm/25nm$) in Figure 5.17(e) compared to Figures 5.17(a) and 5.17(c).

In Figure 5.18, the same cross-sections are compared for nanostructures with diameter of $230nm$. Single floating gold has a peak at $850nm$, and floating $Au/SiO_2/Au$ has two peaks at $815nm$ and roughly $1400nm$. As we mentioned earlier, the week peak of scattering cross section versus the strong absorption is a verification of our assumption that this peak belongs to odd mode. This means the top and bottom plasmons oscillations have π phase difference, significantly reducing the far field (and therefore the measured scattering cross section).

From comparison of the SiNP scattering with scattering of gold on SiNP and gold stack on SiNP, we see that below $800nm$ wavelength they have the same cross section spectrum with similar peaks (altogether the approximate distance of the peaks of the three cases in figures 5.18(a), 5.18(d), and 5.18(e) are below $10nm$ for wavelengths below $800nm$). This similarity is not seen for the floating cases of Figures 5.18(b) and 5.18(c) compared to SiNP cross sections below the same range of frequencies. For further analysis we simplify the problem. Since our main interest is identifying the peaks associated with plasmonic resonance, we focus on the absorption curves.

(a)

(b)

(c)

(d)

(e)
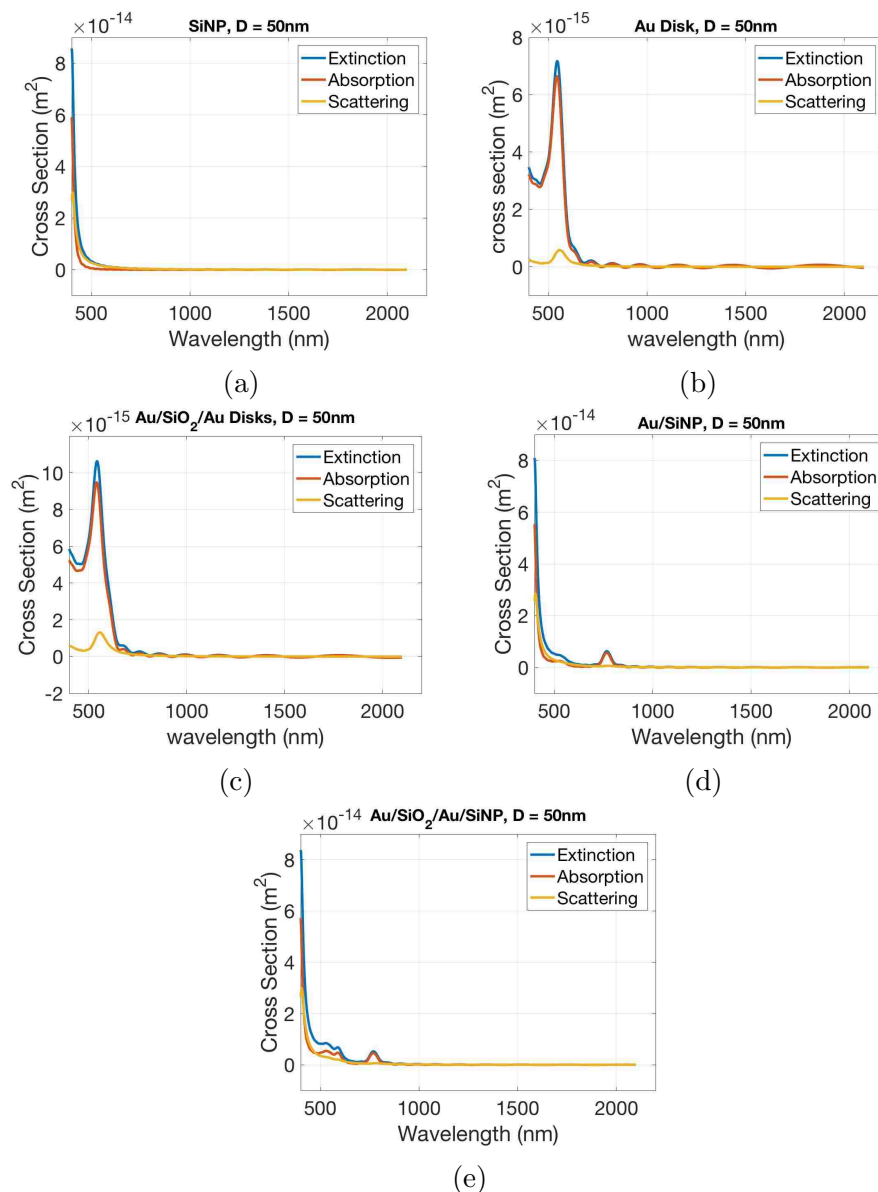
Figure 5.17: Comparison of extinction, scattering and absorption cross sections for nanostructures with a diameter of $50nm$: (a) SiNP (height=$400nm$), (b) Floating single gold nanodisk (thickness=$25nm$). (c) Floating $Au/SiO_2/Au$ stack (gold thickness=$25nm$, silica thickness=$15nm$) (d) Au on SiNP,(gold thickness=$25nm$,pillar height=$400nm$) (e) $Au/SiO_2/Au$ on SiNP(gold thickness=$25nm$, silica thickness=$15nm$, pillar height=$400nm$).
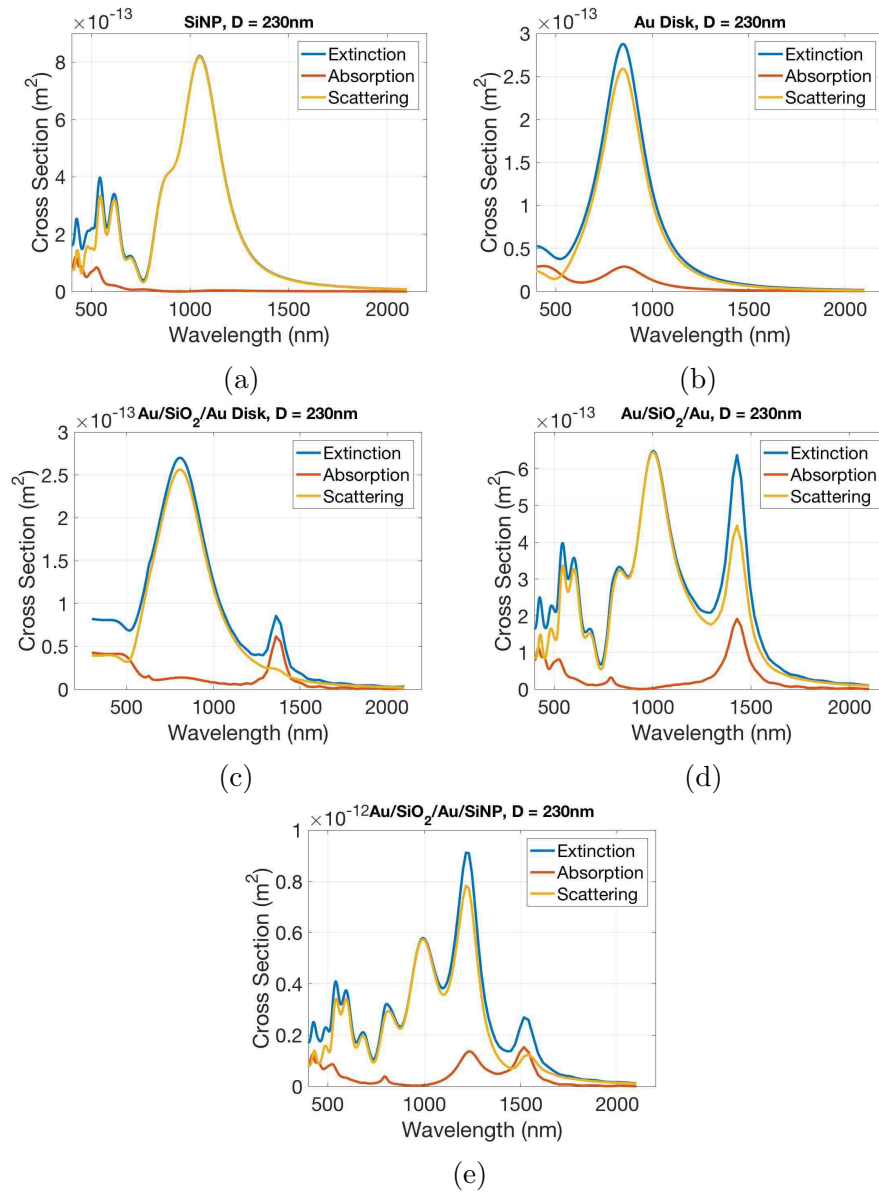
Figure 5.18: Comparison of extinction, scattering and absorption cross sections for nanostructures with a diameter of $230nm$: (a) SiNP (height=$400nm$), (b) Floating single gold nanodisk (thickness=$25nm$).   (c) Floating $Au/SiO_2/Au$ stack (gold thickness=$25nm$, silica thickness=$15nm$) (d) Au on SiNP,(gold thickness=$25nm$,pillar height=$400nm$) (e) $Au/SiO_2/Au$ on SiNP(gold thickness=$25nm$, silica thickness=$15nm$, pillar height=$400nm$).
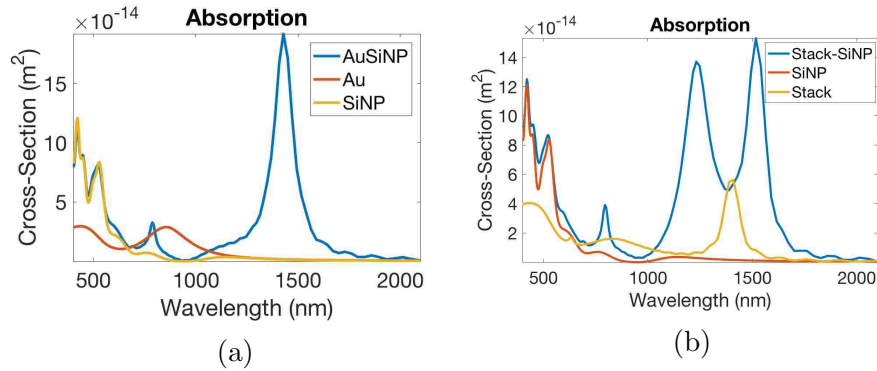
Figure 5.19: Comparison of absorption cross section for $230nm$ diameter structures of $400nm$ height, $230nm$ diameter SiNP, floating plasmonic structure, and plasmonic structure on SiNP (a) Au disk $(25nm)$ as plasmonic layer (b) $Au/SiO_2/Au$: $25nm/15nm25nm$ stack as MIM

The absorption cross sections of the $230nm$ nanopillars with bare SiNP, floating gold nanodisk stack, and gold nanodisk stack on top of SiNPs is shown in figure 5.19(a) and 5.19(b). The absorption of SiNP is expected to be large for wavelengths below $600nm$ due to the large imaginary part of the permittivity (figure 5.2. In figure 5.19(a) it's clear that the major role player in absorption cross section below $620nm$ wavelength is SiNP loss. SiNP shows a minor peak at $763nm$. Since the imaginary part of silicon decreases continuously for wavelengths above $600nm$ we don't expect the same behavior. However if we consider that scattering (resonance) of SiNP changes the direction of the normally incident wave and therefore the propagation length of light inside the underlaying silicon substrate (inside the simulation region using FDTD), we can infer the peak in absorption, to a scattering happening by the nanopillar. Also there is a resonance for metal at $821nm$. The shape of the mode of the resonance of the plasmonic wave and the pillar is unknown, but these two potentially can hybridize (due to close resonance frequencies) and yield the peak at $(794nm)$. The effect of under laying SiNP is seen for the gold stack over SiNP at $1232nm$ and $1517nm$ in figure 5.19(b). The two new peaks don't belong to either of SiNP or floating gold stack.

5.4.6   Coupling of Plasmonic and Cavity Resonances
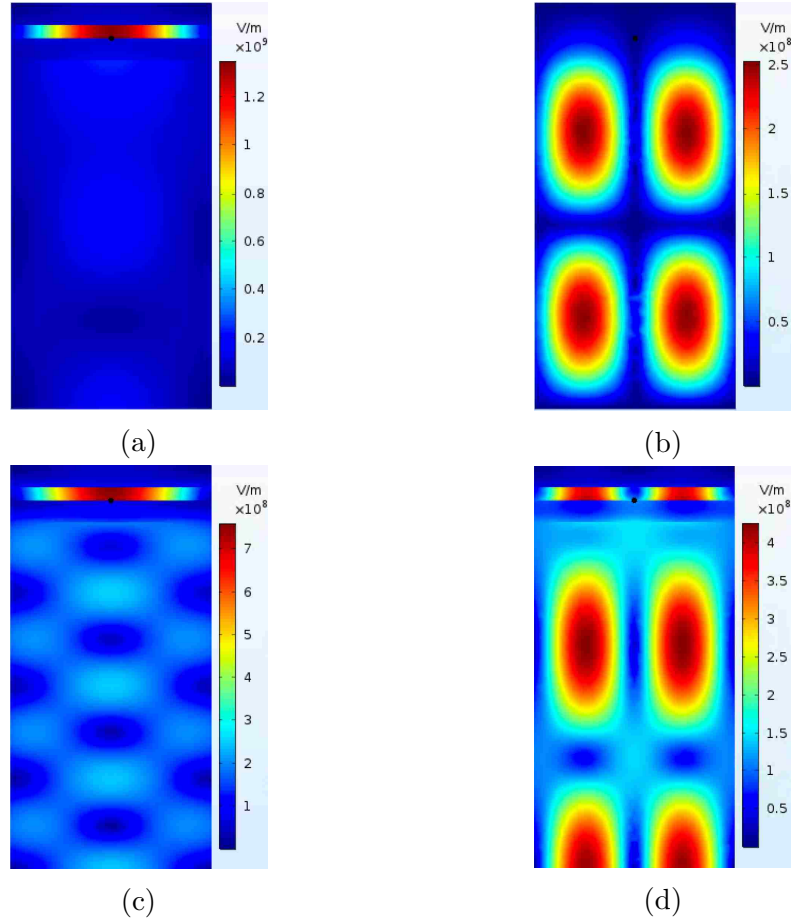
Figure 5.20:   FEM simulation for investigating the possible coupling of plasmonic wave of MIM and SiNP (a) plasmon resonance seen for $Au/SiO_2/Au$: $25nm/15nm/25nm$ with $230nm$ diameter at $317THz$ (b) Cavity resonance inside the $400nm$, height ($230nm$ diameter) at $377THz$ (c) Weak coupling between the plasmonic resonance and cavity resonance at $448THz$ (d) Coupling of plasmonic resonance and cavity resonance at $440THz$

   The FDTD simulations of Sec.5.4.5 indicated that the SiNPs not only work as a platform to lift the plasmonic structures off the wafer surface, but they can also interact with the plasmonic layers. The observed enhancement is due to localization of resonating plasmon at the edges. Using Finite Element simulations, we can study

this interaction even better through obtaining the resonance modes of the overall structure. Fig. 5.20 shows the resonance modes of a $Au/SiO_2/Au$ stack over over an individual SiNP. The SiNP is $400nm$ tall and has a diameter of $230nm$. The thicknesses of Au and SiO_2 layers are $25nm$ and $15nm$, respectively. Resonance mode at $318THz$ shows plasmonic oscillations that are confined to the metal/dielectric/metal stack only (see Fig.5.20(a)). At the resonance frequency of $377THz$, the cavity resonance is happening inside the SiNP only (Figure 5.20(b)). Fig. 5.20(c) shows weak coupling between the plasmonic and cavity resonances at $448THz$. The resonance mode at $440THz$ shows strong coupling between the plasmon resonance and cavity resonances as shown in Figure 5.20(d).

5.4.7 Scattering Cross-Section of SiNP with Plasmonic Structures: Experimental Results

In order to experimentally study the effects of elevating the plasmonic structures by fabricating them on SiNPs, two sets of samples are prepared. The SiNPs of the two samples are identical. They have a height of $400nm$ and a diameter of $230nm$. The thicknesses of the deposited Au and SiO_2 layers are $25nm$ and $15nm$ respectively.

For the reasons mentioned before, it is difficult to make sure that light is completely focused on the nanostructure. Therefore more than 20 datasets have been collected for each sample by running 20 different measurements. By averaging these measurements, one can estimate the scattering cross-section of a single nanostructure. The scattering cross-section data and their averages are represented in Fig. 5.21. Clearly the scattering strength of the $Au/SiO_2/Au$-SiNP is larger than that of the Au-SiNP.
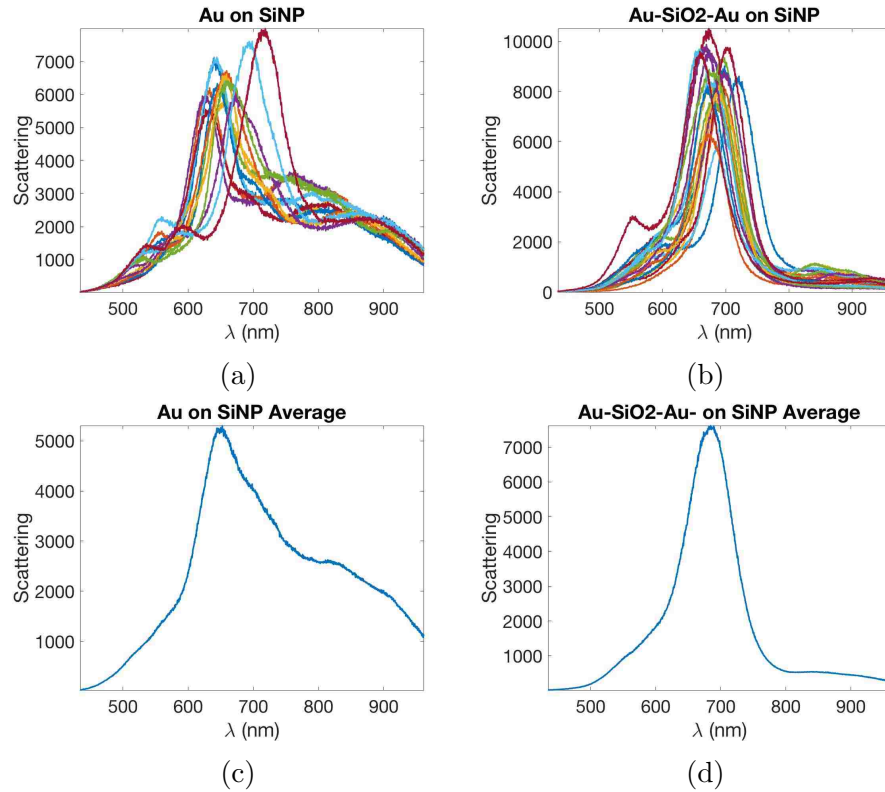
Figure 5.21: Experimentally measured scattering cross-section of *Au* and $Au/SiO_2/Au$ plasmonic structures fabricated on SiNPs. 20 different measurements are conducted and the data are averaged. (a) Scattering cross-section measurements from *Au* over SiNP. (b) Scattering cross-section measurements from $Au/SiO_2/Au$ over SiNP. (c) Average of measurements from *Au* over SiNP (d) Average of measurements from $Au/SiO_2/Au$ over SiNP

5.5 Raman Scattering Measurements

In this section Raman generation on MIM is studied in particular to compare the level of enhancement provided by different structures, understand the temporal and spectral evolution of the Raman signal in the vicinity of MIM (spectral evolution of the Raman signal). The measurements related to comparisons of Raman intensity are all carried out using a $1.5 * 10^{-5} M$ Thionine solution, as the test specimen, and identical illumination and sampling conditions. The measurements are performed after the

Chapter 5. Raman

nanostructures are wetted by $10\mu Liter$ Thionine solution and allowed to dry. The experimental studies of this section include Raman enhancement using bare SiNPs and Au nano-disks as well as Au, Au/SiO_2, $Au/SiO_2/Au$ and $Au/SiO_2/Au/SiO_2/Au$ nanodisks over SiNPs. Spectral evolution of Raman signal is studied using "Methylene blue" (MB) as the test specimen and Au,Au/SiO_2 and $Au/SiO_2/Au$ stacks over SiNP. Through this evolution (also known as demethylation) MB decomposes to Thionine.

5.5.1 Raman Enhancement By SiNPs

The Raman spectrum of bare SiNPs coated by Thionine molecules is presented in Fig 5.22. The measured spectrum (the peaks and their locations) is simply the
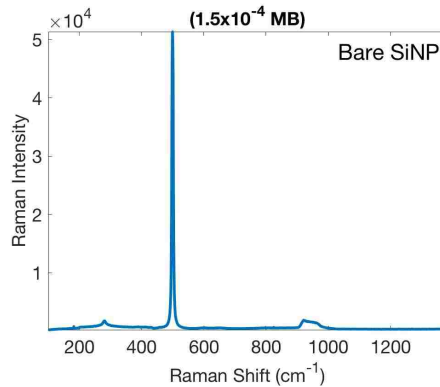
Figure 5.22: Raman spectrum after $10\mu liter$ of $1.5e-5$ molar Thionine solution is allowed to dry on bare-SiNPs. The average diameter and height of the SiNP used are $230nm$ and $400nm$ respectively ($pitch = 675nm$).

Raman spectrum of silicon. This means that bare SiNPs did not enhance the indicant optical field to the level required for generation of measurable Raman signal from the Thionine molecules. This is believed to be due to lack of plasmon resonance. The SiNPs used for this experiment had an average height of $400nm$ and average diameter of $230nm$ with a pitch of $675nm$.

5.5.2   Raman Enhancement By *Au* Nanodisks

As the starting point, we have studied the Raman enhancement provided by gold nanodisks over plain silicon. Numerous samples of *Au* nanodisks are fabricated and used as the substrate for Raman measurement. All nanodisks had a thickness of $25nm$ and were fabricated on plain silicon wafers by lift-off process (as described in chapter 2). Fig 5.23(a) shows the Raman spectrum of Thionine molecules coated on *Au* nanodisks. The first and largest peak is the characteristic peak of Thionine that occurs at $479cm^{-1}$ and the spectrum is similar to the typical Raman spectrum of Thionine. This figure includes the data for 7 sets of nanodisks with diameters ranging from $210nm$ to $440nm$. All samples Fig 5.23 have a pitch of $675nm$. Fig 5.23(b) shows how the magnitude of this peak varies as the diameter of the nanodisks changes.

We have also measured the Raman signal for very large nanodisks. The SEM image of Fig.5.23(c) shows the corresponding sample with the same pitch of $675nm$, where the nanodisks are almost touching each other. Some of the nanodisks do indeed blend with each-other but others illustrate tiny gaps which can in some cases be too small to be able to measure accurately. The resulting small gaps yield in considerably larger Raman signal as seen in Fig. 5.23(d).

5.5.3   Raman Enhancement: *Au* Layers Over SiNP

This section includes Raman spectrum obtained from SiNPs with *Au* layers on top. The SiNP makes the *Au* layers (plasmonic resonators) more exposed to molecules by elevating them. Additionally numerical simulations suggest that the field enhancement is improved in the presence of pillar. We have fabricated and studied SiNPs with one, two and four layers of gold stacked on top of them. All the *Au* layers are $25nm$-thick and any two subsequent *Au* layers are separated by $15nm$-thick layers of SiO_2. The height, diameter and pitch of the SiNPs are $400nm$, $230nm$ and $675nm$ respec-

(a)

(b)

(c)

(d)
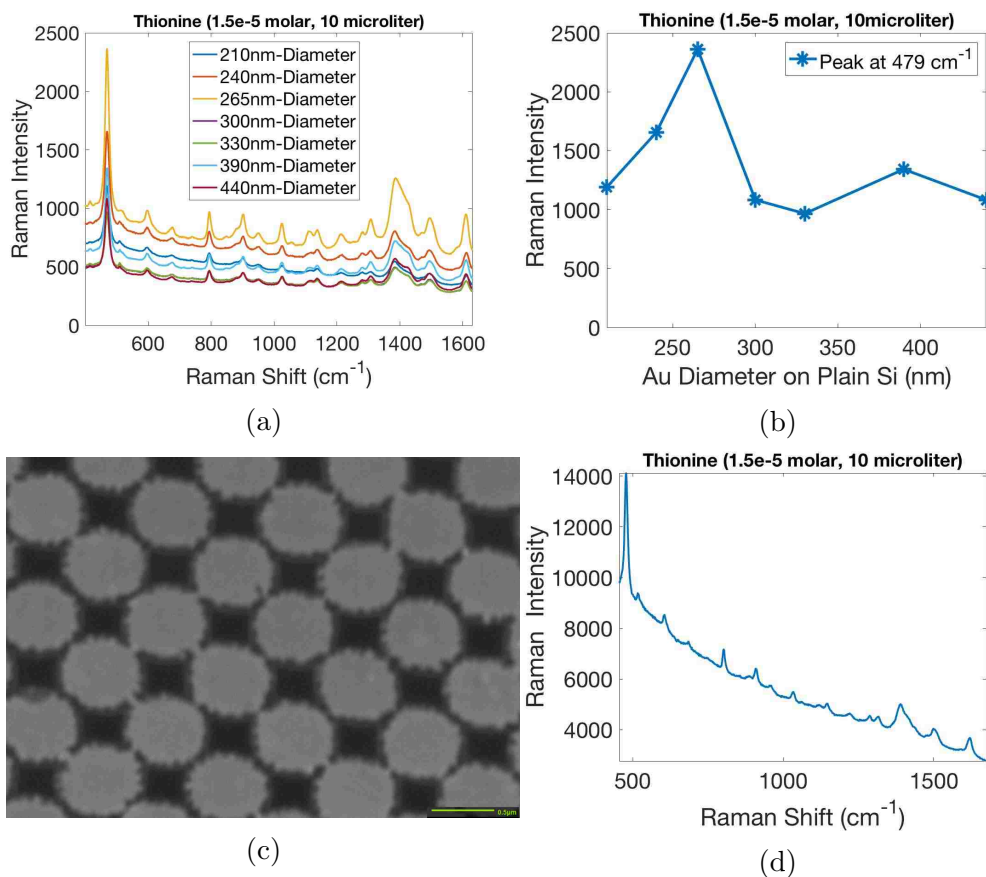
Figure 5.23: Raman spectrum of $10\mu liter$ of $2.5 * 10^{-5}$ molar Thionine on Au nanodisks. All samples have identical pitch of $675nm$. (a) Raman spectrum are compared for Au nanodisks with different diameters ranging from $210nm$ to $440nm$. (b) The peak intensities of the measured spectra are compared at $479cm^{-1}$ as a function of nanodisk-diameters (c) This micro-graph shows the case where the diameters of the Au nanodisks are much bigger, reducing the gap between the two nano-disks considerably. The Raman measurement using this sample is shown in (d) showing a considerable boost in Raman peaks which is due to very small distances of the plates

tively. Figures 5.24(a)-5.24(c) show the measured Raman signal of Thionine obtained using Au over SiNP, $Au/SiO_2/Au$ over SiNP and $Au/SiO_2/Au/SiO_2/Au/SiO_2/Au$ over SiNPs. The observed enhancement is also seen in simulations. In order to achieve this goal, a $4sec$ submersion in diluted buffer HF (0.4%) is used. Fig. 5.24(d) shows the obtain Raman signal. The experimental results obtained so far support
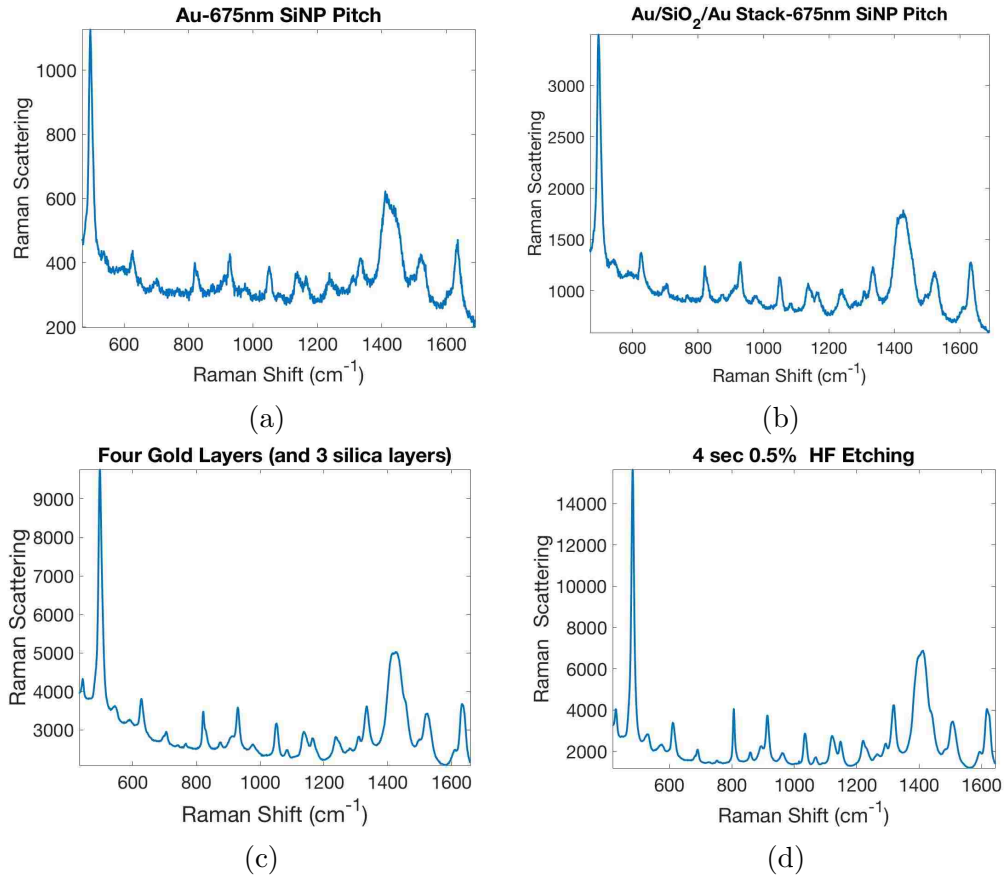
Figure 5.24: Raman signal of Thionine generated from different number of gold layers on top of SiNPs. The SiNPs are $400nm$ tall and have a diameter and pitch of $230nm$ and $675nm$ respectively. The Au layers are $25nm$ thick and are separated by $15nm$-thick layers of SiO_2. (a) A layer of Au over SiNP. (b) $Au/SiO_2/Au$-stack over SiNP. (c) $Au/SiO_2/Au/SiO_2/Au/SiO_2/Au$ stack over SiNP. (d) Raman using the sample of $Au/SiO_2/Au/SiO_2/Au/SiO_2/Au$-stack-over-SiNP, after etching the SiO_2 layers in 0.4% dilute buffer HF for $4sec.$ stacked

our numerical simulation results; the Raman signal increases as the number of gold layers increase and as expected by our simulations.

Effects of Nanopillar Material

Our simulation results also suggested considerable improvements by using silicon dioxide nanopillars as the base instead of SiNPs (see Fig. 5.12(b)). This triggered interest in experimental verification of these suggestions. However for fabrication purposes we decided to fabricate only a portion of the nanopillar from silicon dioxide. A nanopillar which is composed of $350nm$, SiO_2 nanopillar, deposited over $800nm$ SiNPs, is used as a platform for gold deposition. A $25nm$ layer of Au is deposited on top of this nanopillar and used to generate Raman from Thionine. The Raman signal measured is depicted in figure 5.25. Every peak in a Raman spectrum is related to a certain bond in the molecule used. Resolving more peaks can allow a better detection which is the ultimate goal of Raman.
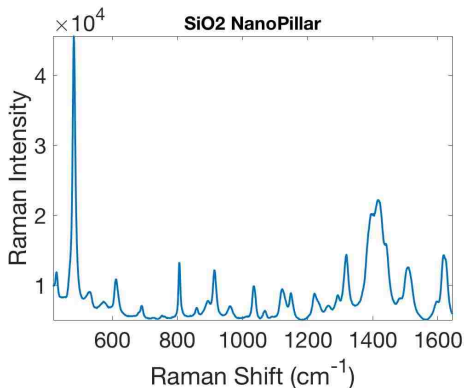
Figure 5.25: Considerable Raman enhancement in the Raman signal ($1.5e-5molar$, $10\mu liter$, Thionine) generated by Au over SiO_2 nanopillars

Effects of Nanopillar Height

The effects of SiNP-height over the overall performance of the Au over SiNP structures are studied using samples with varying SiNP heights ranging from $80nm$ to $400nm$. Fig 5.26 shows how the measured Raman signal is affected by the pillar

height. Fig. 5.26(b) plots the magnitude of the main peaks as a function of pillar height. The experimental results show that $240nm$ tall nanopillar substrates yield the largest Raman signal among the other heights tested. At this height the main peak and the smaller peaks are all larger than the other cases.

(a) (b)
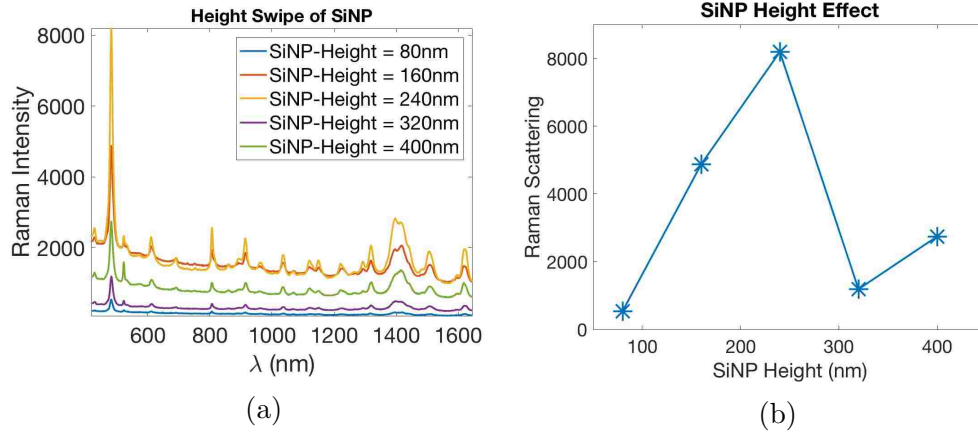
Figure 5.26: Raman spectrum of Thionine coated on Au-SiNPs with different heights (Au thickness =$25nm$). (a) Raman spectrum for different pillar heights ranging from $80nm$-$400nm$. (b) The magnitudes of the main peaks plotted as a function of pillar-height.

Effects of Reducing The Diameter

All the experimental Raman spectra reported so far were obtained using nanopillars with $230nm$ diameter. To examine the effect of having a very small pillar diameter a set of SiNPs are fabricated with diameter of $\sim50nm$ and a height of $290nm$. Fig. 5.27(a) shows the SEM image of these nanopillars. The Ni sample is removed before a $25nm$ layer of Au is deposited on the SiNPs. The measured Raman spectrum of Thionine is shown in Fig. 5.27(b). As seen in Fig. 5.27(a) the etching process has made the Si substrate, between the nanopillars, very rough and porous. The contribution of this rough surface makes the interpretation of the observed signal more difficult. In order to remove this background signal and obtain the spectrum of

Fig. 5.27(b) a silicon substrate was processed in an identical way as our sample but without the nanopillars. The Raman spectrum of this sample was used to eliminate the effect of the background (In Fig. 5.27(b) this background is already subtracted). As can be seen from the results of Fig. 5.27(b), reducing the diameter can consider-

(a)

(b)
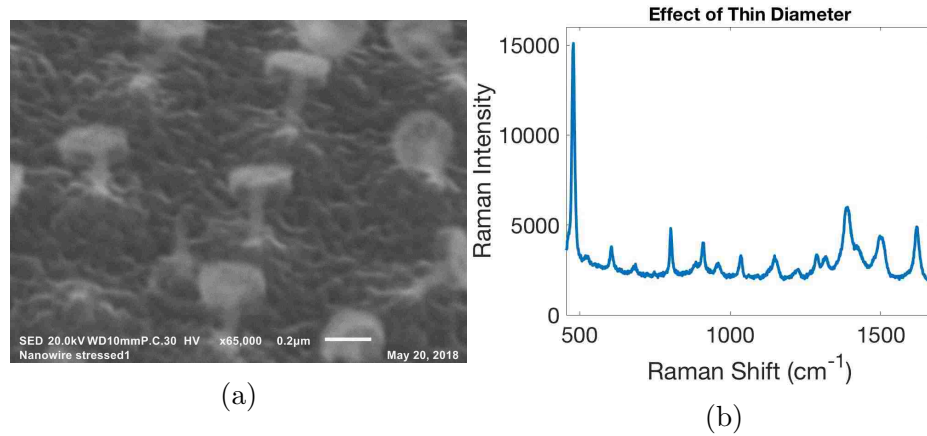
Figure 5.27: The Raman Enhancement from sub 100nm diameter nanopillars (a) SEM showing $50nm$ diameter of SiNP ($290nm$ height) holding the big nickel plate right after thinning the originally $230nm$ diameter nanopillars to $50nm$. (b) Raman enhancement of Au disks over nanopillars after removal of nickel and deposition of $25nm$ gold.

ably increase the Raman signal. The sample reported in this figure has only one layer of gold deposited on top of SiNP but the spectrum measured is comparable with the spectrum in Fig.5.24(c) which was obtained using a $Au/SiO_2/Au$-stack over SiNP but with a diameter of $230nm$.

A comparison of the results showing the effect of stacking and side etching of silica on the Raman spectrum of $10\mu liter$ Thionine (at $479cm^{-1}$) with density of $1.5*10^{-5}$is shown at table 5.2. The gold disks of the stacks are separated by $SiO_2 : 15nm$.

Table 5.2: **Measured peak Raman intensity for various designs**

Number of Disks over SiNP *	Peak Raman intensity at $479cm^{-1}$
$0 - Au$ layer on SiNP	-
$1 - Au$ layer on SiNP	1130
$2 - Au$** layer on SiNP	3500
$4 - Au$** layer on SiNP	9770
$4 - Au$** layer on SiNP, with silica side etching	15660
*: SiNP height and diameter is $400nm, 230nm$	
** : The gold disks of the stacks are separated by $SiO_2 : 15nm$.	

In conclusion we have investigated the effect of stacking of Au layers and side etching of silica on Raman enhancement. We have also observed the effect of changing the pillar height, reducing SiNP diameter, and Changing the material of silicon nanopillar (to silica NP), all with a single Au layer on top. The Raman enhancement for these experiments are as follows:

- Raman enhancement for $Au/SiNP$ ($diameter/height = 230nm/270nm$): 8190

- Raman enhancement for $Au/SiO_2 - NP$ ($diameter/height = 230nm/350nm$): 48170

- Raman enhancement for $Au/SiNP$ ($diameter/height = 50nm/290nm$): 15100

It should be noted that for SiO_2-NP is deposited by E-beam over 800nm SiNP.

5.5.4 Transition of Methylene Blue to Thionine (Spectral Transition of The Raman Signal)

The Raman signal generated from molecules over plasmonic nanostructures (metallic nano structures made from Au,Ag,Cu and even Ni) can increase significantly due to E-field enhancement (proportional to E^4). Additionally for certain molecules the

large field enhancement combined with interaction with free electrons in metal can result in chemical transitions and therefore evolution of the Raman spectrum. Here we study the transitions of Methylene Blue (MB) to Thionine in the vicinity of SiNPs with Au, Au/SiO_2 and $Au/SiO_2/Au$ caps. The SiNPs, all have diameters of $230nm$ and height of $400nm$. The nanostructures used are separated as far as $2.1\mu m$ from each-other. Such large distances make it experimentally possible to record the effects of a single nano-disk or nano-stack. The considerable field enhancement obtained using MIM can potentially lead to chemical transition of the target molecule (as it happens for MB in our measurements). Since a major effort of this dissertation was to enhance Raman through field enhancement, it is important to investigate the effect of excessive field enhancement on the stability of the target molecule . In particular for sensing applications this is an undesired effect as it does not allow for clear identification of a molecular finger print (a specific Raman spectrum).
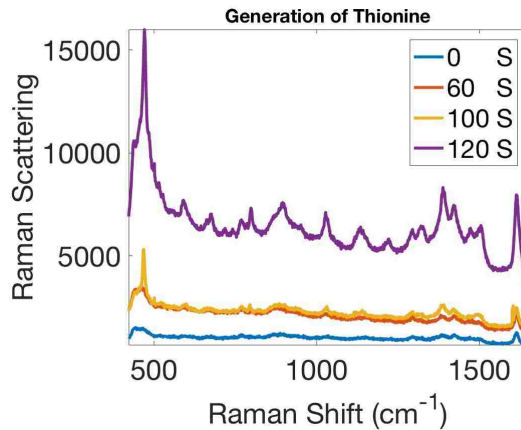
Figure 5.28: Time evolution of MB Raman scattering, obtained using SiNPs topped with $Au/SiO_2/Au$. The spectrum are obtained after different exposure duration to $633nm$ He-Ne laser with a power of $939nW/\mu m^2$.

Fig. 5.28 shows the Raman spectra of MB over a SiNP which is topped with $Au/SiO_2/Au$ stack. This figure shows four different spectra recorded after different exposure durations. Comparing the four different spectra it can bee seen how Methy-

lene Blue is converted to Thionine overtime. Similar phenomena have been reported by other groups for different structures as well and have been reported to be due plasmons turning into hot electrons [123]. Hot electrons are high energy electrons that can initiate the decomposition of MB to Thionine.
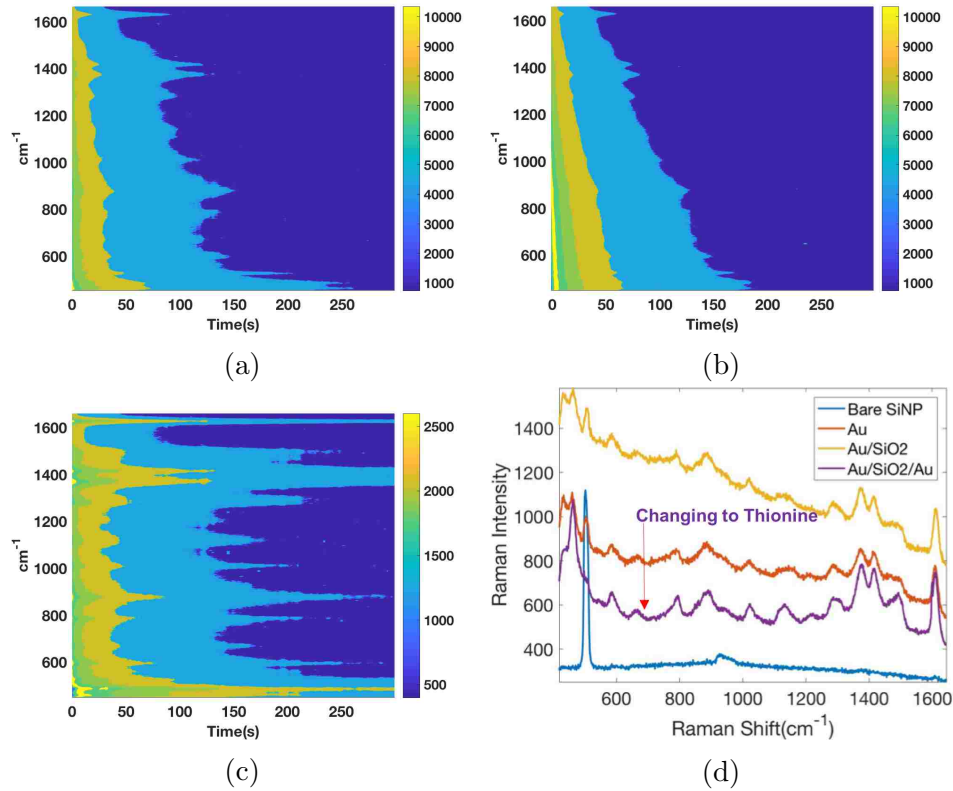
Figure 5.29: Raman scattering of MB as a function of time for a period of 5 minuets. The $632.8nm$ laser light power used was $939nW/\mu m^2$. The data are recorded from MB coated on (a) Au (b) Au/SiO_2 (c) $Au/SiO_2/Au$ -capped SiNPs. (d) The Raman intensity of different structures compared at the end of $5min$ time-line. The Raman intensity curve for $Au/SiO_2/Au$ over SiNP shows emerging Thionine molecule resulted from demethylation of MB.

To further investigate sample stability during Raman spectroscopy and the effects of structures used, we have obtained the Raman emissions of Methylene Blue (MB) using different nanostructures. These data are shown in Fig. 5.29. Each plot of this figure summarizes the results of 1500 measurements. Each plot is composed

of 150 spectra obtained at different times. Each spectra is the average of 10 different measurements obtained from 10 different points. Except some changes in the amplitudes, no changes in the locations of the characteristics peaks are observed in Figs. 5.29(a) & 5.29(b). On the other hand, figure 5.29(c) shows significant peaks at $479cm-1$ and $1621cm^{-1}$ which are characteristics of Thionine. Since there was no initial Thionine, the existence of these peaks can only mean conversion of MB to Thionine in presences of red light and plasmons which generate hot electrons. These hot electrons are high energy electrons that are not coupled to light.

It has been shown that in presence of surface plasmon and red laser, MB decomposes to Thionine by demethylation [123]. The results of Fig. 5.29(d) indicate that demethylation happens only in the $Au/SiO_2/Au$ case. The simulations carried out on the effects of using more than one metallic layer suggested considerable field enhancement by $Au/SiO_2/Au$-SiNP (see Fig.5.24(c)). Thus we can attribute the difference between the behavior of MB, to the different field intensities. The intense field in the $Au/SiO_2/Au$, can be considered responsible for generation of hot electrons and MB degradation. The fact that demethylation doesn't happen immediately, means this process needs a certain amount of absorbed energy to proceed.

Fig. 5.30 confirms that SiNP topped with Au are not capable of initiating demethylation process even after 60 minutes of exposure (at the same light intensity). None of the characteristic peaks of the Thionine are observed even after such a long exposure time. However careful observation of the the results presented in Fig. 5.30 reveals that although the peaks detected don't change, their amplitude does. Over time the overall signal reduces in amplitude. This is due to decomposition of MB in presence of oxygen and is not our focus.

During our experiments we have observed that, when the light intensity is high, even a stable molecule's Raman signal (such as Thionine) degrades fast. Our laser is a $633nm$ HeNe laser. Focusing the light over the sample, rapidly degrades the signal
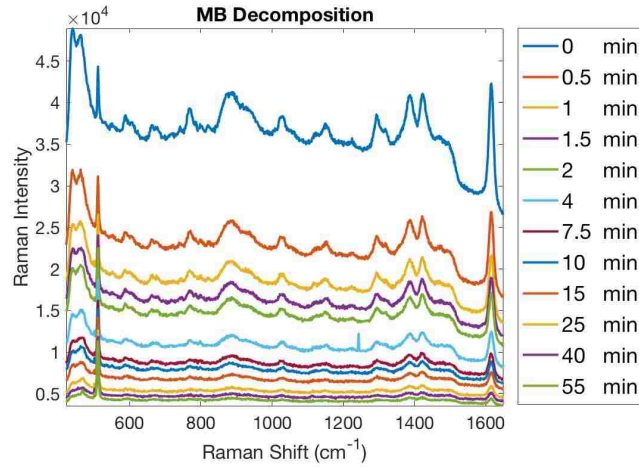
Figure 5.30: Raman scattering of MB over Au-topped SiNP are studied during a $60 minute$ period.

intensity. Therefore, for having a reasonable span of time to reliably measure the Raman spectra we have defocused the beam to cover an area of roughly $1600 \mu m^2$.

5.6 Raman Enhancement With Non-Metallic Stacks on SiNP

So far this chapter was devoted to understanding field enhancement, scattering cross-section and Raman scattering. Special effort was put into limiting the samples used to SiNPs and SiNPs topped with one or more Au layers and stay away from other materials. This allowed an in depth study of the effects of different parameters. However we have also explored the possibility of using non-metallic plasmonic resonators (non-metals with significant negative permittivity). Not only this has yielded considerable results but it also has opened the door to a vast research area which deserves an in depth study by other researchers. However it is important to mention that to the

best of our knowledge, some of the phenomena observed in this section have not yet been completely understood and thus we will inevitably, frequently, refer to claims made by other researchers to partially explain some of these phenomena/results.

This section will include experimental results obtained using Ge, TiN, as well as Au, $Au/SiO_2/Au$, Ag, Cu and super thin Au layers on SiNPs.

5.6.1 Ge as The Non-Metallic Thin-Film

Two samples have been prepared by depositing $25nm$ Ge on SiNP arrays ($400nm$ tall, 230 in diameter). One of the samples is kept as as but the other one is treated with a NH_3 plasma. The treatment is done using $60W$, $500mTor$, NH_3 plasma with a flow rate of $30sccm$, for a duration of 5 minutes, at 180^{oC}. During this process no significant nitridation will happen for Ge [14], but it will get hydrogenated [29]. The resulting structures are used for surface enhanced Raman spectroscopy of a $10\mu Liter$ sample of $1.5 * 10^{-5}M$, MB solution. Fig 5.31 shows the SERS spectrum obtained using these devices. Figs. 5.31(a) and 5.31(b) shows the spectrum obtained by the "as-fabricated" and plasma treated samples. As can be seen from these spectra, the as-fabricated sample doesn't show any noticeable enhancement but the plasma treated sample is capable of significant SERS generation.

Untreated Ge is not capable of any detectable SERS. Two main reasons for this are its positive permittivity and amorphous structure. Ge does has a considerably large positive permittivity. Technically the (dark-)conductivity of Ge can not be increased very much since Ge can not be doped more than $10^{20}cm^{-3}$ (although some other materials like oxides have been reported to have higher dopant solubility as high as $10^{21}cm^{-3}$ [100]). Achieving negative permittivity in Ge would require a much higher doping than practically possible [100]. The other fact that prevents untreated-Ge from producing Raman is its amorphous structure which results in low carrier
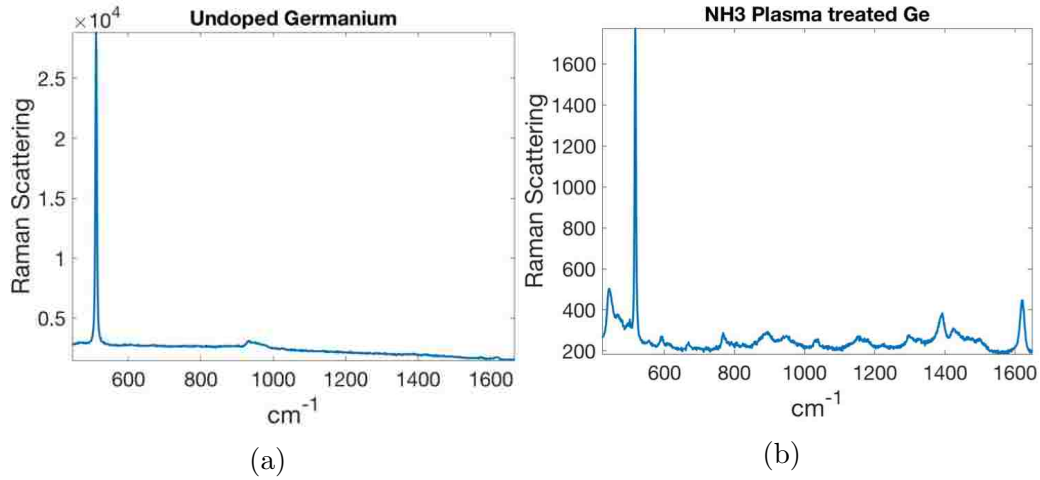
Figure 5.31: Raman signal obtained from MB using $25nm$ layer of Ge over SiNP. (a) No enhancement was observed. The peak at $520cm^-1$ belongs to the Si substrate and is not an indication of Raman enhancement. (b) The Raman signal using the same sample after an NH_3 plasma treatment was performed on it.

mobility. Germanium is a semiconductor thus it has much less conduction electrons to couple with the light and generate plasmon polaritons compared to metals.

Fig. 5.32 show the measured permittivity of the Sample after being treated with NH_3 plasma. The observe negative permittivity explains the reason why the sample was capable of considerable Raman enhancement after being treated with NH_3 plasma.

5.6.2 TiN as The Non-Metallic Thin-Film

The procedure of Sec 5.6.1 is repeated here with the only difference being that instead of GE, TiN is deposited over SiNP. The thickness of the TiN layer is $30nm$. Fig. 5.33 compares the SERS spectrum of MB obtained using TiN-topped-SiNPs as well as TiN-topped-SiNPs which were treated with NH_3 plasma. The results of Fig. 5.33 shows that just like Ge, treating TiN with NH_3 plasma considerably increases its

(a)

(b)
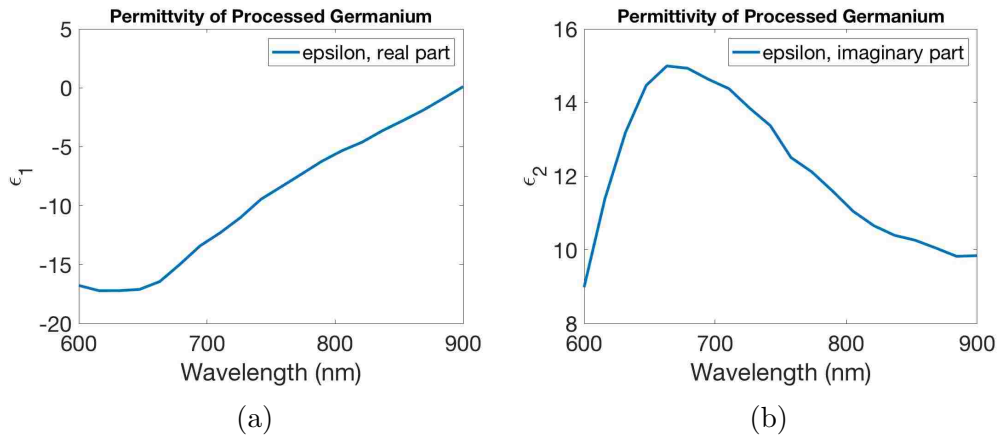
Figure 5.32: Permittivity of Germanium treated with NH_3 plasma at 180^{oC} (a) real part of epsilon which is negative at our Raman and laser wavelength range more negative than Nickel at $633nm$ of our laser wavelength [60](b) imaginary part of epsilon which is comparable to metals like Chromium and nickel at $633nm$. [60].

(a)

(b)
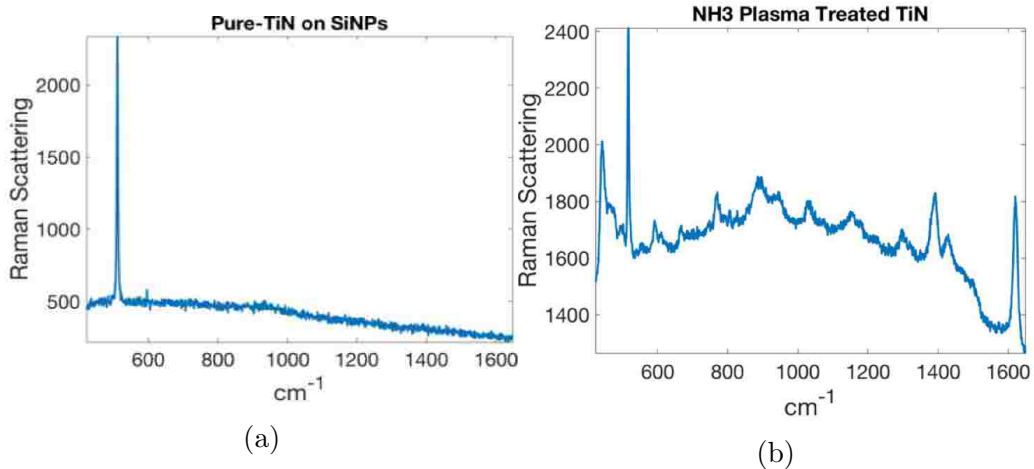
Figure 5.33: SERS of RhB obtained by (a) TiN over SiNPs (b) NH_3-plasma-treated TiN over SiNPs. Raman enhancement is achieved only in the plasma treated sample. The SiNPs were $400nm$ tall and $230nm$ in diameter. The TiN layer is $30nm$ thick

performance. Untreated TiN exhibits no Raman enhancement but when treated with a NH_3 plasma, considerable Raman signal enhancement is observed.

5.7 Impact of Metal Properties and Surface Roughness on Raman Signal: A Study with Au, Ag and Cu Nanodisks on SiNPs

The SiNPs used are $400nm$ tall and $230nm$ in diameter. The samples that will be presented here are Au, Ag, Cu and Au/Cr_2O_3 over SiNPs. All the metallic layers used in this section are $25nm$ thick. Fig. 5.34 shows the SERS spectrum of
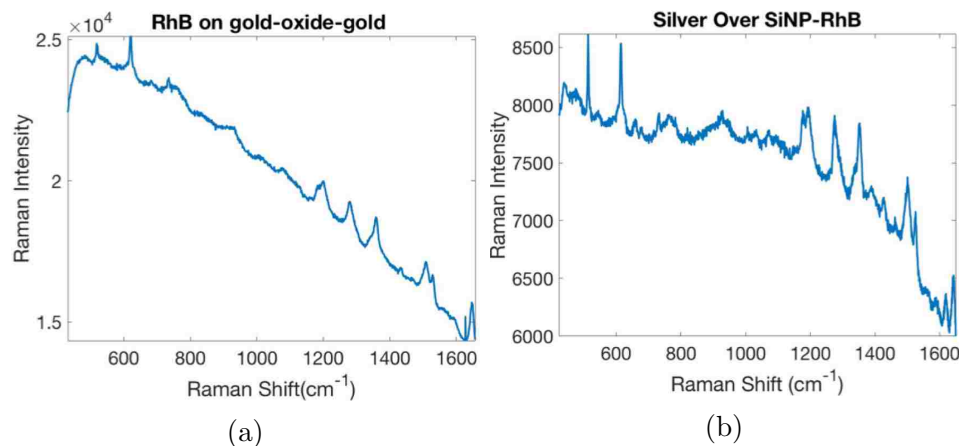
Figure 5.34: The Raman spectrum of RhB obtained by SiNPs topped with (a) $Au/SiO_2/Au$-stack and (b) Ag thin-film. The SiNPs are $400nm$ tall and $230nm$ in diameter. The thickness of Au, Ag and SiO_2 layers are $25nm$, $25nm$ and $15nm$ respectively.

RhB obtained using Ag and Au deposited on top of SiNPs. Both spectrum show the characteristics Raman peaks of RhB (see Fig. 5.36(c)). However the spectrum don't have a flat baseline. This is due to radiation of the metal nanodisks. We call this none-flat baseline the "background" and it is different for different materials. Theoretically one can try to identify and eliminate them but that is not the scope of the work here. Our goal in here is to prevent radiation to begin with. For this end, we have tried different combinations of the materials and processing techniques.
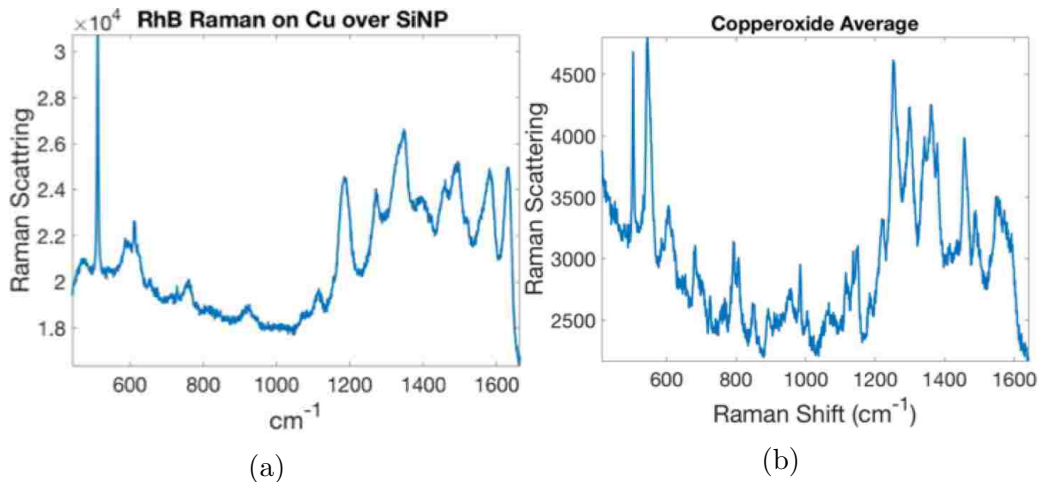
Figure 5.35: The Raman spectrum of RhB obtained by SiNPs topped with (a) Au (b) Cu. The SiNPs are $400nm$ tall and $230nm$ in diameter. The thicknesses of Au, Ag, and Cu are $25nm$, $25nm$, and $25nm$ respectively.

Replacing the Au on top SiNPs with with a $25nm$ layer of Ag yields in much easier to distinguish Raman peaks but cover noise (antenna radiation) remains as a considerable issue still. None of our samples using Ag was able to solve this problem.

Fig. 5.35 shows the SERS spectrum of RhB obtained using copper and copper oxide over SiNPs. These two spectrum represent considerable improvement in minimizing background. Oxidation of copper has been achieved by a 10-second oxygen plasma ($60Watts$ at $200mTorr$). The observed shifts in the location of the peaks, seen both in Fig. 5.35(a) and 5.35(b) are due to chemical phenomena and need quantum mechanical analysis which is not a part of our work.[67]. Despite the observed improvements, the shift in the location of the peaks makes it super difficult to associate different peaks to their corresponding bonds.

The sample used for obtaining the SERS of Fig. 5.36 illustrate considerably flat baseline. All the characteristic Raman peaks (see Fig. 5.36(c)) of RhB are at the expected locations and are considerably enhanced. This is achieved by using a super thin layer of Au over SiNP. The SiNPs are fabricated using a Cr_2O_3 Mask which

(a)

(b)

(c)
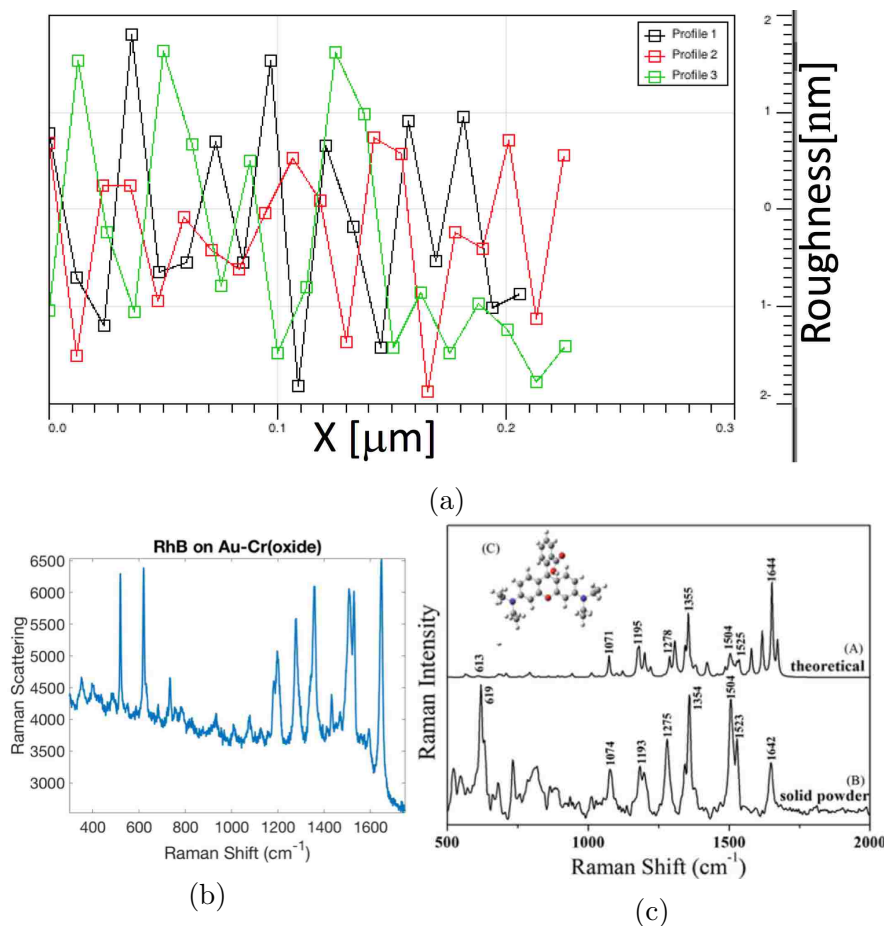
Figure 5.36: Comparison between SERS of RhB obtained here with the typical RhB Raman spectrum available in literature. (a) AFM graph of the roughness of Si surface after using Cr etchant. (b) RhB SERS by a thin layer of gold($4.5nm$) over $30nm$ chromium oxide on $SiNP$. The SiNP was $400nm$ tall and 230 in diameter. (c) The reference RhB powder Raman spectra[88]

need to be removed before gold is deposited. This process renders the surface of the nanopillar rough as can be seen in Fig. 5.36(a). The thickness of the Au layer deposited is $4.5nm$ which is comparable with the surface roughness of the SiNP. The rough Au layer on SiNPs thus experimentally proves to be an ideal method to achieve highly desirable Raman enhancement using MIM-stacks on SiNPs.

5.8 Conclusion

The applications of nanostructures in Raman enhancement are studied in this chapter. Field enhancement, scattering cross-section and Raman enhancement of metallic nanodisks and SiNPs as well as nanodisks on SiNPs are investigated. The effects of different geometric parameters on the field enhancement of the nanostructures are studied. Some of the experimental results obtained, didn't completely agree with the numerical simulations, mainly because the beam of light used in experimental measurements is not a collimated one. The effect of SiNPs on field enhancement of the Au or $Au/SiO_2/Au$ layers on top of them was studied.

Coupling of the stacks was also shown to yield considerable field enhancement. As a result, the Raman signal increased nonlinearly as we moved from one Au-over-SiNP to $Au/SiO_2/Au$-over-SiNP and $Au/SiO_2/Au/SiO_2/Au/SiO_2/Au$-over-SiNP. The coupling is proven both numerically and experimentally. However field enhancement came with the cost of sample specimen degradation due to strong fields formed at the edges. Our experiment and simulation suggests that side etching the silica of the stacks increases the touching surface of edges and molecules, increasing Raman without the cost imposed by field enhancement.

Although the metallic layers used were mainly made of gold, different other metallic and even non-metallic materials were also explored. It was observed that plasma treatment of Ge and TiN changes their plasmonic performance considerably, yielding negative permittivity (for germanium only) and considerable Raman enhancement for both. The optical permittivity of processed Germanium was superior to that of Nickel at wavelengths from $600nm$ to $700nm$. It was also observed that surface roughness of the substrate just below the metallic layer has considerable effect on removing background noise in the recorded Raman signal. Our experimental results showed that when the top surface of a SiNP is roughened before Au deposition (a

roughens of $3nm$), a super-thin ($5nm$) layer of gold deposited on the SiNPs ($400nm$ tall and $230nm$ in diameter), is capable of yielding considerable Raman enhancement with distinct peaks which match with the characteristic spectrum of the RhB powder, and no noticeable background noise. This sample outperformed a stack of $Au/SiO_2/Au : 25nm/15nm/25nm$, both in amplitude and quality of the obtained Raman spectrum.

References

[1] *Ir measurement-nist.gov*, `http://webbook.nist.gov/chemistry`, Accessed: 2010-09-30.

[2] *Ir measurement-thermofisher*, `https://www.thermofisher.com/us/en/home/industrial/spectroscopy-elemental-isotope-analysis/`, Accessed: 2010-09-30.

[3] Mamdouh E Abdelsalam, Philip N Bartlett, Jeremy J Baumberg, Suzanne Cintra, Tim A Kelf, and Andrea E Russell, *Electrochemical sers at a structured gold surface*, Electrochemistry Communications **7** (2005), no. 7, 740–744.

[4] Nahla A Abu Hatab, Jenny M Oran, and Michael J Sepaniak, *Surface-enhanced raman spectroscopy substrates created via electron beam lithography and nanotransfer printing*, ACS nano **2** (2008), no. 2, 377–385.

[5] Nisha Ahlawat, *Raman spectroscopy: A review*, Int. J. Comput. Sci. Mob. Comput **3** (2014), no. 11, 680–685.

[6] Hyo-Jin Ahn, Pradheep Thiyagarajan, Lin Jia, Sun-I Kim, Jong-Chul Yoon, Edwin L Thomas, and Ji-Hyun Jang, *An optimal substrate design for sers: dual-scale diamond-shaped gold nano-structures fabricated via interference lithography*, Nanoscale **5** (2013), no. 5, 1836–1842.

[7] Ceyhun Akcay, Pascale Parrein, and Jannick P Rolland, *Estimation of longitudinal resolution in optical coherence imaging*, Applied Optics **41** (2002), no. 25, 5256–5262.

[8] Seyedhamidreza Alaie, Mani Hossein-Zadeh, Mohammadhosein Ghasemi Baboly, Mohammadreza Zamani, and Zayd Chad Leseman, *Enhancing mechanical quality factors of micro-toroidal optomechanical resonators using phononic crystals*, Journal of Microelectromechanical Systems **25** (2016), no. 2, 311–319.

References

[9] Kenneth W Allen, Joshua M Duran, Gamini Ariyawansa, Jarrett H Vella, Nicholaos I Limberopoulos, Augustine M Urbas, and Vasily N Astratov, *Photonic jets for strained-layer superlattice infrared photodetector enhancement*, Aerospace and Electronics Conference, NAECON 2014-IEEE National, IEEE, 2014, pp. 32–33.

[10] Erik Hyde Anderson, *Fabrication and electromagnetic applications of periodic nanostructures*, Ph.D. thesis, Massachusetts Institute of Technology, 1988.

[11] Gustavo FS Andrade, MeiKun Fan, and Alexandre G Brolo, *Multilayer silver nanoparticles-modified optical fiber tip for high performance sers remote sensing*, Biosensors and Bioelectronics **25** (2010), no. 10, 2270–2275.

[12] Khalid Askar, Blayne M Phillips, Yin Fang, Baeck Choi, Numan Gozubenli, Peng Jiang, and Bin Jiang, *Self-assembled self-cleaning broadband antireflection coatings*, Colloids and Surfaces A: Physicochemical and Engineering Aspects **439** (2013), 84–100.

[13] Mark A Atwater, Arash K Mousavi, Zayd C Leseman, and Jonathan Phillips, *Direct synthesis and characterization of a nonwoven structure comprised of carbon nanofibers*, Carbon **57** (2013), 363–370.

[14] D Aubel, M Diani, L Kubler, JL Bischoff, and D Bolmont, *Selective thermal – as opposed to non-selective plasma-nitridation of sige related materials examined by in situ photoemission techniques*, Journal of non-crystalline solids **187** (1995), 319–323.

[15] Byeong-Ju Bae, Sung-Hoon Hong, Eun-Ju Hong, Heon Lee, and Gun-young Jung, *Fabrication of moth-eye structure on glass by ultraviolet imprinting process with polymer template*, Japanese Journal of Applied Physics **48** (2009), no. 1R, 010207.

[16] Kui Bao, Xiang Ning Kang, Bei Zhang, Tao Dai, Chang Xiong, Hang Ji, Guo Yi Zhang, and Yong Chen, *Improvement of light extraction from patterned polymer encapsulated gan-based flip-chip light-emitting diodes by imprinting*, IEEE Photonics Technology Letters **19** (2007), no. 22, 1840–1842.

[17] Jeremy J Baumberg, Timothy A Kelf, Yoshihiro Sugawara, Suzanne Cintra, Mamdouh E Abdelsalam, Phillip N Bartlett, and Andrea E Russell, *Angle-resolved surface-enhanced raman scattering on metallic nanostructured plasmonic crystals*, Nano letters **5** (2005), no. 11, 2262–2267.

[18] A Bett, J Eisenlohr, O Höhn, B Bläsi, J Benick, P Repo, H Savin, JC Goldschmidt, and M Hermle, *Front side antireflection concepts for silicon solar cells*

References

with diffractive rear side structures, 29th European Photovoltaic Solar Energy Conference and Exhibition, 2014, pp. 987–991.

[19] D Bouhafs, A Moussi, A Chikouche, and JM Ruiz, *Design and simulation of antireflection coating systems for optoelectronic devices: Application to silicon solar cells*, Solar Energy Materials and Solar Cells **52** (1998), no. 1-2, 79–93.

[20] Darryl A Boyd, Jesse A Frantz, Shyam S Bayya, Lynda E Busse, Woohong Kim, Ishwar Aggarwal, Menelaos Poutous, and Jasbinder S Sanghera, *Modification of nanostructured fused silica for use as superhydrophobic, ir-transmissive, anti-reflective surfaces*, Optical Materials **54** (2016), 195–199.

[21] Alexandre G Brolo, Erin Arctander, Reuven Gordon, Brian Leathem, and Karen L Kavanagh, *Nanohole-enhanced raman scattering*, Nano Letters **4** (2004), no. 10, 2015–2018.

[22] Claudia Brückner, Boris Pradarutti, Olaf Stenzel, Ralf Steinkopf, Stefan Riehemann, Gunther Notni, and Andreas Tünnermann, *Broadband antireflective surface-relief structure for thz optics*, Optics express **15** (2007), no. 3, 779–789.

[23] J Buencuerpo, L Torné, R Álvaro, JM Llorens, ML Dotor, and JM Ripalda, *Nano-cones for broadband light coupling to high index substrates*, Scientific reports **6** (2016), 38682.

[24] Martín Caldarola, Pablo Albella, Emiliano Cortés, Mohsen Rahmani, Tyler Roschuk, Gustavo Grinblat, Rupert F Oulton, Andrea V Bragas, and Stefan A Maier, *Non-plasmonic nanoantennas for surface enhanced spectroscopies with ultra-low heat conversion*, Nature communications **6** (2015), 7915.

[25] Joshua D Caldwell, Orest Glembocki, Francisco J Bezares, Nabil D Bassim, Ronald W Rendell, Mariya Feygelson, Maraizu Ukaegbu, Richard Kasica, Loretta Shirey, and Charles Hosten, *Plasmonic nanopillar arrays for large-area, high-enhancement surface-enhanced raman scattering sensors*, ACS nano **5** (2011), no. 5, 4046–4055.

[26] Joshua D Caldwell, Orest J Glembocki, Francisco J Bezares, Maarit I Kariniemi, Jaakko T Niinistö, Timo T Hatanpää, Ronald W Rendell, Maraizu Ukaegbu, Mikko K Ritala, Sharka M Prokes, et al., *Large-area plasmonic hot-spot arrays: sub-2 nm interparticle separations with plasma-enhanced atomic layer deposition of ag on periodic arrays of si nanopillars*, Optics express **19** (2011), no. 27, 26056–26064.

References

[27] Linyou Cao, Bahram Nabet, and Jonathan E Spanier, *Enhanced raman scattering from individual semiconductor nanocones and nanowires*, Physical review letters **96** (2006), no. 15, 157402.

[28] S Cao, W Yu, T Wang, Z Xu, C Wang, Y Fu, and Y Liu, *Two-dimensional subwavelength meta-nanopillar array for efficient visible light absorption*, Applied Physics Letters **102** (2013), no. 16, 161109.

[29] I Chambouleyron and R Campomanes, *Ammonia as an active doping source gas of hydrogenated amorphous germanium films*, Physical Review B **53** (1996), no. 19, 12566.

[30] Yun-Chorng Chang, Shih-Ming Wang, Hsin-Chan Chung, Chung-Bin Tseng, and Shih-Hui Chang, *Observation of absorption-dominated bonding dark plasmon mode from metal–insulator–metal nanodisk arrays fabricated by nanospherical-lens lithography*, ACS nano **6** (2012), no. 4, 3390–3396.

[31] RS Chao, RK Khanna, and ER Lippincott, *Theoretical and experimental resonance raman intensities for the manganate ion*, Journal of Raman Spectroscopy **3** (1975), no. 2-3, 121–131.

[32] Dinguo Chen, *Anti-reflection (ar) coatings made by sol–gel processes: a review*, Solar Energy Materials and Solar Cells **68** (2001), no. 3, 313–336.

[33] HL Chen, SY Chuang, CH Lin, and YH Lin, *Using colloidal lithography to fabricate and optimize sub-wavelength pyramidal and honeycomb structures in solar cells*, Optics Express **15** (2007), no. 22, 14793–14803.

[34] Zhizhang Chen, Peyman Sana, Jalal Salami, and Ajeet Rohatgi, *A novel and effective pecvd sio/sub 2//sin antireflection coating for si solar cells*, IEEE Transactions on Electron Devices **40** (1993), no. 6, 1161–1165.

[35] Sameer Chhajed, Martin F Schubert, Jong Kyu Kim, and E Fred Schubert, *Nanostructured multilayer graded-index antireflection coating for si solar cells with broadband and omnidirectional characteristics*, Applied Physics Letters **93** (2008), no. 25, 251108.

[36] _____, *Nanostructured multilayer graded-index antireflection coating for si solar cells with broadband and omnidirectional characteristics*, Applied Physics Letters **93** (2008), no. 25, 251108.

[37] CH Chiu, Peichen Yu, HC Kuo, CC Chen, TC Lu, SC Wang, SH Hsu, YJ Cheng, and YC Chang, *Broadband and omnidirectional antireflection employing disordered gan nanopillars*, Optics express **16** (2008), no. 12, 8748–8754.

References

[38] WS Choi, SSA Seo, KW Kim, TW Noh, MY Kim, and S Shin, *Dielectric constants of ir, ru, pt, and iro 2: Contributions from bound charges*, Physical Review B **74** (2006), no. 20, 205117.

[39] John W Coburn and Harold F Winters, *Plasma etching—a discussion of mechanisms*, Journal of vacuum Science and Technology **16** (1979), no. 2, 391–403.

[40] JW Coburn, Harold F Winters, and T␣J␣ Chuang, *Ion-surface interactions in plasma etching*, Journal of Applied Physics **48** (1977), no. 8, 3532–3540.

[41] C David, P Häberling, M Schnieper, J Söchtig, and C Zschokke, *Nanostructured anti-reflective surfaces replicated by hot embossing*, Microelectronic Engineering **61** (2002), 435–440.

[42] Viktor Nikolaevič Denisov, Boris Nikolajevič Mavrin, and Vâčeslav Borisovič Podobedov, *Hyper-raman scattering by vibrational excitations in crystals, glasses and liquids*, Physics reports **151** (1987), no. 1, 1–92.

[43] Nibir K Dllllr, Dennis L PolI, and Priyalal Wijewarnasuriya, *Nanostructured antireflection (ar) coatings for optoelectronic applications*, Comprehensive Guide for Nanocoatings Technology (Mahmood Aliofkhazraei, ed.), vol. 4, Nova Science Publishers, Inc.

[44] Gary L Dorer and Valdis Mikelsons, *Microstructured transmission and reflectance modifying coating*, February 26 1980, US Patent 4,190,321.

[45] Ying Du, Shijie Liu, Hongbo He, Yunxia Jin, Fanyu Kong, and Heyuan Guan, *Laser-induced damage properties of antireflective porous glasses*, Optics Communications **285** (2012), no. 24, 5512–5518.

[46] Gisela Eckhardt, RW Hellwarth, FJ McClung, SE Schwarz, D Weiner, and EJ Woodbury, *Stimulated raman scattering from organic liquids*, Physical Review Letters **9** (1962), no. 11, 455.

[47] Maj Frederiksen, Vladimir E Bochenkov, Ryosuke Ogaki, and Duncan S Sutherland, *Onset of bonding plasmon hybridization preceded by gap modes in dielectric splitting of metal disks*, Nano letters **13** (2013), no. 12, 6033–6039.

[48] Bradley J Frey, Douglas B Leviton, and Timothy J Madison, *Temperature-dependent refractive index of silicon and germanium*, SPIE Astronomical Telescopes+ Instrumentation, International Society for Optics and Photonics, 2006, pp. 62732J–62732J.

[49] Neal A Hall, *Electrostatic mems microphones*, Encyclopedia of Nanotechnology, Springer, 2012, pp. 775–783.

References

[50] Katherine Han and Chih-Hung Chang, *Numerical modeling of sub-wavelength anti-reflective structures for solar module applications*, Nanomaterials **4** (2014), no. 1, 87–128.

[51] Christy L Haynes and Richard P Van Duyne, *Nanosphere lithography: a versatile nanofabrication tool for studies of size-dependent nanoparticle optics*, 2001.

[52] LJ Heyderman, H Schift, C David, J Gobrecht, and T Schweizer, *Flow behaviour of thin polymer films used for hot embossing lithography*, Microelectronic Engineering **54** (2000), no. 3-4, 229–245.

[53] Douglas S Hobbs and Bruce D MacLeod, *High laser damage threshold surface relief micro-structures for anti-reflection applications*, Laser-Induced Damage in Optical Materials: 2007, vol. 6720, International Society for Optics and Photonics, 2005, p. 67200L.

[54] ———, *Design, fabrication, and measured performance of anti-reflecting surface textures in infrared transmitting materials*, Laser-Induced Damage in Optical Materials: 2005, vol. 6720, International Society for Optics and Photonics, 2007, p. 67200L.

[55] Douglas S Hobbs, Bruce D MacLeod, and Ernest Sabatino, *Continued advancement of laser damage resistant optically functional microstructures*, Laser-Induced Damage in Optical Materials: 2012, vol. 8530, International Society for Optics and Photonics, 2012, p. 85300O.

[56] Yi-Fan Huang, Surojit Chattopadhyay, Yi-Jun Jen, Cheng-Yu Peng, Tze-An Liu, Yu-Kuei Hsu, Ci-Ling Pan, Hung-Chun Lo, Chih-Hsun Hsu, Yuan-Huei Chang, et al., *Improved broadband and quasi-omnidirectional anti-reflection properties with biomimetic silicon nanostructures*, Nature nanotechnology **2** (2007), no. 12, 770–774.

[57] Yun Suk Huh, Aram J Chung, Bernardo Cordovez, and David Erickson, *Enhanced on-chip sers based biomolecular detection using electrokinetically active microwells*, Lab on a Chip **9** (2009), no. 3, 433–439.

[58] Hyungsoon Im, Kyle C Bantz, Nathan C Lindquist, Christy L Haynes, and Sang-Hyun Oh, *Vertically oriented sub-10-nm plasmonic nanogap arrays*, Nano letters **10** (2010), no. 6, 2231–2236.

[59] Dae Hong Jeong, You Xiang Zhang, and Martin Moskovits, *Polarized surface enhanced raman scattering from aligned silver nanowire rafts*, The Journal of Physical Chemistry B **108** (2004), no. 34, 12724–12728.

References

[60] PB Johnson and RW Christy, *Optical constants of transition metals: Ti, v, cr, mn, fe, co, ni, and pd*, Physical Review B **9** (1974), no. 12, 5056.

[61] M Kahl, E Voges, S Kostrewa, C Viets, and W Hill, *Periodically structured metallic substrates for sers*, Sensors and Actuators B: Chemical **51** (1998), no. 1-3, 285–291.

[62] Y Kanamori, M Ishimori, and K Hane, *High efficient light-emitting diodes with antireflection subwavelength gratings*, IEEE Photonics Technology Letters **14** (2002), no. 8, 1064–1066.

[63] Yoshiaki Kanamori, Ken-ichi Kobayashi, Hiroo Yugami, and Kazuhiro Hane, *Subwavelength antireflection gratings for gasb in visible and near-infrared wavelengths*, Japanese journal of applied physics **42** (2003), no. 6S, 4020.

[64] Gumin Kang, Jeonghoon Yoo, Joonmo Ahn, and Kyoungsik Kim, *Transparent dielectric nanostructures for efficient light management in optoelectronic applications*, Nano Today **10** (2015), no. 1, 22–47.

[65] Young Hun Kang, Sang Soon Oh, Young-Sung Kim, and Choon-Gi Choi, *Fabrication of antireflection nanostructures by hybrid nano-patterning lithography*, Microelectronic Engineering **87** (2010), no. 2, 125–128.

[66] F Karbassian, B Kheyraddini Mousavi, S Rajabali, R Talei, S Mohajerzadeh, and E Asl-Soleimani, *Formation of luminescent silicon nanowires and porous silicon by metal-assisted electroless etching*, Journal of electronic materials **43** (2014), no. 4, 1271–1279.

[67] M Karnan, V Balachandran, M Murugan, MK Murali, and A Nataraj, *Vibrational (ft-ir and ft-raman) spectra, nbo, homo–lumo, molecular electrostatic potential surface and computational analysis of 4-(trifluoromethyl) benzylbromide*, Spectrochimica Acta Part A: Molecular and Biomolecular Spectroscopy **116** (2013), 84–95.

[68] Maheshwar R Kashamolla, Drew F Goettler, Arash K Mousavi, and Zayd C Leseman, *Mode ii measurements for stiction failed mems devices*, ASME 2010 International Mechanical Engineering Congress and Exposition, American Society of Mechanical Engineers, 2010, pp. 63–69.

[69] Scott R Kennedy and Michael J Brett, *Porous broadband antireflection coating by glancing angle deposition*, Applied optics **42** (2003), no. 22, 4573–4579.

[70] Arash Kheyraddini Mousavi, *Characterization of mechanical properties at the micro/nano scale: Stiction failure of mems, high-frequency michelson interferometry and carbon nanofibers*, (2015).

References

[71] Arash Kheyraddini Mousavi, Seyedhamidreza Alaie, and Zayd Chad Leseman, *Basic mems actuators*, Encyclopedia of Nanotechnology (2016), 1–16.

[72] M Khorasaninejad, J Walia, and SS Saini, *Enhanced first-order raman scattering from arrays of vertical silicon nanowires*, Nanotechnology **23** (2012), no. 27, 275706.

[73] Dae-Seon Kim, Min-Su Park, and Jae-Hyung Jang, *Fabrication of cone-shaped subwavelength structures by utilizing a confined convective self-assembly technique and inductively coupled-plasma reactive-ion etching*, Journal of Vacuum Science & Technology B, Nanotechnology and Microelectronics: Materials, Processing, Measurement, and Phenomena **29** (2011), no. 2, 020602.

[74] Hyunsoo Kim, Jaehee Cho, Jeong Wook Lee, Sukho Yoon, Hyungkun Kim, Cheolsoo Sone, Yongjo Park, and Tae-Yeon Seong, *Enhanced light extraction of gan-based light-emitting diodes by using textured n-type gan layers*, Applied physics letters **90** (2007), no. 16, 161110.

[75] Jae-Jun Kim, Youngseop Lee, Ha Gon Kim, Ki-Ju Choi, Hee-Seok Kweon, Seongchong Park, and Ki-Hun Jeong, *Biologically inspired led lens from cuticular nanostructures of firefly lantern*, Proceedings of the national academy of sciences **109** (2012), no. 46, 18674–18678.

[76] Pratik Kothary, Blayne M Phillips, Sin-Yen Leo, and Peng Jiang, *Bioinspired broadband midwavelength infrared antireflection coatings on silicon*, Journal of Vacuum Science & Technology B, Nanotechnology and Microelectronics: Materials, Processing, Measurement, and Phenomena **34** (2016), no. 4, 041807.

[77] Arvind Kumar, Harsh Chaliyawala, Soumik Siddhanta, and Harish C Barshilia, *Broadband quasi-omnidirectional sub-wavelength nanoporous antireflecting surfaces on glass substrate for solar energy harvesting applications*, Solar Energy Materials and Solar Cells **145** (2016), 432–439.

[78] K Kurihara, Y Saitou, N Souma, S Makihara, H Kato, and T Nakano, *Fabrication of nano-structure anti-reflective lens using platinum nanoparticles in injection moulding*, Materials Research Express **2** (2014), no. 1, 015008.

[79] Hee Kwan Lee, Myung Sub Kim, and Jae Su Yu, *Light-extraction enhancement of large-area gan-based leds with electrochemically grown zno nanorod arrays*, IEEE Photonics Technology Letters **23** (2011), no. 17, 1204–1206.

[80] Jung Woo Leem, Bhaskar Dudem, and Jae Su Yu, *Thermal-tolerant polymers with antireflective and hydrophobic grooved subwavelength grating surfaces for high-performance optics*, RSC Advances **6** (2016), no. 83, 79755–79762.

References

[81] Jung Woo Leem, Xiang-Yu Guan, Minkyu Choi, and Jae Su Yu, *Broadband and omnidirectional highly-transparent coverglasses coated with biomimetic moth-eye nanopatterned polymer films for solar photovoltaic system applications*, Solar Energy Materials and Solar Cells **134** (2015), 45–53.

[82] Jung Woo Leem, Young Min Song, and Jae Su Yu, *Broadband wide-angle antireflection enhancement in azo/si shell/core subwavelength grating structures with hydrophobic surface for si-based solar cells*, Optics express **19** (2011), no. 105, A1155–A1164.

[83] Jung Woo Leem, Jae Su Yu, Jonggon Heo, Won-Kyu Park, Jin-Hong Park, Woo Jin Cho, and Do Eok Kim, *Nanostructured encapsulation coverglasses with wide-angle broadband antireflection and self-cleaning properties for iii–v multi-junction solar cell applications*, Solar Energy Materials and Solar Cells **120** (2014), 555–560.

[84] JW Leem, YM Song, YT Lee, and JS Yu, *Antireflective properties of azo subwavelength gratings patterned by holographic lithography*, Applied Physics B **99** (2010), no. 4, 695–700.

[85] V Lehmann and Ulrich Gösele, *Porous silicon formation: A quantum wire effect*, Applied Physics Letters **58** (1991), no. 8, 856–858.

[86] Yunfeng Li, Junhu Zhang, and Bai Yang, *Antireflective surfaces based on biomimetic nanopillared arrays*, Nano Today **5** (2010), no. 2, 117–127.

[87] Yunfeng Li, Junhu Zhang, Shoujun Zhu, Heping Dong, Fei Jia, Zhanhua Wang, Yue Tang, Liang Zhang, Shiyu Zhang, and Bai Yang, *Bioinspired silica surfaces with near-infrared improved transmittance and superhydrophobicity by colloidal lithography*, Langmuir **26** (2010), no. 12, 9842–9847.

[88] Shuang Lin, Xiang Lin, Xiu-Tao Lou, Fang Yang, Dian-Yang Lin, Zhi-Wei Lu, et al., *Rapid and sensitive sers method for determination of rhodamine b in chili powder with paper-based substrates*, Analytical Methods **7** (2015), no. 12, 5289–5294.

[89] Yu-Sheng Lin, Wen-Ching Hsu, Kuo-Cheng Huang, and J Andrew Yeh, *Wafer-level fabrication and optical characterization of nanoscale patterned sapphire substrates*, Applied Surface Science **258** (2011), no. 1, 2–6.

[90] Xiaojun Liu, Jianqiang Gu, Ranjan Singh, Yingfang Ma, Jun Zhu, Zhen Tian, Mingxia He, Jiaguang Han, and Weili Zhang, *Electromagnetically induced transparency in terahertz plasmonic metamaterials via dual excitation pathways of the dark mode*, Applied Physics Letters **100** (2012), no. 13, 131101.

References

[91] John R Lombardi and Ronald L Birke, *A unified approach to surface-enhanced raman spectroscopy*, The Journal of Physical Chemistry C **112** (2008), no. 14, 5605–5617.

[92] Cheng Lu and RH Lipson, *Interference lithography: a powerful tool for fabricating periodic structures*, Laser & Photonics Reviews **4** (2010), no. 4, 568–580.

[93] Bruce D MacLeod and Douglas S Hobbs, *Low-cost anti-reflection technology for automobile displays*, Journal of the Society for Information Display, Automotive Display Conference, 2004.

[94] Mariana Medina-Sánchez, Sandrine Miserere, and Arben Merkoçi, *Nanomaterials and lab-on-a-chip technologies*, Lab on a Chip **12** (2012), no. 11, 1932–1943.

[95] AK Mousavi, MR Kashamolla, and ZC Leseman, *Improved model for the adhesion of μcantilevers: Theory and experiments*, Journal of Micromechanics and Microengineering **23** (2013), no. 11, 115011.

[96] Arash K Mousavi, Mark A Atwater, Behnam K Mousavi, Mohammad Jalalpour, Mahmoud Reda Taha, and Zayd C Leseman, *Mechanical and electrical characterization of entangled networks of carbon nanofibers*, Materials **7** (2014), no. 6, 4845–4853.

[97] Arash Kheyraddini Mousavi, Khawar Abbas, Mirza Mohammad Mahbube Elahi, Edidson Lima, Stephen Moya, Joseph Daniel Butner, Denise Pinon, Adeeko Benga, Behnam Kheyraddini Mousavi, and Zayd Chad Leseman, *Pulsed vacuum and etching systems: Theoretical design considerations for a pulsed vacuum system and its application to xef 2 etching of si*, Vacuum **109** (2014), 216–222.

[98] Arash Kheyraddini Mousavi and Zayd Chad Leseman, *Basic mems actuators*, Encyclopedia of Nanotechnology, Springer, 2012, pp. 173–185.

[99] Shaunak Mukherjee, Florian Libisch, Nicolas Large, Oara Neumann, Lisa V Brown, Jin Cheng, J Britt Lassiter, Emily A Carter, Peter Nordlander, and Naomi J Halas, *Hot electrons do the impossible: plasmon-induced dissociation of h2 on au*, Nano letters **13** (2012), no. 1, 240–247.

[100] Gururaj V Naik and Alexandra Boltasseva, *Semiconductors for plasmonics and metamaterials*, physica status solidi (RRL)-Rapid Research Letters **4** (2010), no. 10, 295–297.

[101] Gottlieb S Oehrlein, *Dry etching damage of silicon: A review*, Materials Science and Engineering: B **4** (1989), no. 1-4, 441–450.

References

[102] Andreas Otto, *What is observed in single molecule sers, and why?*, Journal of Raman Spectroscopy **33** (2002), no. 8, 593–598.

[103] Birgit Päivänranta, Noora Heikkilä, and Markku Kuittinen, *Antireflective subwavelength-structured surfaces with enhanced color properties*, JOSA A **24** (2007), no. 6, 1680–1686.

[104] Birgit Päivänranta, Andreas Langner, Eugenie Kirk, Christian David, and Yasin Ekinci, *Sub-10 nm patterning using euv interference lithography*, Nanotechnology **22** (2011), no. 37, 375302.

[105] Edward D Palik, *Handbook of optical constants of solids, five-volume set: Handbook of thermo-optic coefficients of optical materials with applications*, Elsevier, 1997.

[106] P Papet, O Nichiporuk, A Kaminski, Y Rozier, J Kraiem, J-F Lelievre, A Chaumartin, A Fave, and M Lemiti, *Pyramidal texturing of silicon solar cell with tmah chemical anisotropic etching*, Solar Energy Materials and Solar Cells **90** (2006), no. 15, 2319–2328.

[107] K Baghbani Parizi, N Peyvast, B Kheyraddini Mousavi, S Mohajerzadeh, and M Fathipour, *Schottky barrier nano-mosfet with an asymmetrically oxidized source/drain structure*, Solid-State Electronics **54** (2010), no. 1, 48–51.

[108] Panos Patsalas, Nikolaos Kalfagiannis, and Spyros Kassavetis, *Optical properties and plasmonic performance of titanium nitride*, Materials **8** (2015), no. 6, 3128–3154.

[109] GJ Puppels, A Huizinga, HW Krabbe, HA De Boer, G Gijsbers, and FFM De Mul, *A high-throughput raman notch filter set*, Review of scientific instruments **61** (1990), no. 12, 3709–3712.

[110] Hemant Kumar Raut, V. Anand Ganesh, A. Sreekumaran Nair, and Seeram Ramakrishna, *Anti-reflective coatings: A critical, in-depth review*, Energy Environ. Sci. **4** (2011), 3779–3804.

[111] Shashank Sarbada, Zhifeng Huang, Yung C Shin, and Xiulin Ruan, *Low-reflectance laser-induced surface nanostructures created with a picosecond laser*, Applied Physics A **122** (2016), no. 4, 453.

[112] Rudiger Schlaf, *Method of producing an integrated circuit with a carbon nanotube*, December 28 2004, US Patent 6,835,613.

References

[113] Martin F Schubert, Frank W Mont, Sameer Chhajed, David J Poxson, Jong Kyu Kim, and E Fred Schubert, *Design of multilayer antireflection coatings made from co-sputtered and low-refractive-index materials by genetic algorithm*, Optics express **16** (2008), no. 8, 5290–5298.

[114] Marcel Schulze, Michael Damm, Michael Helgert, Ernst-Bernhard Kley, Stefan Nolte, and Andreas Tünnermann, *Durability of stochastic antireflective structures-analyses on damage thresholds and adsorbate elimination*, Optics express **20** (2012), no. 16, 18348–18355.

[115] JP Simko and GS Oehrlein, *Reactive ion etching of silicon and silicon dioxide in cf 4 plasmas containing h 2 or c 2 f 4 additives*, Journal of The Electrochemical Society **138** (1991), no. 9, 2748–2752.

[116] Vivek Singh, Pao Tai Lin, Neil Patel, Hongtao Lin, Lan Li, Yi Zou, Fei Deng, Chaoying Ni, Juejun Hu, James Giammarco, et al., *Mid-infrared materials and devices on a si platform for optical sensing*, Science and Technology of Advanced Materials **15** (2014), no. 1, 014603.

[117] Young Min Song, Gyeong Cheol Park, Eun Kyu Kang, Chan Il Yeo, and Yong Tak Lee, *Antireflective grassy surface on glass substrates with self-masked dry etching*, Nanoscale research letters **8** (2013), no. 1, 505.

[118] DG Stavenga, S Foletti, G Palasantzas, and K Arikawa, *Light on the moth-eye corneal nipple array of butterflies*, Proceedings of the Royal Society of London B: Biological Sciences **273** (2006), no. 1587, 661–667.

[119] Kai-Hung Su, Stephane Durant, Jennifer M Steele, Yi Xiong, Cheng Sun, and Xiang Zhang, *Raman enhancement factor of a single tunable nanoplasmonic resonator*, The Journal of Physical Chemistry B **110** (2006), no. 9, 3964–3968.

[120] KH Su, QH Wei, and X Zhang, *Tunable and augmented plasmon resonances of au/ si o 2/ au nanodisks*, Applied Physics Letters **88** (2006), no. 6, 063118.

[121] Chih-Hung Sun, Brian J Ho, Bin Jiang, and Peng Jiang, *Biomimetic subwavelength antireflective gratings on gaas*, Optics letters **33** (2008), no. 19, 2224–2226.

[122] Mohammad Mahdi Tavakoli, Kwong-Hoi Tsui, Qianpeng Zhang, Jin He, Yan Yao, Dongdong Li, and Zhiyong Fan, *Highly efficient flexible perovskite solar cells with antireflection and self-cleaning nanostructures*, ACS nano **9** (2015), no. 10, 10287–10295.

References

[123] Tefera E Tesema, Bijesh Kafle, Meron G Tadesse, and Terefe G Habteyes, *Plasmon-enhanced resonant excitation and demethylation of methylene blue*, The Journal of Physical Chemistry C **121** (2017), no. 13, 7421–7428.

[124] Ian M Thomas, *High laser damage threshold porous silica antireflective coating*, Applied Optics **25** (1986), no. 9, 1481–1483.

[125] Lianming Tong, Maurizio Righini, Maria Ujue Gonzalez, Romain Quidant, and Mikael Käll, *Optical aggregation of metal nanoparticles in a microfluidic channel for surface-enhanced raman scattering analysis*, Lab on a Chip **9** (2009), no. 2, 193–195.

[126] *Silicon transmission*, `http://www.tydexoptics.com/pdf/Si.pdf`, Accessed: 2010-09-30.

[127] Laurent Vaissié, Oleg V Smolski, Alok Mehta, and Eric G Johnson, *High efficiency surface-emitting laser with subwavelength antireflection structure*, IEEE photonics technology letters **17** (2005), no. 4, 732–734.

[128] T Vo-Dinh, JP Alarie, N Isola, D Landis, Al L Wintenberg, and MN Ericson, *Dna biochip using a phototransistor integrated circuit*, Analytical Chemistry **71** (1999), no. 2, 358–363.

[129] Tuan Vo-Dinh, *Sers diagnostic platforms, methods and systems microarrays, biosensors and biochips*, (2007), US Patent 7,267,948.

[130] Angela Walter, Anne März, Wilm Schumacher, Petra Rösch, and Jürgen Popp, *Towards a fast, high specific and reliable discrimination of bacteria on strain level by means of sers in a microfluidic device*, Lab on a Chip **11** (2011), no. 6, 1013–1021.

[131] Xiaotian Wang, Wensheng Shi, Guangwei She, and Lixuan Mu, *Using si and ge nanostructures as substrates for surface-enhanced raman scattering based on photoinduced charge transfer mechanism*, Journal of the American Chemical Society **133** (2011), no. 41, 16518–16523.

[132] ZY Wang, RJ Zhang, SY Wang, M Lu, X Chen, YX Zheng, LY Chen, Z Ye, CZ Wang, and KM Ho, *Broadband optical absorption by tunable mie resonances in silicon nanocone arrays*, Scientific reports **5** (2015), 7810.

[133] Sabrina M Wells, Igor A Merkulov, Ivan I Kravchenko, Nickolay V Lavrik, and Michael J Sepaniak, *Silicon nanopillars for field-enhanced surface spectroscopy*, ACS nano **6** (2012), no. 4, 2948–2959.

References

[134] Binbin Weng, Jijun Qiu, Zijian Yuan, Preston R Larson, Gregory W Strout, and Zhisheng Shi, *Responsivity enhancement of mid-infrared pbse detectors using caf2 nano-structured antireflective coatings*, Applied Physics Letters **104** (2014), no. 2, 021109.

[135] Kirt R Williams, Kishan Gupta, and Matthew Wasilik, *Etch rates for micromachining processing-part ii*, Journal of microelectromechanical systems **12** (2003), no. 6, 761–778.

[136] Deying Xia and SRJ Brueck, *A facile approach to directed assembly of patterns of nanoparticles using interference lithography and spin coating*, Nano letters **4** (2004), no. 7, 1295–1299.

[137] Yao Xu, Bing Zhang, Wen Hao Fan, Dong Wu, and Yu Han Sun, *Sol–gel broadband anti-reflective single-layer silica films with high laser damage threshold*, Thin Solid Films **440** (2003), no. 1, 180–183.

[138] Itsunari Yamada, Kenji Kintaka, Junji Nishii, Satoshi Akioka, Yutaka Yamagishi, and Mitsunori Saito, *Mid-infrared wire-grid polarizer with silicides*, Optics letters **33** (2008), no. 3, 258–260.

[139] Jing Yang, Fangfang Luo, Tsung Sheng Kao, Xiong Li, Ghim Wei Ho, Jinghua Teng, Xiangang Luo, and Minghui Hong, *Design and fabrication of broadband ultralow reflectivity black si surfaces by laser micro/nanoprocessing*, Light: Science & Applications **3** (2014), no. 7, e185.

[140] Ma Ye-Wan, Zhang Li-Hua, Wu Zhao-Wang, and Zhang Jie, *Optical properties of plasmon resonances with ag/sio2/ag multi-layer composite nanoparticles*, Chinese Physics Letters **27** (2010), no. 6, 064204.

[141] Bulent E Yoldas and Deborah P Partlow, *Formation of broad band antireflective coatings on fused silica for high power laser applications*, Thin solid films **129** (1985), no. 1-2, 1–14.

[142] Zhaoning Yu, He Gao, Wei Wu, Haixiong Ge, and Stephen Y Chou, *Fabrication of large area subwavelength antireflection structures on si using trilayer resist nanoimprint lithography and liftoff*, Journal of Vacuum Science & Technology B: Microelectronics and Nanometer Structures Processing, Measurement, and Phenomena **21** (2003), no. 6, 2874–2877.

[143] Qiang Zhang, Jun Jun Xiao, Xiao Ming Zhang, Dezhuan Han, and Lei Gao, *Core–shell-structured dielectric–metal circular nanodisk antenna: gap plasmon assisted magnetic toroid-like cavity modes*, ACS Photonics **2** (2014), no. 1, 60–65.

References

[144] XM Zhang, JJ Xiao, Q Zhang, LM Li, and Y Yao, *Plasmonic tm-like cavity modes and the hybridization in multilayer metal-dielectric nanoantenna*, Optics express **23** (2015), no. 12, 16122–16132.

[145] J Zhao, A Wang, P Altermatt, and MA Green, *Twenty-four percent efficient silicon solar cells with double layer antireflection coatings and reduced resistance loss*, Applied Physics Letters **66** (1995), no. 26, 3636–3638.

[146] Junhong Zhao, Jian Lin, Hengyong Wei, Xiuhua Li, Wenjun Zhang, Guannan Zhao, Jinglong Bu, and Ying Chen, *Surface enhanced raman scattering substrates based on titanium nitride nanorods*, Optical Materials **47** (2015), 219–224.

[147] Yiping Zhao, Dexian Ye, Gwo-Ching Wang, and Toh-Ming Lu, *Designing nanostructures by glancing angle deposition*, Optical Science and Technology, SPIE's 48th Annual Meeting, International Society for Optics and Photonics, 2003, pp. 59–73.

[148] Lei Zhou, Xiaoxuan Dong, Yun Zhou, Wenming Su, Xiaolian Chen, Yufu Zhu, and Su Shen, *Multiscale micro–nano nested structures: Engineered surface morphology for efficient light escaping in organic light-emitting diodes*, ACS applied materials & interfaces **7** (2015), no. 48, 26989–26998.

[149] Weidong Zhou, Meng Tao, Li Chen, and Hongjun Yang, *Microstructured surface design for omnidirectional antireflection coatings on solar cells*, Journal of Applied Physics **102** (2007), no. 10, 103105.

[150] Xiaolong Zhu, Wei Yan, Peter Uhd Jepsen, Ole Hansen, N Asger Mortensen, and Sanshui Xiao, *Experimental observation of plasmons in a graphene monolayer resting on a two-dimensional subwavelength silicon grating*, Applied Physics Letters **102** (2013), no. 13, 131101.